

Soft X-Ray Spectrometers for Absorption Spectroscopy of Aluminum in Laser Driven Backlighter Experiments

**Spektrometer für weiche Röntgenstrahlung aus laser-getriebenen Quellen zur
Absorptionsspektroskopie von Aluminium**

Master Thesis by Carlos Butler

Date: January 1, 2024

1. Review: Prof. Dr. Vincent Bagnoud
Darmstadt



TECHNISCHE
UNIVERSITÄT
DARMSTADT

Physics Department
Institute of Nuclear Physics
Working Group Bagnoud

Soft X-Ray Spectrometers for Absorption Spectroscopy of Aluminum in Laser Driven Backlighter Experiments

Spektrometer für weiche Röntgenstrahlung aus laser-getriebenen Quellen zur Absorptionsspektroskopie von Aluminium

Master Thesis by Carlos Butler

Date: January 1, 2024

Darmstadt

Erklärung zur Abschlussarbeit gemäß § 22 Abs. 7 APB TU Darmstadt

Hiermit erkläre ich, Carlos Butler, dass ich die vorliegende Arbeit gemäß § 22 Abs. 7 APB der TU Darmstadt selbstständig, ohne Hilfe Dritter und nur mit den angegebenen Quellen und Hilfsmitteln angefertigt habe. Ich habe mit Ausnahme der zitierten Literatur und anderer in der Arbeit genannter Quellen keine fremden Hilfsmittel benutzt. Die von mir bei der Anfertigung dieser wissenschaftlichen Arbeit wörtlich oder inhaltlich benutzte Literatur und alle anderen Quellen habe ich im Text deutlich gekennzeichnet und gesondert aufgeführt. Dies gilt auch für Quellen oder Hilfsmittel aus dem Internet.

Diese Arbeit hat in gleicher oder ähnlicher Form noch keiner Prüfungsbehörde vorgelegen.

Mir ist bekannt, dass im Falle eines Plagiats (§ 38 Abs. 2 APB) ein Täuschungsversuch vorliegt, der dazu führt, dass die Arbeit mit 5,0 bewertet und damit ein Prüfungsversuch verbraucht wird. Abschlussarbeiten dürfen nur einmal wiederholt werden.

Bei einer Thesis des Fachbereichs Architektur entspricht die eingereichte elektronische Fassung dem vorgestellten Modell und den vorgelegten Plänen.

Darmstadt,

C. Butler

Contents

1. Introduction	9
2. X-Ray Absorption Fine-Structure Spectroscopy	13
3. Fundamentals of X-Ray Spectrometers	17
3.1. Flat Crystal Geometries	18
3.2. Bent Crystal Geometries	18
3.2.1. Von Hamos Geometry	19
3.2.2. Focusing Spectrograph with Spatial Resolution	19
3.3. Dispersion Calculation	21
3.4. Resolution	25
4. Spectrometer Design	27
4.1. Design Considerations	27
4.2. Implemented Spectrometer Schemes	29
4.2.1. Dual Unbent Crystal Spectrometer	30
4.2.2. Focusing Spectrograph with Spatial Resolution	31
4.2.3. Single Unbent Crystal Spectrometer	32
4.3. Specifications and Comparison	33
5. Experimental Setup	37
5.1. General Setup	37
5.2. Mechanical Design of Spectrometers	40
5.2.1. Dual Unbent Crystal Spectrometer	41
5.2.2. Focusing Spectrograph with Spatial Resolution	43
6. Data Analysis	47
7. Results and Discussion	51
7.1. Qualitative Performance	51
7.1.1. X-ray Source Spectra	51
7.1.2. X-ray Absorption Spectra	55
7.2. Spectrometer Characterization	59
7.2.1. Spectral Resolution	59
7.2.2. Integrated Reflectivity Ratio	66
7.3. Setup Validation	69
7.3.1. Conversion Efficiency into He- α Line of Aluminum	69
8. Summary and Outlook	73

Bibliography	77
Appendices	81
I. Crystal Considerations	81
II. Spectrometer Simulations	83
i. Simple Ray Tracing of the Focusing Spectrograph with Spatial Resolution	83
ii. Simulation of the Focusing Spectrograph with Spatial Resolution	85
iii. Simulation of the Dual Unbent Crystal Spectrometer	87
iv. Summary of Simulation Results	90
III. Alignment Procedure for FSSR-1D	91
IV. Supplementary Results	95
i. Spectral Resolution	95
ii. Integrated Reflectivity Ratio	96
iii. Conversion Efficiency into He- α Line of Aluminum	97
V. Uncertainty Analysis	99
i. Spectral Resolution	99
ii. Ratio of Integrated Reflectivities	100
iii. Conversion Efficiency into He- α Line of Aluminum	100

Acknowledgments

ADD MORE LATER

Here I want to note that the spectrometer designs, in all their facets, were made possible with the help and input of Artem Martynenko, Zsuzsanna Major, and in particular, Philipp Hesselbach and Paul Neumayer, who contributed the initial designs, offered continued support in all stages of this thesis.

1. Introduction

The experimental study of warm dense matter (WDM) has been gaining steam in the last few decades thanks to developments in laser and accelerator facilities, allowing researchers to better probe these elusive states of matter [1–3]. WDM, though not precisely defined, is generally considered to encompass states with pressures above 100 GPa, temperatures in the range of 1 eV to 100 eV, and high densities, lying at or above solid density [1]. In this regime the plasma displays unique properties, including strongly coupled, fluid-like ions and fully or partially degenerate electrons, which invalidates many standard approximations in the current theory [2] and makes WDM difficult to describe. In addition to this theoretical interest, WDM is of great importance to many fields, ranging from astrophysics, where the study of WDM gives insight into the internal structure and evolution of many celestial objects [4–6], to inertial confinement fusion, relevant for the understanding of implosions of laser fusion capsules [1, 2]. Consequently, many large-scale experiments are conducted on WDM [7–9], which all seek to solve the significant experimental challenges inherent to WDM, i.e. the generation of extreme conditions [2, 4] and the consequently short lifetimes on the order of micro- to nanoseconds [1].

The necessity of rapidly depositing large amounts of energy with powerful drivers to reach WDM conditions presents a considerable experimental challenge, which is tackled with a number of methods. In general, two main requirements play a role in assessing the viability of a WDM driver. One is uniformity of the sample, as strong temperature or density gradients can hinder comparison with theory and therefore make it difficult to assess the WDM properties. This limitation rules out many direct drivers. The other requirement is timescale. The sample should stay within WDM conditions long enough for probes and optimally allow time for equilibration [10]. Since static methods, such as diamond anvil cells (DAC), where the sample is confined and compressed between diamond anvils [11], only reach temperatures and pressures at the low end of the WDM range (\approx 100 GPa and \lesssim 1 eV), dynamic methods are often pursued.

The dynamic WDM generation methods can be loosely placed in two categories: shock/ramp compression and volumetric heating [10]. A notable example of the former type is indirectly laser driven shocks delivered by x-rays generated by a high-Z cylindrical hohlraum target irradiated with intense laser pulses, which ablates the top layer of a shock target located in the center of the hohlraum, driving a shock which culminates in the center. This method was successfully applied at the National Ignition Facility (NIF) in California to generate WDM of beryllium [12]. A promising application of the latter type, volumetric heating, comes in the form of ultra-short x-ray pulses from x-ray free-electron lasers (XFEL). These intense pseudo-monochromatic x-ray beams are focused to a spot size of a few microns. Upon irradiating a sample target, the photons are mostly absorbed through photo-absorption in a given band or shell of the material, depositing their energy uniformly within femtoseconds and producing a transient WDM state [10], as demonstrated at the Linac Coherent Light Source (LCLS) facility in California [13]. An alternative approach to volumetric heating, and the one relevant to this work, are intense heavy-ion beams, which transfer energy to a sample through coulomb collisions between the ions in the beam and electrons in the target. As such the penetration range is on the scale of several mm and heating can occur isochorically along the whole sample [14]. These properties offer significant advantages in that large (mm^3) high-Z WDM samples

with sufficient lifetimes for equilibration and high uniformity can be produced [1, 6], opening doors to new WDM physics.

Similarly to the generation of warm dense matter, the diagnostics and characterization of WDM samples require addressing unique obstacles. Due to the short lifetimes of the state, the diagnostic methods must allow for fast data acquisition. Additionally, the high opacity of WDM samples in the optical range means that most methods of optical probing are excluded, unless performing surface or shock-wave measurements [1, 2, 15]. X-rays, on the other hand, are capable of penetrating these samples thanks to longer attenuation lengths, and therefore offer effective diagnostic techniques for probing the bulk properties of WDM [7, 16]. In order to apply these techniques, intense, fast x-ray sources, also referred to as backscatterers, are required. Common methods to produce x-rays for WDM experiments include synchrotron [16], x-ray free-electron lasers [17], and laser-driven plasmas. Interestingly, in the case of XFEL, the x-ray beam can simultaneously act as the WDM driver and a selective probe, as shown at NIF by Vinko, *et al.* [13]. In this work, laser-driven plasma acts as a high-brightness fast x-ray source for the diagnostics by irradiating backscatterer targets with a high-intensity short-pulse optical laser, which can be tuned to desired energy ranges and intensities through the choice of backscatterer material and laser energy [7]. The tunability, high intensity, and small angular dependence of the x-ray emission are especially attractive to WDM matter research.

Advances in the area of intense x-ray beam production enable several diagnostic techniques applicable to WDM research, including x-ray scattering, radiography, and x-ray absorption spectroscopy [1, 2]. The first method involves studying features in spectrally resolved x-ray scattering measurements and comparing the results to theoretical descriptions of the scattering [10]. In this way, Lee *et al.* successfully determined the ion temperature and density of laser-driven dense plasma of beryllium [18]. Another effective diagnostic technique is X-ray Absorption Fine-Structure Spectroscopy (XAES), an extension of x-ray absorption spectroscopy, which was first demonstrated in the scope of WDM research in 1987 by Hall *et al.* [19] and is the diagnostic of choice in this work. This method extracts bulk properties of a sample by investigating features of an absorption spectrum located around an edge, defined by the binding energy of a shell of electrons. The features form when electrons released through the photoelectric effect with incident x-rays quantum mechanically scatter on neighboring atoms in the sample. The back-scattered photoelectron wave-functions overlap with the electron state at the original atom, modulating the absorption coefficient [20]. As this modulation behaves differently depending on proximity to the absorption edge, one distinguishes between X-ray Absorption Near Edge Structure (XANES) and Extended X-ray Absorption Fine-structure (EXAFS), i.e. after the edge [21]. As a smaller energy range and higher spectral resolution is required for XANES as compared to EXAFS and because each stem from different physical interactions, experiments commonly target one specifically. Because each sub-technique allows for determining different material properties [1], XAES can cover a wide range of applications, although it is important to note that the method needs a smooth backscatterer spectrum as well as an uniform sample to resolve the fine-structures [10]. Accordingly, the experimental setup must be designed specifically with XAES in mind.

The general experimental scheme (see fig. 1.1), which will build the context of this work, seeks to leverage three methods of WDM research in a novel way: intense heavy-ion beams for WDM generation, laser-driven plasma for backlighting, and XAES for diagnostics. The heavy-ion beam produces large, highly homogeneous WDM samples, while the high intensity and tunability of the laser-driven backscatterer allows for a smooth x-ray source spectrum with a significant x-ray flux. Together, these advantages harmonize well with XAES to create the possibility of highly resolved absorption spectra of uniform WDM samples, with which bulk properties can be extracted with precision, opening the door to further advances in WDM research.

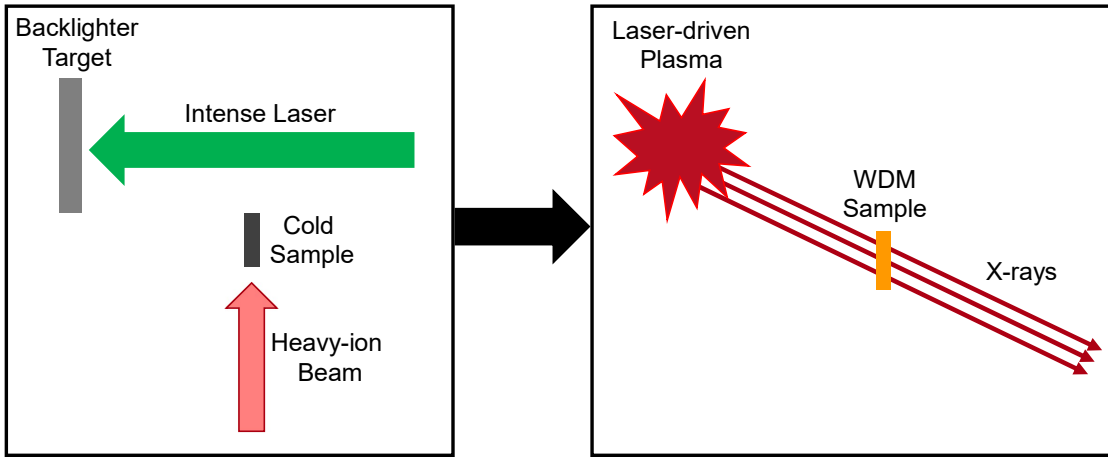


Figure 1.1.: The general experimental scheme that forms the basis of the overarching project, under which the experiment conducted in the scope of this work falls. A laser-driven plasma, induced by an intense short-pulse optical laser, serves as the backlighter for a WDM sample heated with a heavy-ion beam. The x-rays emitted by the plasma pass through the sample and are then used for diagnostics.

A project utilizing this scheme will be realized at the Facility for Antiproton and Ion Research (FAIR), an accelerator facility under construction in Darmstadt, Germany [15], with preliminary experiments currently underway at a neighboring facility, the GSI Helmholtz Center for Heavy Ion Research [7]. With the goal of validating the experimental setup and demonstrating a proof of concept, preparatory experiments are conducted at the High energy, High Temperature (HHT) experimental station and beamline finished in 2021, where high-energy ns-pulse laser beams from the Petawatt High-Energy Laser for Heavy Ion Experiments (PHELIX) are combined with heavy-ion beams originating at the UNIversal Linear ACcelerator (UNILAC) and accelerated by the heavy ion synchrotron SIS-18. Using these heavy-ion beams with velocities of $0.9 c$ [22], ion counts of $\sim 4 \cdot 10^9$ for U^{73+} per FWHM = 100 ns bunch, and an ion focal spot of $\sim 1 \times 1 \text{ mm}^2$ [23], along with PHELIX beams with laser energies of up to 200 J at 2ω (527 nm) for ns-pulses with a FWHW of 25 μm , heavy-ion heating experiments using x-rays from laser-driven plasma can be conducted. As such, GSI offers the, as of writing this, unique ability to combine intense heavy-ion beams with high-energy ns-pulse laser beams [24]. These capabilities will be expanded in the future at the Atomic, Plasma Physics and Applications (APPA) cave at FAIR, in its final stage achieving ion numbers of up to $\sim 5 \cdot 10^{11}$ ions (U^{73+}) per bunch through acceleration in the synchrotron SIS-100 [15]. The APPA cave will combine this more intense heavy-ion beam with a laser system of comparable characteristics to PHELIX, finally reaching the WDM regime with temperature states of up to $> 10 \text{ eV}$ [15].

On the path towards the generation of WDM, an experiment at HHT using the heavy-ions of the SIS-18 synchrotron is planned for 2024, aiming to investigate heavy-ion heated Al samples through absorption spectroscopy of the Al K-edge. The work of this thesis is carried out in the context of a preparatory experiment conducted in May, 2023, whose goal is to investigate and optimize the laser-driven x-ray backlighter and XAFS diagnostics setup in a laser-only beamtime using PHELIX.

Essential to the proposed experiments are x-ray spectrometers, which act as the primary measurement devices. By the nature of x-ray-matter interactions, conventional optics cannot be used for x-ray diagnostics. In the case of x-ray spectrometers, the number of refracting surfaces is usually limited to one, as otherwise rays are too heavily absorbed [25]. This restriction, as well as the violent conditions inherent to WDM experiments and the requirement of two well aligned spectra for deriving the Al absorption spectrum for

XAFS, necessitate the design of spectrometers unique to this application. As such, my task is the design, implementation, and characterization of soft x-ray spectrometers to conduct XAFS of the Al K-edge by producing high resolution, high signal-to-noise ratio spectra, while accounting for the challenges inherent to the experimental setup.

Due to the prevalence of x-ray diagnostics in high-energy density matter research, x-ray spectrometers have become ubiquitous in the field and are now a well-matured technology [26]. As is typical for the realm of high-resolution x-ray spectroscopy of extreme-state matter, crystals serve as the spectrally dispersing elements of the spectrometers. A deciding factor in the performance of these instruments is the shape of the crystal. In general, flat crystals offer simplicity of design and fewer defects in the crystal structure, while bent crystals enable focusing of the rays, leading to higher flexibility in the design, improved signal-to-noise ratios, and potential for better resolution, at the cost of increased complexity and introduction of crystal defects [25, 26]. Drawing inspiration from spectrometers successfully implemented in other XAFS experiments [16, 19, 27], I created two soft x-ray spectrometers. The first targets the near-edge structures of XAFS and uses a dual channel, flat crystal geometry, while the second is intended for EXAFS and implements a focusing geometry, known as a Focusing Spectrograph with Spatial Resolution (FSSR), with a spherically bent crystal. With these two starkly different constellations, I will weigh two contrasting design philosophies. On one hand, the flat crystal spectrometer focuses on ease of use and reliability, intending to reduce the overall complexity of the experimental setup and ensure best possible crystal quality. On the other, the bent crystal design emphasizes spectrometer performance, yielding potentially improved spectra and greater adaptability, but also adding complexity and chances for unforeseen difficulties. In the course of this thesis, each aspect of the spectrometers and their performance in the 2023 beamtime will be assessed and used to inform the design of spectrometers for future experiments.

This work is structured as follows. In chapter 2, I discuss XAFS in depth and briefly present two experiments applying XAFS in WDM research. In chapter 3, I explain the fundamentals of x-ray spectrometers, outlining the theory behind them with special focus placed on the FSSR. For the FSSR, I collect the sometimes inconsistent information from the literature and reformulate it to present a unified picture. I also derive the analytical dispersion of the geometries relevant for this work and elaborate on resolution. In chapter 4, the considerations and constraints placed on the spectrometer design according to their purpose and the experimental setup are listed and explained, followed by descriptions and explanations of the spectrometer geometries in detail. In chapter 5, I present the experimental setup of the 2023 laser-only experiment at HHT, along with a description of the spectrometers' mechanical design and functions. In chapter 6, the spectrum extraction and analysis procedure of the experimental data are explained. In chapter 7, I present the results and discuss their implications for the spectrometers. Finally, in chapter 8 I summarize the content and findings of this work and apply them to recommend a spectrometer design for a combined experiment in 2024.

2. X-Ray Absorption Fine-Structure Spectroscopy

The method of X-ray Absorption Fine-Structure Spectroscopy (XAFS) probes the electronic structure of atoms in a material by irradiating a sample with X-rays and recording the resulting absorption spectrum. As this diagnostic technique constitutes the purpose of the spectrometers designed in this work, it will be elaborated on in the following.

XAFS originates from X-ray Absorption Spectroscopy (XAS), a method first experimentally established in 1918-1920 at Lund University in a series of experiments by K. Stenström and H. Fricke under the supervision of M. Siegbahn [28, 29]. Although XAS was overshadowed by X-ray Diffraction (XRD) in its first few decades, in large part due to the higher x-ray intensity requirements, it had a key advantage in that it could probe less ordered and liquid materials. As such, the technique experienced a boom in 1975, where the building of large research facilities with electron synchrotrons enabled consistent access to intense x-ray sources [30]. This also marks the advent of XAFS, the modern version of XAS, allowing measurement of the fine structures of absorption edges, which presents the opportunity to locally probe defects and features in lattice structures to a higher degree than other x-ray diagnostics. With over 50% of beamtime requests from industrial customers for synchrotron laboratories pertaining to x-ray absorption methods, XAFS has become a well-established tool to evaluate samples for a wide array of fields, including Chemistry, Biology and Material Science [31].

XAFS is not only limited to conventional samples, but can also be applied to probe short-lived, dynamic states such as WDM [32], which exists in a non-crystalline state where short-range order dominates, making XAFS especially suited as a diagnostic technique [21]. X-ray sources capable of short pulses, like laser-produced plasma, or spectrometers using detectors with rapid recording, like image plates or CCD cameras, enable the collection of a complete spectra on the order of nanoseconds. The first experiment using XAFS on WDM was conducted in 1987, in which converging laser-induced shocks were used to bring an aluminum sample to WDM conditions [19]. Since then, XAFS has been widely used in WDM matter research, with x-ray crystal spectrometers playing a central role [1, 16, 21].

In the context of WDM experiments, XAFS often examines the photon energy range around a K-edge, defined by the binding energy of K-shell electrons in a material. By studying the fine-structures of the absorption spectra in this region, multiple properties of WDM, e.g. density, temperature, and coordination of atoms, can be simultaneously extracted [16, 19, 27]. These structures consist of shifts in the location and shape of the K-edge, as well as oscillations in the absorption coefficient after the edge, and originate from free electrons ejected by x-rays through the photoelectric effect. In a simplified description as depicted in fig 2.1, the wave-functions of the ejected electrons scatter on neighboring atoms, so that a part of the free electron wave-function returns to and interferes with the absorbing atom. As this all occurs in a single coherent quantum state, the process is effectively a modulation of the quantum electronic state at the location of the absorbing atom. Since the absorption coefficient depends on the available electronic states, this phenomenon causes modulation of the absorption probability, and therefore the absorption spectrum, depending on the atomic order within $\approx 5\text{\AA}$ of the absorbing atom [20].

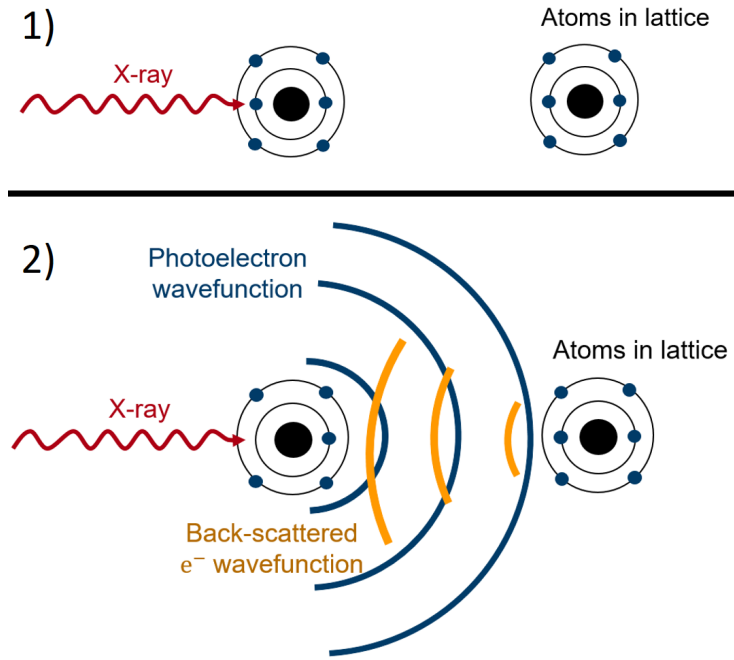


Figure 2.1.: Schematic representation of XAFS mechanism. 1) An electron is ejected from the absorbing atom through the photoelectric effect. 2) The electron wavefunction is partially back-scattered by a neighboring atom in a lattice, which returns to the absorbing atom and modulates the electronic states, consequently modulating the absorption coefficient.

XAFS can be broken down into two techniques: X-ray Absorption Near Edge Structure (XANES), covering the range of 50 eV within the K-edge [33], and Extended X-ray Absorption Fine-Structure (EXAFS), extending as far as 250 eV above the edge [34]. In the case of XANES, the shift and slope of the K-edge are governed by the degeneracy, ionization, and continuum lowering of the plasma and are affected by the temperature and density [2, 21]. For EXAFS, the amplitude of the absorption oscillations is an indicator of ionic temperature, while the position and frequency of the peaks reveal information about the density and ionic order [1]. Note that determining properties from the oscillations is more straightforward for EXAFS, as approximations of single scattering are valid in this region, simplifying theoretical models [20].

To give an idea of what XAFS absorption spectra typically look like and how WDM properties can be determined from them, I will summarize two experiments, with one applying XANES and the other EXAFS, whose results are depicted in fig. 2.2. In an experiment conducted by Levy *et al.* [21] corresponding to fig. 2.2a, WDM of aluminum is produced through isochoric heating with a picosecond proton beam pulse generated by Target Normal Sheath Acceleration (TNSA) on gold targets. The sample is then irradiated with x-rays from a laser-driven plasma backlighter of erbium, allowing for recording of absorption spectra. By fitting theoretical models and simulations to the experimental near-edge curves, WDM quantities can be extracted. For example, the electron temperature is determined through the variable slope of the K-edge, where a steeper slope indicates a lower temperature. Likewise, the electron temperature can be found by studying the far-edge structures, as shown in fig. 2.2b. In this experiment by Torchio *et al.* [16], iron samples are compressed and brought to WDM conditions through laser-driven shocks, then diagnosed with x-rays from a synchrotron beamline specialized for x-ray absorption techniques. By using a correlated Debye model, the electron temperature is determined. In addition, information about the atomic structure of the sample is gained by studying the disappearance of certain peaks. Notable is also the broadening of

EXAFS oscillations with increasing temperature, which is indicative of a collapse of atomic order in the material.

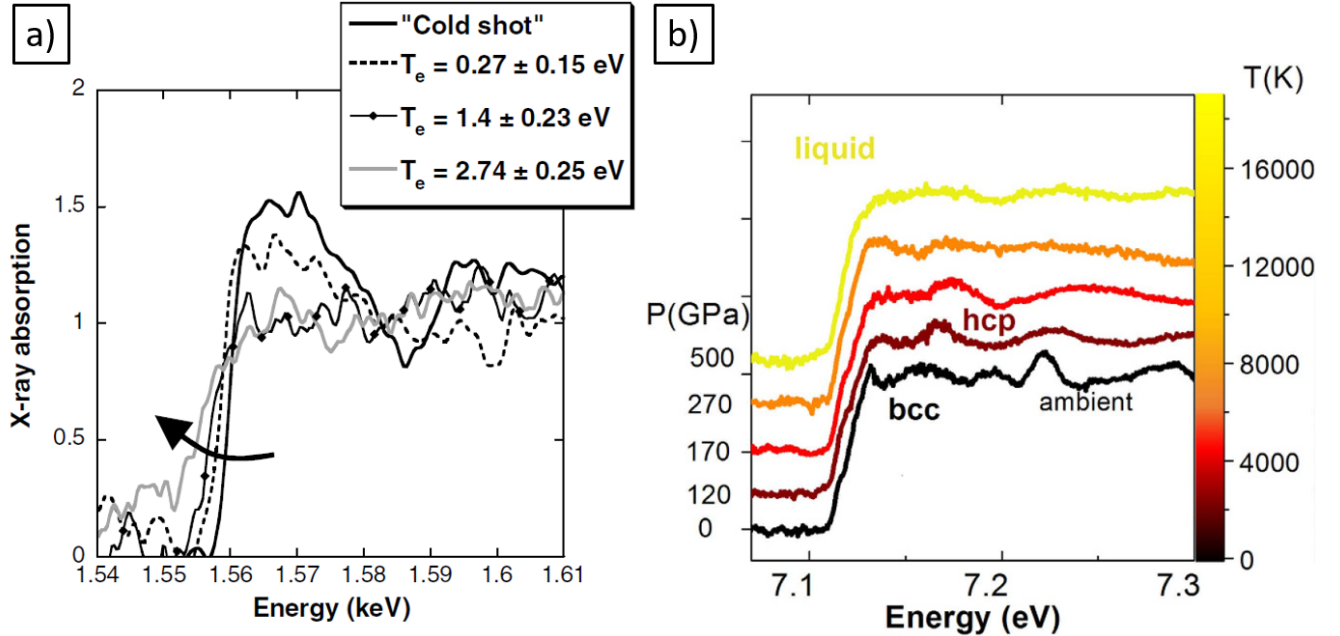


Figure 2.2.: Examples of XAFS spectra taken in WDM experiments for XANES and EXAFS respectively. It is important to note that the first graph displays absorption spectra of aluminum, while the second shows spectra of iron. **a)** Spectra from an aluminum sample isochorically heated to WDM conditions with energetic proton beam and diagnosed with x-rays from laser-driven plasma of erbium. XANES is applied to extract information about the electron temperature [21]. The arrow highlights the reduction of the K-edge slope with rising temperature. **b)** Spectra from an iron sample brought to WDM conditions with a laser-driven shock and investigated with x-rays generated by a synchrotron. EXAFS is conducted to derive the temperature and lattice structure of the samples. Note that the spectra are artificially shifted along the y-axis to represent rising pressure. [16].

Both of these results exemplify the power of XAFS as a diagnostic method for warm dense matter. As with most experiments in this vein, this method is made possible by x-ray spectrometers. Due to a number of restrictions originating from inherent properties of these devices and the volatile nature of WDM, the design of these spectrometers is essential for experimental success. As such, I will go into more depth on their history and design in the following chapter.

3. Fundamentals of X-Ray Spectrometers

Since its inception in 1914 [35], x-ray spectrometers have developed into an indispensable tool for plasma and high-energy density matter research [26]. This can be attributed in part to the unique challenges presented by x-rays and their interaction with matter. Conventional optics cannot be applied, as no absorption free materials are available and sufficient reflectivity is only achieved with grazing-angle incidence, greatly increasing optical aberrations [25]. By necessity, the entire optics of the spectrometers must therefore be realized using as few components as possible. In most cases, this limits the components to three; the x-ray source, the detector, and the dispersive element, which spatially separates the photons according to their energies and in most cases consists of one reflecting surface, as each new surface reduces the intensity of the x-rays on detector. In light of these limitations, x-ray spectrometers are generally designed with the specific experimental scheme and goals in mind and optimized using ray-tracing codes [26].

Central to the function of these spectrometers is the dispersive element. For energies below 250 eV, gratings are generally used, owing to their high reflectivity, while for x-rays from 250 eV -100 keV, and therefore for this work, crystals are more suitable [26]. The spectral dispersion of the x-rays occurs upon reflection on the dispersive element, where optical path differences between incident photons lead to interference. If this difference corresponds to multiples of the photon's wavelength, there is constructive interference, while the reflected intensity of other wavelengths is suppressed. As the optical path difference depends on the incident angle, photons are dispersed according to wavelength. In the case of crystals, this dependence is expressed by Bragg's law [36]

$$n\lambda = 2d_l \sin(\theta), \quad (3.1)$$

where n is the diffraction order, λ the wavelength, d_l the lattice constant, and θ the grazing angle.

In this work I will categorize the wide variety of spectrometer designs into two types; flat crystal and bent crystal. Crystals can be one-dimensionally bent, for example cylindrically, or two-dimensionally, i.e. conanically or spherically. The type and degree of bending is limited by the crystal material and available production methods [25]. Typically, flat crystal spectrometers offer simplicity, ease of build, and more crystal material choice with fewer defects, while bent crystal spectrometers exhibit lower background, more flexible geometries, and potentially high resolution and intensity on detector [25, 26]. As a result, improved signal-to-noise ratios are expected for bent crystal designs, at the cost of more complicated schemes and potential for crystal defects. Also to note is that bent crystals have the potential for imaging.

In this section, I aim to introduce the background and fundamentals needed for this work. First in section 2.1, the flat crystal design is briefly outlined and explained, also serving as a baseline used to introduce some important quantities. In section 2.2, bent crystal designs are discussed, including an overview of the von-Hamos geometry and a more detailed explanation of the Focusing Spectrograph with Spatial Resolution (FSSR) geometry. Then, in section 2.3, the calculations for the dispersion of the spectrometer geometries used in the experiment are shown. Lastly, the influences on the resolution are discussed in section 2.4.

3.1. Flat Crystal Geometries

An example of a flat crystal spectrometer geometry is shown in fig. 3.1, where the Bragg angle of the central energy, corresponding to the ray incident on the center of the detector, is given as θ_0 and a Bragg angle of an arbitrary wavelength as θ . For every incident angle on the crystal, only one wavelength fulfills the Bragg condition, so that the rays are dispersed on the detector with a dispersion $d(E)$, where d gives the location of the rays on the detector. This dispersion equation is essential for processing of the spectra from raw data, and is therefore to be calculated or, for more elaborate geometries, determined using ray-tracing procedures.

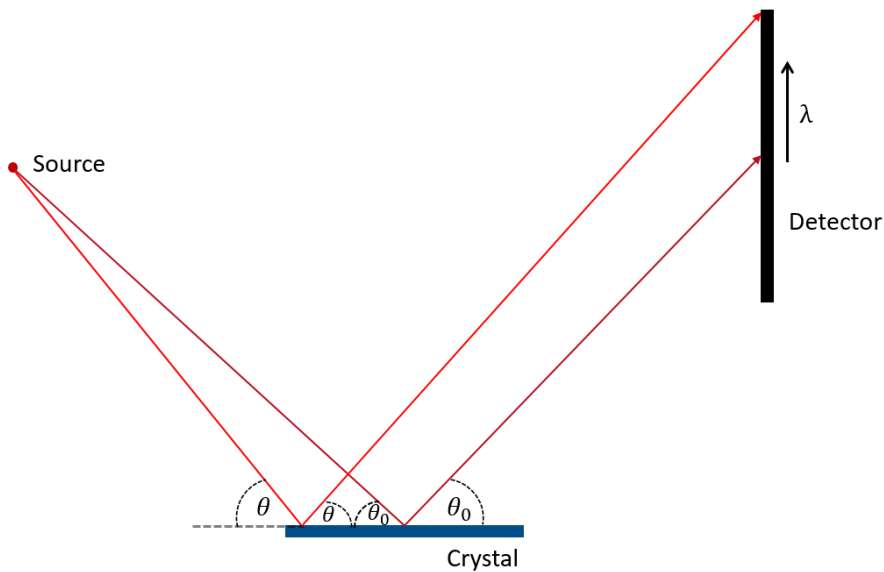


Figure 3.1.: Schematic geometry of a spectrometer with a flat crystal.

Currently, flat crystal spectrometers are typically eschewed in favor of bent crystal in the context of high-energy density matter experiments, attributed to the higher intensity on detector and reduction of source-size influences on the resolution of bent crystal schemes. If flat crystal schemes are used, they often come in as compact, easy-to-use mini-spectrometers, mostly serving supportive roles [26]. Notably, a novel group of flat crystal spectrometers shows promise, employing two vertically orientated plane crystals, but is not suitable for this work due to its lower collection efficiency [37]. Despite this outlook, flat crystal schemes could prove suitable if the experimental scheme covers the drawbacks, i.e. small source size and intense x-ray source, and a simple spectrometer scheme is desired.

3.2. Bent Crystal Geometries

Bending of the crystal allows for higher intensity on the detector, and therefore better signal-to-noise ratios, as the crystals collect the rays more effectively than their flat counterparts. Intuitively, this can be understood as more surface area of the crystal reflecting light of a certain wavelength onto the same approximate region on the detector. This comes at the cost of possibly worsening intrinsic reflection properties of the crystal [38], impacting the inherent resolution due to the crystal, though it is to note

that the focusing properties of the scheme can offset this impact [26]. Spherical crystals often entail FSSR geometries, while cylindrical crystals are applied for von Hamos geometries. Though these are of course not the only possibilities, they are the geometries relevant for this work, and hence will be handled individually in the following.

INTENSITY DISCUSSION THAT VINCENT MENTIONED

3.2.1. Von Hamos Geometry

The von Hamos geometry is shown schematically in fig 3.2. In this case the components are placed such that the source and detector lie on the cylinder axis of the crystal. As a result, all rays emitted from a point source with the same incident angle on the crystal are focused onto the same point on the detector, regardless of where they are reflected on the circular arc. In effect, the geometry leads to one dimensional imaging of the source, with the spatial resolution along the y axis and spectral resolution in x direction in fig 3.2. With its high collection efficiency and 1-D imaging, this scheme is popular, but has the drawback of a shallow angle of incidence on the detector and sensitivity to source broadening in the dispersive direction [26].

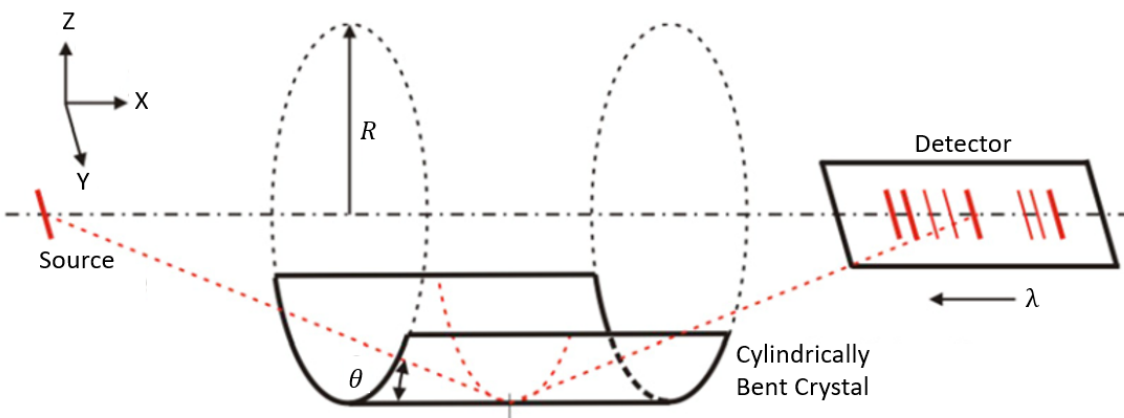
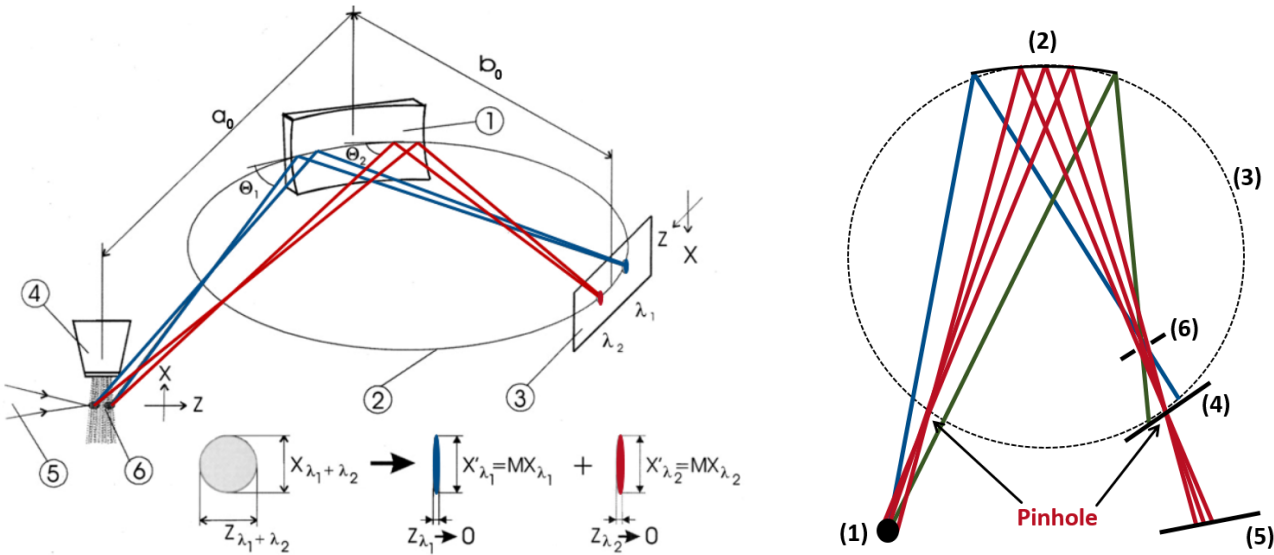


Figure 3.2.: Schematic representation of a spectrometer with von Hamos geometry. R represents the crystal curvature radius. [26]

3.2.2. Focusing Spectrograph with Spatial Resolution

The FSSR has become one of the most widely used spectrometer geometries in plasma diagnostics [36], since it offers high luminosity, spectral and spatial resolution, and relatively large energy ranges [26]. Its geometry is characterized by the use of a spherically bent crystal and is commonly separated into two variants, the FSSR-1D and FSSR-2D, whereby the suffix refers to the dimensions of the source imaging [26, 39]. Due to its comparable simplicity, the function of the FSSR-1D will first be described, followed by the FSSR-2D in the final paragraph.

Before discussing further, I need to make an aside about the terminology used here. When I refer to "imaging", I mean imaging in the sense of rays coming from an object plane being reflected in such a way



(a) Schematic depiction of the FSSR-1D spectrometer. (1) Spherically bent crystal, (2) Rowland circle, (3) detector, (4) target material source (in the diagram a gas, in this work a foil), (5) laser beam, (6) laser-produced plasma. Additionally the imaging of the source is shown on the bottom, where a 1D-image is formed for each wavelength. [39]

(b) Schematic comparison of the FSSR-1D and 2D configurations. (1) Source, (2) spherically bent crystal, (3) Rowland circle, (4) detector in FSSR-1D, (5) detector in FSSR-2D, (6) aperture at polychromatic crossover. Also pictured is the location of the pinhole-like points for the rays of a single wavelength, here in red.

Figure 3.3.: FSSR Schemes.

that an image is formed in the image plane, which depends on from where the rays were emitted. This is analogous to what occurs for lenses and curved mirrors, which is simply the result of refraction or reflection on a curved surface. Furthermore I will differentiate between "mirror imaging" and "pinhole imaging", referring to imaging due to mirror curvature in the first case and pinholes as in pinhole cameras in the second. On the other hand, "spectral focusing" refers to the focusing of the rays of the same wavelength, but from different origins, onto a single point. This is in essence different from imaging, since it does not inherently form an image, although both cases involve a form of focusing.

A schematic representation of the geometry can be found in fig. 3.3a. To explain the workings of the FSSR-1D, it is instructive to define two distinct planes, as the properties of the spectrometer change between them. In this work they are denoted as the dispersive plane, containing the direction of dispersion and the circle depicted in fig 3.3a, and the vertical plane, which is perpendicular to the dispersive plane and includes the detector surface. In the literature these planes are often referred to as the meridional (dispersive) and sagittal (vertical) planes [26, 36]. First, I will focus on the dispersive plane.

An important concept to this configuration in the dispersive plane is Johann geometry [40], which utilizes the so-called Rowland circle (RC) (see fig. 3.3), defined as a circle tangential to the spherical crystal at its midpoint with the radius $R/2$, where R is the radius of the crystal curvature. According to this geometry, any ray with a given wavelength that passes through a certain point on the RC fulfills the Bragg condition everywhere on the crystal surface and is focused in first approximation onto another point on the RC, mirrored across the crystal curvature pole. All other rays of this wavelength, which do not pass through this point, do not fulfill Bragg's law anywhere on the crystal and are hence not reflected. This effectively results in spectral focusing of the light onto the RC independent of where the rays are emitted. This is

schematically illustrated in fig. 3.3a, where the red and blue rays indicate different wavelengths. To note here is also that placing the detector on the RC is the defining feature of the FSSR-1D [41].

For both planes, an additional important aspect is mirror imaging properties originating from the spherical bending, comparable to imaging from a concave mirror and therefore in itself independent of wavelength. There are two focal lengths, one for each plane, which result from astigmatism due to the off-axis location of the source with respect to the crystal. The imaging condition, which follows from the mirror equation, in the vertical plane is [39]

$$\frac{1}{a} + \frac{1}{b} = \frac{(2 \cos(\alpha))}{R}, \quad (3.2)$$

where, for a given ray, the distance between emission point and crystal incidence is denoted as a , the distance between crystal incidence and detector incidence as b and the Bragg angle as θ , with $\alpha = 90^\circ - \theta$. To achieve the best possible spectral resolution, the source-crystal distance a_0 , where the index 0 refers to the central ray, and the crystal-detector distance b_0 are chosen so that eq. 3.2 is satisfied [26, 39, 42]. This ensures sharp imaging in the vertical plane. It is important to note that for the FSSR-1D, there is no imaging on the detector in the dispersive plane, as the detector lies on the point of spectral focusing. Despite this, the mirror imaging in the dispersive plane (see [39]) does lead to a convergence of rays of different wavelengths onto a region between detector and crystal. By placing an aperture on this region, referred to as the polychromatic crossover (see fig. 3.3b), extraneous rays are blocked, reducing the background on the detector [26]. Through mirror imaging and spectral focusing, the FSSR-1D produces a series of 1D, spectrally distinguished images on the detector, as depicted in the bottom of fig. 3.3a.

The other variant is the FSSR-2D, in which case the detector is placed anywhere not on the RC [42]. If the detector and source lie outside of the RC, pinhole imaging for each wavelength is realized in the dispersive plane. The "pinholes" are a result of the spectral focusing and are located on the RC as labeled in fig. 3.3b. A good way to imagine this is by removing everything inside the RC and bringing the "pinholes" together, forming a typical pinhole camera setup for each wavelength. Hence the magnification in the dispersive direction depends on the distance of the source and detector respectively to the RC [26]. This pinhole imaging in the dispersive plane, along with mirror imaging in the vertical plane, results in a series of 2D spectrally selected images on the detector with different magnifications in each plane [43]. In general, the 1D configuration yields the highest possible spectral resolution, since there is minimal overlap of energies due to spectral focusing, while the 2D setup allows for 2D quasi-monochromatic imaging of the source at the cost of reduced spectral resolution [26]. Accordingly, the FSSR-2D setup is suitable for use with a source that emits a quasi-discrete spectrum, as a continuous spectrum would lead to a continuous set of 2D-images, leading to very low spectral resolution.

3.3. Dispersion Calculation

The dispersion $d(E)$ of a spectrometer shows the relation between a spatial coordinate and the energies of the photons. In this work I use d for the coordinate, defined as pictured in fig. 3.4. Therefore $d(E)$ quantifies where each photon with energy E is expected to land on the detector dispersive line for a given spectrometer configuration. Generally speaking, an approximately linear dispersion is desirable, since it simplifies data processing and ensures an even spread of energies on the detector, so that no information is lost due to variable resolution [36]. I will calculate the dispersion for the two geometries used in this work, namely for the flat crystal geometry found in fig. 3.1 and the FSSR as depicted in fig. 3.3b.

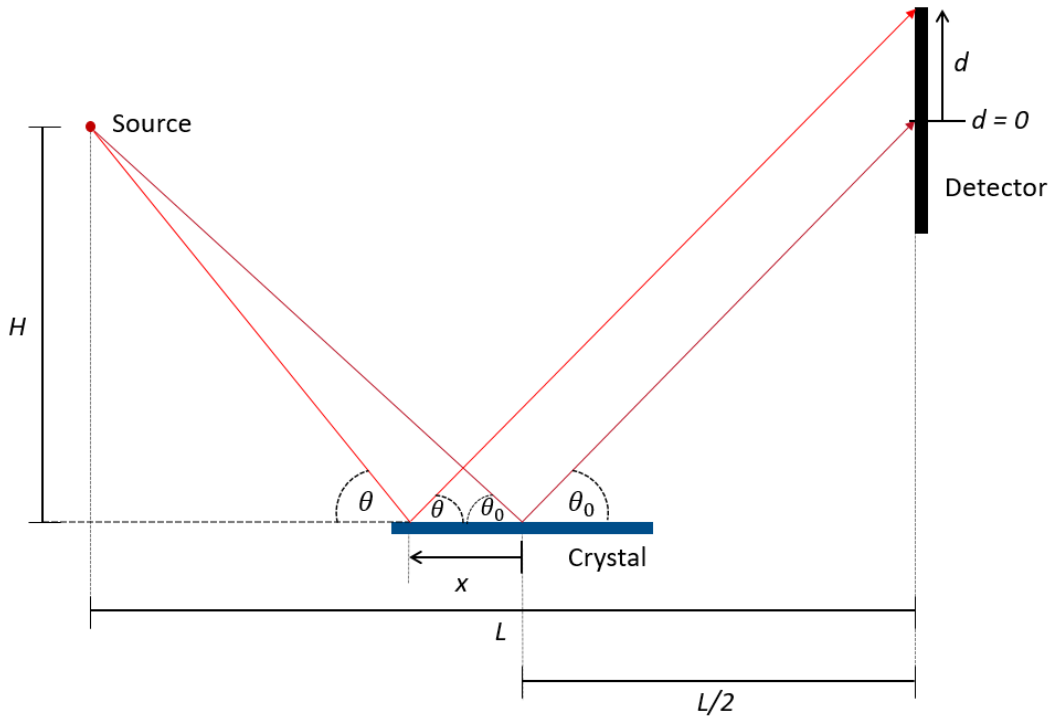


Figure 3.4.: Schematic representation of a flat crystal geometry with the detector perpendicular to the crystal surface. d is defined as lying on the intersection of the dispersive plane and detector surface, with its origin on the location of the central ray, corresponding to θ_0 , on the detector. x is the distance between the incident points of a given ray and of the central ray on the crystal in the dispersive plane. H is the height of the spectrometer, i.e., the vertical distance from the source to the crystal surface, and L is the length of the spectrometer, i.e., the source-detector distance.

I will calculate the dispersion for the flat crystal configuration using trigonometry and the Bragg condition. The parameters used can be referenced from fig. 3.4. From the path of the non-central ray in the diagram with the Bragg angle θ , I get the two relations

$$\tan \theta = \frac{H + d}{\frac{L}{2} + x} \quad (3.3a)$$

$$\tan \theta = \frac{H}{\frac{L}{2} - x}. \quad (3.3b)$$

Setting the right hand sides equal to each other and solving for x yield

$$x = \frac{L}{2} \cdot \frac{d}{d + 2H}. \quad (3.4)$$

I then plug this into eq. 3.3a and simplify, which gives

$$\tan \theta = \frac{d}{L} + \frac{H}{\frac{L}{2}}. \quad (3.5)$$

By identifying $\frac{H}{L/2} = \tan \theta_0$ and solving for d , I can write

$$d = L(\tan \theta - \tan \theta_0). \quad (3.6)$$

Finally, using Bragg's law (see eq. 3.1) and

$$\tan \theta = \frac{\sin \theta}{\sqrt{1 - \sin^2 \theta}} = \frac{1}{\sqrt{1/\sin^2 \theta - 1}}, \quad (3.7)$$

I receive the dispersion for the flat crystal geometry with detector perpendicular to the source

$$d(E) = L \left(\frac{1}{\sqrt{\left(\frac{2d_l}{nhc}\right)^2 E^2 - 1}} - \frac{1}{\sqrt{\left(\frac{2d_l}{nhc}\right)^2 E_0^2 - 1}} \right), \quad (3.8)$$

where E_0 denotes the energy of the central ray, h the Planck constant and c the speed of light, which is used in the conversion $\lambda = hc/E$. Consequently the dispersion is determined by four parameters in total: n , d_l , E_0 and L .

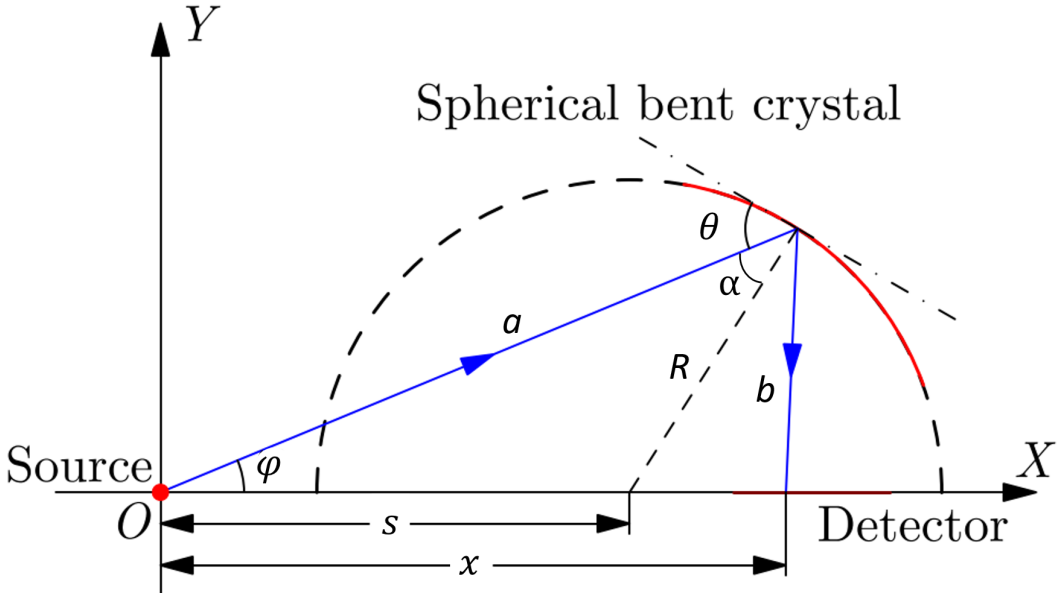


Figure 3.5.: Geometry of an FSSR spectrometer, labeled with quantities useful for analytical calculations. Note that this is generalized, so that it's applicable for both the FSSR-1D and 2D. [36]

Before calculating the FSSR dispersion, it is important to consider a restriction on the detector position. The dispersion line on the detector surface, which corresponds to d , must lie on a symmetry axis of the sphere drawn out from the crystal curvature and point towards the source, so that the imaging condition in the vertical plane (see eq. 3.2) is fulfilled for all photon energies. With this placement, the dispersion can be analytically calculated. Q. Yang *et. al.* [36] carried out this calculation employing the coordinate system and quantities found in fig. 3.5. For the dispersion $x(\varphi(\theta))$ they found

$$x = \frac{2s\chi(\chi + s \cos \varphi)}{\kappa}, \quad (3.9)$$

where

$$\begin{aligned} \chi &= (R^2 - s^2 \sin^2 \varphi)^{1/2} \\ \kappa &= 2\chi^2 + 2s\chi \cos \varphi - R^2. \end{aligned} \quad (3.10)$$

To bring $x(\varphi)$ into the form $d(E)$, I first express χ and κ in terms of α , which is related to the Bragg angle θ through the equation $\alpha = 90^\circ - \theta$. By taking advantage of the triangle traced out by R , a and s , I can write

$$\begin{aligned}\chi &= R \cos(\alpha) \\ \cos \varphi &= \frac{(a - R \cos \alpha)}{s}\end{aligned}\tag{3.11}$$

Plugging this into eq. 3.10 leads to

$$\begin{aligned}\kappa &= 2R^2 \cos^2 \alpha + 2sR \cos \alpha \cos \varphi - R^2 \\ &= 2R^2 \cos^2 \alpha + 2sR \cos \alpha \frac{(a - R \cos \alpha)}{s} - R^2 \\ &= 2Ra \cos \alpha - R^2.\end{aligned}\tag{3.12}$$

From this and $s = \sqrt{a^2 + R^2 - 2aR \cos \alpha}$ follows

$$x(\theta) = \frac{\sqrt{a^2 + R^2 - 2aR \sin \theta}}{1 - \frac{R}{2a \sin \theta}},\tag{3.13}$$

where $\cos \alpha = \sin \theta$ was used. The only implicit dependence on θ left in this equation is in $a(\theta)$. Using the same triangle from above and the fact that s is independent of θ , a can be written as

$$\begin{aligned}a &= R \sin \theta + \sqrt{R^2 \sin^2 \theta + s^2 - R^2} \\ \text{with } s &= \sqrt{a_0^2 + R^2 - 2a_0 R \sin \theta_0},\end{aligned}\tag{3.14}$$

where a_0 and θ_0 denote these values for the central ray. Note that for simplicity a_0 and θ_0 were chosen to calculate s , though any combination of a and θ can be used. To determine $d(E)$, I introduce a coordinate transform according to fig. 3.5 with $x_0 = x(\theta_0)$. In the case of a FSSR-1D geometry, x_0 is equivalent to $a_0 \sin(2\theta_0)$, owing to the right angle of the central ray with the detector surface. Accordingly d can be written as

$$d = x - x_0.\tag{3.15}$$

Applying this transform, Bragg's law as in eq. 3.1 and converting from λ to E as before finally yields

$$d(E) = \frac{\sqrt{a^2 + R^2 - \frac{2Rnhc}{(2d_l)} \cdot \frac{a}{E}}}{1 - \frac{R(2d_l)}{2nhc} \cdot \frac{E}{a}} - x_0,\tag{3.16}$$

where

$$\begin{aligned}a &= \frac{Rnhc}{(2d_l)} \cdot \frac{1}{E} + \sqrt{\left(\frac{Rnhc}{(2d_l)}\right)^2 \cdot \frac{1}{E^2} + s^2 - R^2} \\ \text{with } s &= \sqrt{a_0^2 + R^2 - \frac{2a_0 Rnhc}{(2d_l)} \frac{1}{E_0}}.\end{aligned}\tag{3.17}$$

Therefore, the quantities required to find the dispersion $d(E)$ of an FSSR are the crystal curvature radius R and lattice constant d_l , diffraction order n , central photon energy E_0 , central Bragg angle θ_0 and source-crystal distance a_0 . To note is that this result is applicable for both the FSSR-1D and 2D.

3.4. Resolution

In general, the resolution of a spectrometer mainly depends on three factors [26, 41], which will be discussed in this section:

1. Source broadening
2. Intrinsic crystal properties
3. Detector resolution

Which of these has the greatest effect on the resolution depends on the choice of geometry, crystal and detector.

Source broadening refers to the effect the physical size of the source has on the resolution. For example, in the flat crystal geometry a larger source corresponds to a larger area covered by x-rays of the same wavelength on the detector, leading to worse resolution. This factor is strongly dependent on the geometry and crystal shape. Generally, the resolution of flat crystal spectrometers is strongly affected by source broadening, while FSSR spectrometers suppress the influence of source size [26].

The crystal properties that mainly affect resolution are structural in nature. The crystal structure influence is parameterized by the rocking curve width $\Delta\theta$, which is given by the FWHM of the reflected intensity as a function of incident angle and depends on wavelength and polarization of the radiation, crystal perfectness and bending radius [26, 38]. The reflection properties, mainly affecting the intensity on detector, are assessed using the integrated reflectivity R_{int} , i.e., the ratio of the angular intensity $I(\theta)$ integrated over the range of diffraction angles around a Bragg angle $\theta_B \pm \Delta\theta$ and the incident intensity I_0 [38]

$$R_{int} = \frac{1}{I_0} \int_{\theta_B - \Delta\theta}^{\theta_B + \Delta\theta} I d\theta. \quad (3.18)$$

Both these quantities can be calculated using the dynamical theory of X-ray diffraction [38]. In this work the following formula will be used to estimate the ratio of integrated reflectivity for a given setup,

$$R_{int} = \frac{N_{det}}{N_{total}} \frac{4\pi D}{\Delta x_{pix}}, \quad (3.19)$$

where N_{total} represents the total number of photons emitted by the source in the energy range, often corresponding to an emission line, D the distance over which the x-rays diverge (for example, the optical path length from source to detector for flat crystal geometries), and Δx_{pix} the pixel width in dispersive direction. N_{det} corresponds to the number of photons detected over the same energy range as N_{total} , corrected for filter transmission and detector sensitivity [44]. Note that a high resolution usually implies a low R_{int} and therefore weaker signals on the detector. With these quantities the effect of the crystal on the resolution can be estimated.

Another factor for the spectrometer resolution is the detector spatial resolution. This can be estimated simply by using the dispersion $d(E)$ and spatial resolution dx of the detector. In this work this takes the form of pixel density on a CCD camera. This is often the limiting factor for FSSR spectrometers [26, 41], though this should be calculated on a case to case basis, as geometry design choices also impact this factor.

For geometries capable of imaging, one can differentiate between spatial and spectral resolution. The spectral resolution is given directly by the energy interval corresponding to the area covered on the detector

by X-rays of the same wavelength, while the spatial resolution results from the imaged source size on the detector and is only limited by deviation from the imaging condition for different locations on the X-ray source.

In the case of the von Hamos geometry, the spectral resolution is sensitive to source broadening in both x and z directions, as depicted in fig. 3.2, while the spatial resolution along the y axis remains unaffected [26]. For the FSSR-1D, the spectral resolution is independent of source size due to the spectral focusing in the dispersive plane, a property that applies for the spatial resolution in the vertical plane as well, owing to the large a distance relative to the typical source size in laser plasma experiments. In the FSSR-2D scheme, the optimal spectral focusing condition is no longer met, therefore a finite source size leads to source broadening in spectral direction as well. [41]. A geometrical calculation of the impact of source size on spectral resolution for the FSSR scheme can be found in [45].

4. Spectrometer Design

As stated in the introduction, the overarching goal is the eventual characterization of warm dense matter of aluminum. The WDM will be induced using a heavy-ion beam, leading to rapid and fairly homogeneous heating compared to other techniques, like laser-driven shock or proton beams. Since WDM is opaque to visible light, x-rays will be used for the main diagnostics. In this case, the source will be laser-driven plasma as a backlighter of the sample, distinguished by its tunability, high-brightness, and small angular dependence of the emission. Together, the laser-driven backlighter and heavy-ion beam heated WDM sample offer a relatively homogeneous setup, in reference to sample properties and x-ray spatial distribution. This homogeneity enhances the diagnostics in that approximately a single WDM state can be probed, reducing unknowns in the experiment. XAFS will be the diagnostic method of choice, a technique that notably enables measurements relating to the atomic structure of short-lived, non-crystalline matter. As previously outlined, x-ray spectrometers are ubiquitous in WDM experiments using XAFS, and here is no exception.

The design of the spectrometers must in essence accommodate each main aspect of the experiment. The heavy-ion heating places demands on the sample size to ensure homogeneity and induces large amounts of background, necessitating careful shielding. The laser-driven backscatterers impact the possible intensity and wavelength distribution of the x-ray source, such that the spectrometers must be adjusted accordingly. Finally, the use of XAFS sets restrictions on the photon energy range of the spectra and the resolution, as the features must be detected and resolved. The details of all these design considerations will be discussed shortly in the next section.

In this chapter I will discuss the designs of the spectrometers and their rationale, outlining the advantages and disadvantages of each. First, I will describe the considerations that informed the designs. Then, the geometries of each spectrometer will be introduced in detail. Finally, the specifications of the spectrometers will be given and a comparison carried out, summarizing the purpose of each design.

4.1. Design Considerations

For the design of the spectrometers I took five main considerations into account, which follow from the specific needs of the experimental setup:

1. **Energy Range:** As stated in the introduction, the main function of the spectrometers is to perform X-ray Absorption Fine Structure (XAFS) spectroscopy and resolve the aluminum K-edge at 1558.98 eV [46] and its features. Near edge structures (XANES) can be observed within 50 eV of the edge [33], while extended fine structures (EXAFS) can be measured as far as 250 eV above the Al K-edge [34], which consist mainly of several oscillations in the absorption coefficient [27]. This yields an energy range of approximately 1530 - 1810 eV, where the upper value is much less strict than the

lower and the lower value is adjusted upward if the spectral range of the spectrometer is mainly the immediate area of the K-edge.

2. **Sample Size:** The future heavy ion beam heating, although more homogeneous than other WDM production methods, still is partly inhomogeneous, since the energy deposited along the heavy ion beam propagation direction, denoted here as z , is not constant. This negatively impacts the absorption spectroscopy, and accordingly the sample temperature measurements through XAFS, as each transmission location on the sample along the z direction corresponds to a certain energy on the detector (see fig. 4.1). The setup must therefore be adjusted to heat the sample as homogeneously as possible, realized by carefully choosing the sample-source distance and sample size in z direction. This limit on sample size also introduces a restriction on the choice of central Bragg angle. Together, this leads to the following constraints: (1) the central Bragg angle cannot be too large, because, assuming a fixed energy range, a larger θ_0 requires a larger range of angles to cover all the energies compared to a smaller θ_0 . This is due to the proportionality $\lambda \propto \sin \theta$, in which larger wavelengths have smaller slopes. (2) The source-sample distance cannot be too small, as then the heavy ion beam would strike the laser target, nor too large, as that would require a larger sample size. The sample size is limited by the projection of the spectrometer angle range on the sample, as well as by the FWHM of the heavy ion beam transversal to z . A compromise between all these factors leads to a sample-source distance of 5 mm and a sample size in z direction of ≤ 1 mm. Fig. 4.1 illustrates the setup and gives the distances used in this work.
3. **Spectral Resolution:** The main requirement on the spectral resolution is that it be high enough to resolve XAFS structures. From the example spectrum given in fig. 2.2a, the required resolutions for XANES can be estimated. Practically, a spectral resolution of ≤ 1 eV is expected to resolve the Al K-edge sufficiently to carry out XANES, while ~ 10 eV is required for EXAFS, estimated from half of an oscillation period [27]. Spatial resolution is advantageous, but not a hard requirement.
4. **Intensity:** A high enough intensity to resolve the spectra and perform the absorption spectroscopy is necessary. In the design this comes into play in part through the length of the spectrometer and distance to the source. Additionally the choice of geometry and crystal play a role.
5. **Physical Size:** The spectrometers must fit in the HHT chamber. This restricts the physical length to under 0.55 m. There must also be space for the heavy ion beam in future experiments and the PHELIX beam.

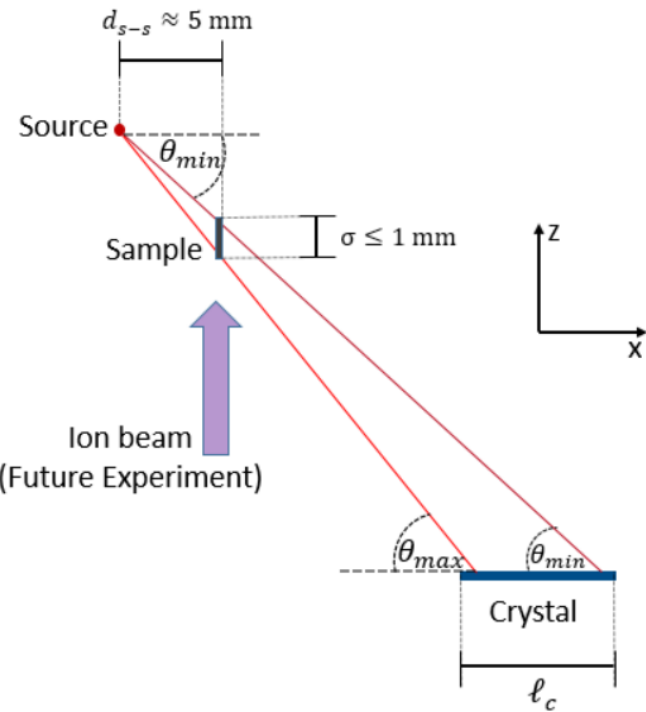


Figure 4.1: Illustration of the sample size consideration. The transmission length on the sample in z direction is denoted by σ , which must stay at or below 1 mm. θ_{max} and θ_{min} correspond to the maximum and minimum Bragg angles of the spectrometer respectively, while ℓ_c represents the length of the crystal in the dispersive plane and d_{s-s} the source-sample distance.

4.2. Implemented Spectrometer Schemes

I chose two configurations according to the considerations above and the aspects discussed in the introduction to this chapter, namely a flat crystal geometry (see fig. 3.1) and a bent crystal scheme, specifically a FSSR-1D geometry (see fig. 3.3). For the flat crystal spectrometer, inspiration was drawn from [27] and a dual channel geometry was chosen, so that both the absorption and source spectrum could be simultaneously measured on a single detector. A flat crystal design has potential in light of the small source size in the form of a laser-driven plasma ($\approx 150 \mu\text{m}$) and possibility of intense emission thanks to the source's tunability. This helps to alleviate the inherent disadvantages of a flat crystal geometry outlined in section 3.1.

As for the bent crystal scheme, the FSSR-1D geometry offers the highest possible spectral resolution of FSSR schemes while also giving high luminosity on detector. Additionally, it has the potential for 1D imaging in the vertical direction, which could be exploited to simultaneously observe the source and absorption spectra. I also considered a FSSR-2D configuration, but decided against it because some source spectra are expected to be continuous, which would significantly impact the spectral resolution. A von Hamos geometry was discarded because of its aforementioned shallow incidence angle on the detector and sensitivity to source broadening, which is altogether absent in the FSSR-1D scheme.

The crystals for each scheme were chosen according to the considerations listed in the appendix (section I). In the end, I decided on using ammonium dihydrogen phosphate (ADP) for the flat crystal geometry

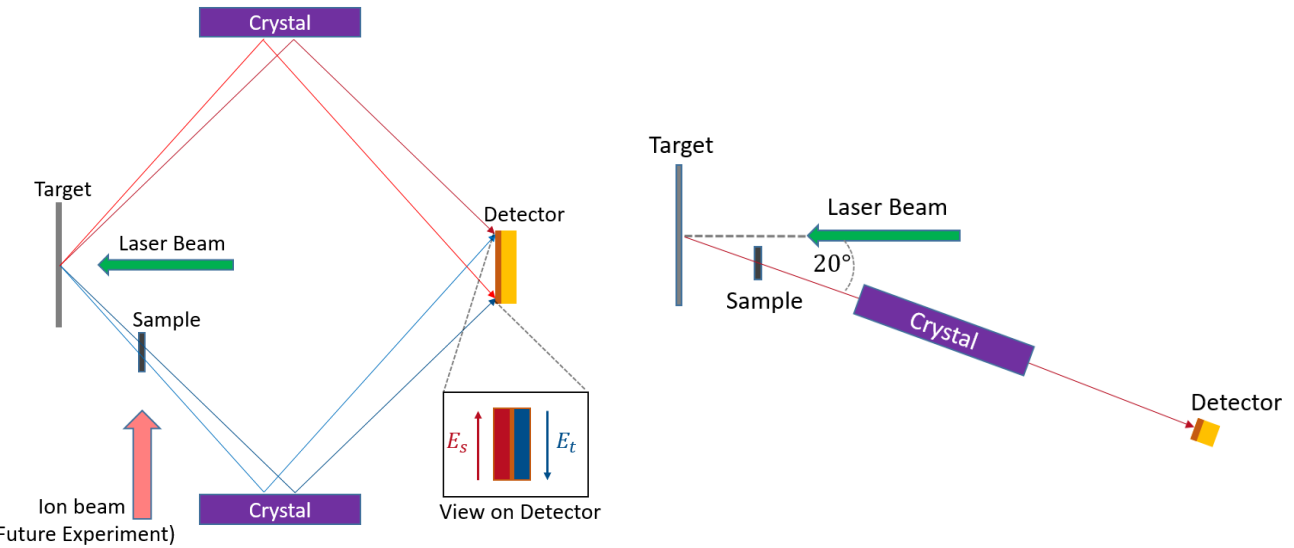
and mica for the bent crystal. ADP was chosen mainly for its potential to reach extremely high optical and structural perfection as well as its lattice spacing of $2d_l = 10.64 \text{ \AA}$, allowing for diffraction in the first order, covering the desired energy range [47, 48]. Mica was chosen for the FSSR-1D geometry for its bendability, high spectral resolution in tandem with good reflectivity, a wealth of previous applications in the literature and the possibility to use a low diffraction order (second order), yielding $2d_l/n = 19.84/2 \text{ \AA} = 9.92 \text{ \AA}$. [26, 39, 41, 42]. One drawback of the mica crystal was that it contains aluminum, which could lead to a drop in reflectivity at the Al K-edge, though the expected decrease in intensity is not significant enough to exclude mica [49]. Mica is also often used in FSSR spectrometers with strong bending, reaching radii of down to 100 mm [41].

In addition to the two main spectrometers of this work, I will introduce another simple flat crystal spectrometer in section 4.2.3, whose purpose is to deliver a wide energy range overview spectrum of the x-ray source as a control. It uses a potassium acid phthalate (KAP) crystal. This crystal is commonly used in x-ray spectrometers and has a larger rocking curve width than ADP [25, 50]. As this spectrometer is straightforward and not of my design, I will only describe it briefly and give its specifications.

In the following, I will describe the spectrometers in more detail, leaving the specifications for the next section. To note is that for this work I will generally refer to the spectrometers by their geometries, whose basic layout is in principle independent of the chosen crystal and energy range. For ease of discussion, I will however make clear in the following subsections if I'm referring to the geometry or the spectrometer. After this, the geometry names will refer to the spectrometers as a whole.

4.2.1. Dual Unbent Crystal Spectrometer

The dual crystal spectrometer geometry, which I christened the **Dual Unbent Crystal SpeCtrometer (DUCC)**, is illustrated schematically in fig. 4.2. The central idea behind this geometry is to simultaneously record two spectra by implementing a mirror symmetrical two-channel design. This spatial symmetry ensures that the channels see the same source, assuming a conical symmetry of the plasma emission. Through the combination of the DUCC geometry and ADP crystal, the DUCC spectrometer will target XANES and therefore have a relatively small energy range. This allows for lower relative resolutions, further reducing the impact of source broadening.



(a) Top view including the ion beam, which will not yet be introduced in the experiment. The coverage of rays on the detector according to the origin is depicted above. E_s refers to the source spectrum, while E_t labels the transmission spectrum, corresponding to the bottom beam paths in fig. 4.2a. The red area on the detector shows the E_s coverage and the blue area the E_t coverage.

(b) Side view, in which the tilt of the spectrometer is illustrated.

Figure 4.2.: Schematic illustration of the DUCC geometry, not to scale.

In fig. 4.2a the top view of the DUCC geometry is schematically shown. The laser beam irradiates the target, igniting a plasma. This plasma then emits soft x-rays, whose spectrum is measured through the top channel using one half of the available detector surface. The transmission spectrum through the sample, in this work an aluminum foil, is recorded through the bottom channel on the other half of the chip surface. The separation of the two spectra on the chip is realized by a plate with two openings inserted into the beam path before the two channels overlap (not shown in fig). Space was left for the ion beam for future experiments, which is of course not present in this work. To note is that space is left in the center of the spectrometer for a large lead block, which in the future will serve to shield the detector from electrons and protons being emitted from the sample due to the interaction with the heavy ion beam. Fig. 4.2b depicts the 20° tilt of the DUCC spectrometer that I introduced to leave space for the laser beam, which is conical and has a half opening angle of $\pm 2.3^\circ$. The spectrometer components were also tilted to simplify the design and deliver the simplest possible profile on the detector.

4.2.2. Focusing Spectrograph with Spatial Resolution

The FSSR-1D configuration used for the spectrometer is depicted in fig. 4.3. As the fundamental geometry effectively functions equivalently to the one described in section 3.2.2, I will not elaborate in detail on it here and instead discuss the spectrometer as a whole, so a FSSR-1D geometry with mica crystal. The main focus of this spectrometer is to capture a larger energy range, aiming to additionally resolve the oscillations in the EXAFS in the absorption spectra, while maintaining a good spectral resolution. Furthermore, the larger source-crystal distance a_0 and relation with the crystal-detector distance b_0 (see eq. 3.2) allow freedom of placement in the chamber, as compared to the DUCC spectrometer. One potential drawback

is the necessity of careful alignment and exact positioning of the components to achieve high spectral resolution, owing to the innate focusing and imaging of the FSSR scheme.

To note is that the potential of the 1D imaging for absorption spectroscopy with a single detector is not applied here due to the ratio of a_0 to b_0 , leading to a magnification in the vertical plane of 0.22. This magnification combined with the small sample size σ renders an image too small to consistently differentiate between source and transmission spectra. Despite this, the imaging properties does find use in concentrating the x-rays from the plasma onto a single line in the dispersive direction on the detector, significantly reducing the effects of background, which will be especially advantageous in the future experiments with the heavy ion beam.

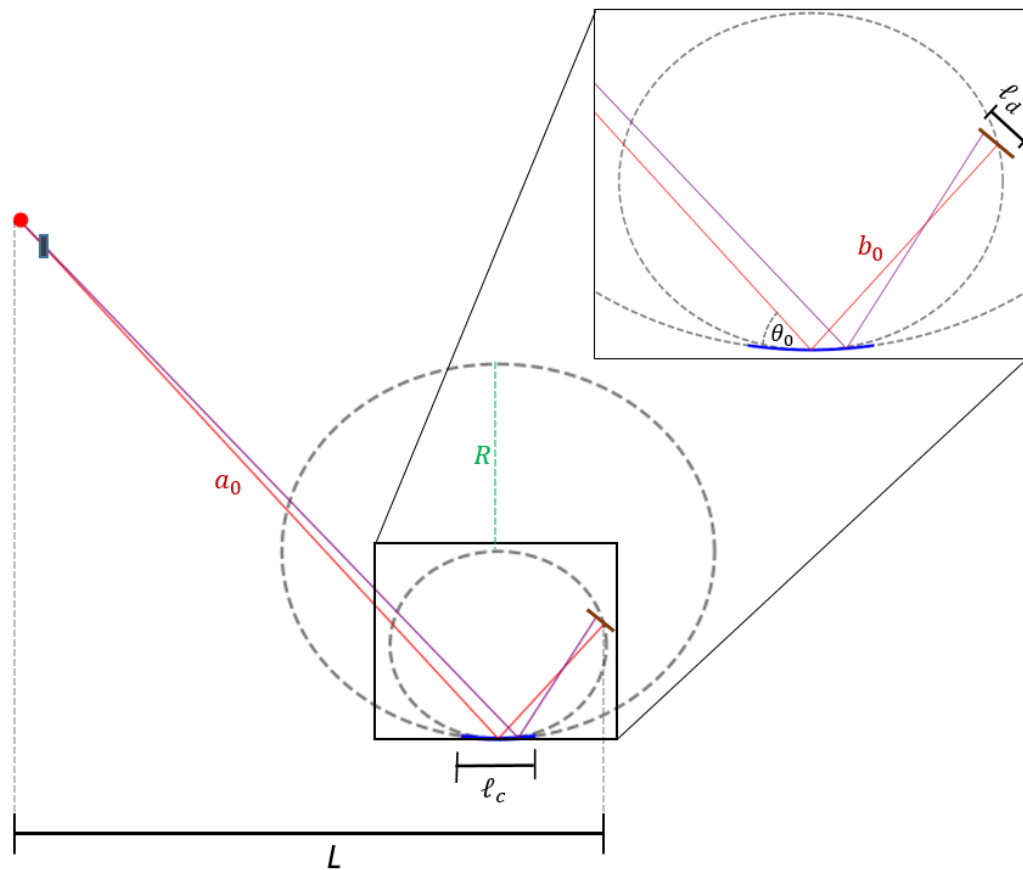


Figure 4.3.: Schematic Illustration of the FSSR-1D, where R is the radius of curvature of the crystal, L the spectrometer length, ℓ_c the length of the crystal in the dispersive plane and ℓ_d the detector length in dispersive direction. The crystal is depicted in blue, the source in red and the sample in dark gray. Note that the Rowland circle and circle drawn out by the crystal curvature are also shown.

4.2.3. Single Unbent Crystal Spectrometer

The **Single Unbent Crystal SpeCtrometer** (SUCC) is a basic spectrometer, consisting of a single, flat crystal set in a geometry analogous to fig. 3.1 or to the top channel of the DUCC geometry (see fig. 4.2a). Designed by P. Hesselbach, the spectrometer aims at a large enough energy range to cover both the FSSR-1D and DUCC spectrometer ranges, albeit at a lower resolution, owing to the source broadening intrinsic to the

flat crystal geometry and the worse crystal properties of KAP as compared to ADP. To note is that this higher rocking curve width also increases the intensity on the detector, ensuring that control spectra are consistently recorded. Its role as a control implies that it will not be used for transmitted spectra.

In addition to the SUCC, another spectrometer by the name of old SUCC (OSUCC), a device used in a previous experiment and also designed by P. Hesselbach applying the same basic design as the SUCC, is used to extract spectra transmitted through a sample. The main purpose of the OSUCC in the experiment is to investigate the other aspects of the experimental setup by using an already tested spectrometer. In this work, it is used only when presenting qualitative results.

4.3. Specifications and Comparison

Now that the specific geometries and crystal choices are established, I will introduce the specifications of each spectrometer and use them to validate that the considerations are fulfilled, as well as compare the spectrometers. The parameters are listed in table 4.2. In the table, the first six parameters are directly relevant to the considerations presented in section 4.1, where all but the spectral resolution follow directly from geometrical calculations. The spectral resolutions are derived using simulations conducted with the python3 code *mmpxrt* from Michal Šmíd [51], the results of which are given in table 4.1. For details on these simulations and path to the final resolution values, see section II in the appendix. In summary, the resolutions are calculated from three contributions: source broadening, detector resolution, and broadening from crystal properties. For the DUCC, the greatest contribution is due to source broadening, while for the FSSR-1D the crystal properties have by far the greatest impact. Additionally, the dispersion for each spectrometer is determined from the simulations, and for the FSSR-1D with a simple ray-tracing code written by me, and compared to the analytical dispersions from section 3.3. For both spectrometers, the analytical and simulated dispersions show excellent agreement and are approximately linear, with the three different derivations for the FSSR-1D dispersion displaying near perfect overlap.

Table 4.1.: Resolution contributions for the DUCC and FSSR-1D spectrometers. In both cases, the source broadening is taken from an *mmpxrt* simulation and assumes a source size of 150 μm , and the detector resolution is calculated from the *mmpxrt* dispersion and uses a pixel size of 13.5 μm . The contribution due to the crystal properties for the DUCC is estimated as described in section iii, while for the FSSR-1D it is taken from *mmpxrt*'s second ΔE value. The total spectral resolution is calculated by using error propagation on the source broadening and crystal properties' resolution, then linearly adding on the detector resolution.

ΔE Contributions	DUCC	FSSR-1D
Source Broadening	0.621 eV	0.014 eV
Detector	0.038 eV	0.143 eV
Crystal Properties	0.238 eV	2.954 eV
Total	0.703 eV	3.097 eV

The DUCC with ADP crystals aims to resolve a narrow energy range around the Al K-edge as well as possible to conduct XANES. Consequently, this design successfully fulfills the energy range consideration. The

sample size in z direction σ is calculated using the geometry in fig. 4.1, as well as assuming a source size in z direction s_z of 150 μm , which yields the equation

$$\sigma = (\tan \theta_{max} - \tan \theta_{min}) \cdot d_{s-s} + s_z, \quad (4.1)$$

where d_{s-s} corresponds to the source-sample distance and θ_{max} and θ_{min} to the maximum and minimum Bragg angle of the spectrometer. This equation, along with the values in table 4.2, result in a σ well below the upper limit of 1 mm, which together with the chosen θ_0 and d_{s-s} fulfill the sample size consideration. The spectral resolution falls in the desired range of ≤ 1 eV. The small distances from source to detector address the intensity consideration, while a spectrometer length of ≤ 550 mm complies with the physical size consideration.

Next, the validity of the FSSR-1D with mica crystal design will be assessed. With a maximum energy of 1755 eV, the spectrometer is within the range to conduct EXAFS, fulfilling the energy range consideration. As previously, σ , θ_0 and d_{s-s} all fall within the goal, with σ being only slightly larger than 1 mm, where in this case the sample size is determined using the 3D-model of the FSSR-1D in the HHT chamber, as the angle of the sample w.r.t. the crystal depends on the placement of the FSSR-1D in the experimental setup. Accordingly, the sample size consideration is also achieved. With an energy resolution of 3.097 eV, which is well under the requirement for EXAFS of 10 eV, the spectrometer fulfills the spectral resolution consideration as well. The intensity consideration is addressed by the properties of the FSSR geometry and the good intrinsic properties of mica [38, 41]. As with the DUCC, the FSSR-1D also fits well in the experimental chamber. Accordingly, all of the considerations outlined in the beginning of this chapter are fulfilled for both spectrometers.

I will now collect the arguments for each spectrometer interspersed throughout this chapter and present a comparison. Essentially for the purposes of this work, the question is whether to use a flat or bent crystal geometry, which depends also on the experimental conditions. The DUCC offers simplicity of design, easy alignment, and better crystal properties, at the cost of low collection efficiency and high sensitivity to source broadening. Conversely, the FSSR-1D boasts high collection efficiency, effective background reduction, and independence to source size, but is significantly more complex, difficult to align, and vulnerable to crystal defects caused by bending. As seen in table 4.2, for both spectrometers the relative resolution, i.e. $\Delta E/(E_{max} - E_{min})$, is approximately the same at $\approx 1\%$. The sample size σ and central Bragg angle θ_0 are also comparable. This implies that neither spectrometer distinguishes itself solely in terms of its specifications, besides the fact that the DUCC is intended for XANES and the FSSR-1D for EXAFS. In conclusion, the more advantageous design will be determined largely qualitatively from its performance in the preparatory experiment, assuming that the derived numbers prove accurate.

Lastly, I will address the SUCC and its role in this work. As is apparent from table 4.2, the SUCC covers a wider energy range than even the FSSR and therefore is intended for source characterization and acting as a control for the spectra of the DUCC and FSSR-1D. Another important aspect of this spectrometer is the chosen crystal, the KAP. This crystal has an approximately two times larger integrated reflectivity than the ADP (≈ 80 and 33 μrad respectively [52]), meaning that the SUCC's inherent resolution due to crystal properties is lower than the DUCC's, while simultaneously contributing to a higher intensity on detector. Consequently, a good signal to noise ratio is to be expected for most potential sources, further cementing its role as a control. Finally, this spectrometer design has been tested and vetted in previous experiments. As such, the SUCC can act as an effective backup, should either the DUCC or FSSR-1D have difficulties in the course of the experiment.

Table 4.2.: Parameters of the DUCC with ADP crystals, FSSR-1D with mica crystal, and SUCC with KAP crystal. All spectrometers use a CCD camera as a detector. The parameters directly significant to the design considerations are listed first, followed by values that set the final geometry but are not immediately relevant to the considerations. The spectral resolution is calculated using the results from section iv, summarized in table 4.1. Source size is assumed to be 150 μm . Sample size σ is determined using eq. 4.1 for the DUCC and directly from the 3-D model for the FSSR-1D.

Parameter	Denoted as	DUCC	FSSR-1D	SUCC
Energy Range	-	1541 - 1618 eV	1465 - 1755 eV	1400 - 1800 eV
Sample size (z)	σ	0.75 mm	1.07 mm	-
Source-Sample Distance	d_{s-s}	5 mm	5 mm	-
Central Bragg Angle	θ_0	47.58°	51.36°	17.23°
Spectral Resolution	ΔE	0.703 eV	3.097 eV	-
Spectrometer Length	L	235.17 mm	404.3 mm	325.22 mm
Bragg Angle Range	-	46.01 - 49.14°	45.4 - 58.53°	14.99 - 19.42°
Source-crystal Distance	a_0	174.10 mm	549.71 mm	170.26 mm
Crystal-detector Distance	b_0	174.10 mm	121.11 mm	170.26 mm
Detector Length	ℓ_d	27.6 mm	27.6 mm	27.6 mm
Detector Width	-	6.9 mm	6.9 mm	6.9 mm
Crystal Length	ℓ_c	40 mm	50 mm	50 mm
Crystal Width	-	30 mm	10 mm	20 mm
Crystal Radius	R	-	155.04 mm	-

5. Experimental Setup

Now that the spectrometer designs and important background information are established, I will describe the experimental setup for the laser-only experiment of May 2023 at the High energy, High Temperature experimental station (HHT) of GSI. To reiterate, this experiment is conducted to prepare for a combined experiment, so using PHELIX and the SIS-18 heavy ion synchrotron, in 2024, which is in itself a preparation for eventual combined experiments at the currently in construction FAIR facility, specifically at the APPA cave. This future endeavor will be capable of producing WDM samples through heavy-ion beam heating using the SIS-100, applying the novel combination of laser-driven plasma as backscatterers and heavy-ion heated WDM. The basic experimental scheme is illustrated in the introduction in fig. **REFERENCE WHEN IS CREATED.**

The main goals of the 2023 experiment are to assess the performance of the spectrometers, test backscatterer materials, and to validate the setup as a whole. As the main focus of this work are the spectrometers, I will only schematically explain the general experimental setup in the first section, placing more of a focus on the mechanical design of the spectrometers themselves, which appear in the following section.

5.1. General Setup

The experimental setup, as shown schematically in fig. 5.1 and as an *Inventor* model in fig. 5.2, consists of five main components: the backscatterer target, aluminum sample, spectrometers, PHELIX beam, and focus diagnostics. To note is that the location of heavy-ion beam is also taken into account by the setup. Laser shots that use an aluminum sample are denoted as absorption shots, while reference shots without samples are called source shots. Additionally, a measurement event, initiated by a shot from the PHELIX laser, is referred to simply as an event. From each event results one set of spectra. In the following, I will describe each component individually as well as discuss how the measurements are generally conducted.

The backscatterer targets are irradiated with the PHELIX laser to form plasmas as x-ray sources for the sample diagnostics. To find an optimal backscatterer for future experiments, a variety of materials are tested, including the rare earths samarium (Sm), gadolinium (Gd), terbium (Tb) and dysprosium (Dy), along with polytetrafluoroethylene (PTFE), also known by the brand name teflon. In addition, and most relevant to this work, aluminum (Al) targets are shot, fulfilling the purpose of characterizing the spectrometers and validating the setup using a well-described emission source. All of the targets are rectangular foils with a variety of thicknesses: 100 μm for the rare earths, 120 μm for teflon and 20 μm or 50 μm for aluminum. The targets are affixed to holders placed on a target ladder and aligned to the target chamber center (TCC) for each event. These holders also position the aluminum samples at the aforementioned 5 mm away from the backscatterers.

These samples are penetrated by the x-rays, which are transmitted to the spectrometers. The location of the samples is such that they lie in the optical path of the FSSR-1D and the bottom channel (w.r.t fig. 5.1) of

the DUCC. Most of the samples have a thickness of 0.8 mm, with the exception of the first five transmission shots, which are 2 mm. The switch to 0.8 mm occurred due to the low intensity of the transmission spectra with the thicker samples. The samples remain unheated for the duration of the experiment, so that all transmission spectra are intended to be at ambient temperatures.

The spectrometers lie next on the path of the x-rays, whose mechanical design, with the exception of the SUCC, is discussed in the next sections in more detail. As seen in fig. 5.1, the layout is such that during a transmission shot, so with a sample, the FSSR-1D and bottom channel of the DUCC can record transmission spectra, while the SUCC and upper channel of the DUCC take the reference, or source, spectra. Due to the limitation of only having two x-ray cameras, the spectrometers are designed to be modular, with the cameras easily detachable. Generally speaking, one of these cameras is attached to the SUCC, yielding wide energy range reference spectra, while the other is on either the DUCC or FSSR-1D. Between shots, filters were often changed to accommodate different backscatter intensities, which depend on laser energy and backscatter material. In total, four filter materials were used: carbon, gold, pokalon, and polycarbonate. For each shot, a combination of filter types and thicknesses were chosen according to the backscatter and spectrometer. All the spectrometers are orientated so that they view the backscatter at the same radial angle, exploiting the assumed conical symmetry of the plasma emissions. As such, the SUCC is tilted upwards and positioned above the upper DUCC channel, along with the view of the FSSR-1D placed slightly above the lower channel of the DUCC. Consequently, only the FSSR-1D lies in the plane drawn by the PHELIX beam, backscatter, and sample. If the OSUCC is used, it replaces the FSSR-1D in the experimental scheme.

The PHELIX beam is focused onto the backscatter targets with ... **FILL IN SPECS HERE**. The focus diagnostics consist of an optical setup designed to image the TCC onto a camera that lies outside the vacuum chamber. It is used to align the targets and PHELIX beam to ensure clean shots. The chamber is evacuated to establish a vacuum and the x-ray cameras are cooled to near 0°C before each shot to protect the chips from condensation.

After event number 25 (of 75 total events), a phase plate was inserted into the PHELIX beam. With this, a random, spatially distributed phase was introduced, leading to a larger focus spot with a more homogeneous intensity distribution as compared to a Gaussian. Thus the fluctuation between shots was reduced and the homogeneity of the plasma improved.

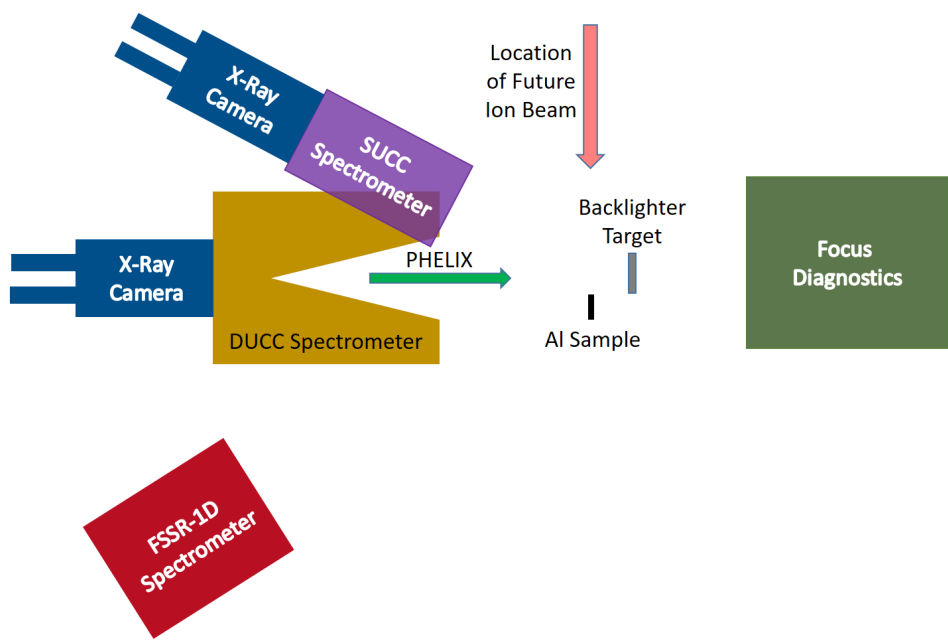


Figure 5.1.: Schematic illustration of the experimental setup. Note that the location of the heavy-ion beam for future experiments is marked, but of course not present in this experiment. The DUCC and SUCC spectrometers are not in the plane of the illustration, but tilted downwards and upwards respectively. The x-ray cameras can be freely transferred between the spectrometers.

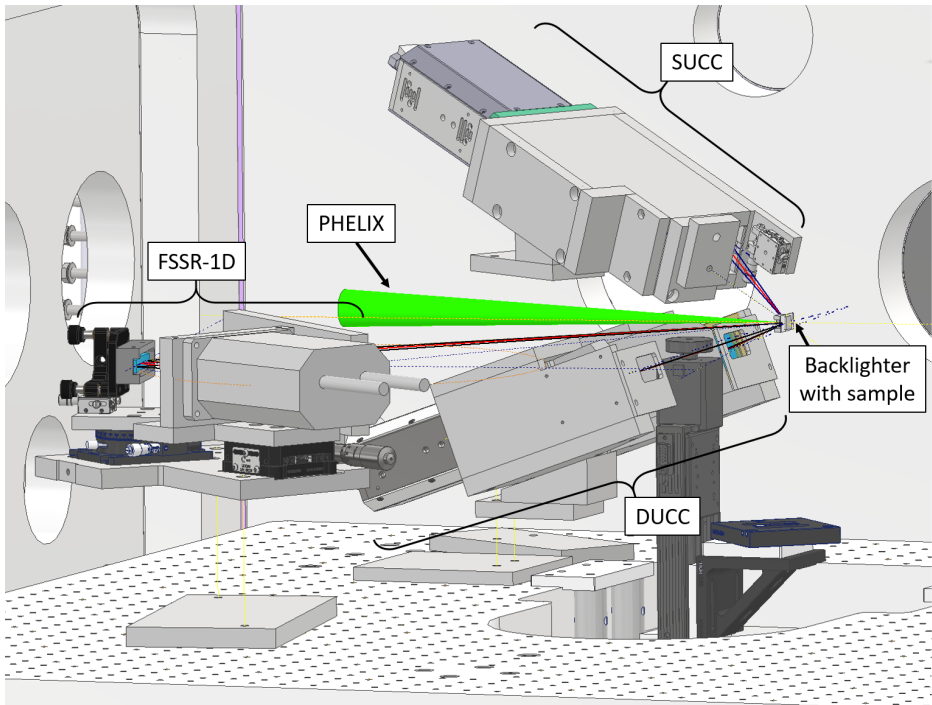


Figure 5.2.: *Inventor* model of the HHT chamber from the perspective of the bottom right of fig. 5.1 looking towards the spectrometers. The heavy-ion beam as well as the focus diagnostics are not pictured. The optical posts that connect the spectrometers to their bases are not shown, but their locations are depicted with thin yellow lines. Additionally, the optical paths in the dispersive direction for each spectrometer are shown in blue, with a red line for the central rays. In actuality the PHelix beam extends out of the chamber.

5.2. Mechanical Design of Spectrometers

ADD REAL PICTURES OF SPECTROMETERS

I based the mechanical design of the spectrometers around four goals. First, the devices must implement the designs presented in chapter 4 to an approximately ± 0.5 mm precision, ensuring that sufficient internal and external alignment to produce well-resolved spectra is achieved. Second, the crystal and camera chip must be sufficiently shielded while still maintaining enough intensity on the detector. Third, alignment of the spectrometer components to one another and the backlighter must be addressed. This requirement is more stringent for the FSSR-1D as a consequence of its focusing properties. Finally, the devices must be robust enough to withstand the harsh experimental conditions resulting from the heavy-ion beam and plasma. This mainly takes the form of heavy aluminum shielding, among others.

In this section, I will describe the mechanical designs of the DUCC and FSSR-1D, whose models are built in the CAD program *Autodesk Inventor 2020*. The SUCC will not be elaborated on, as it is not designed by me and generally shares a similar mechanical design philosophy with a single channel of the DUCC. All spectrometers are outfitted with in-vacuum CCD cameras from *greateyes* of the GE-VAC 2048 512 series as detectors. In the case of the DUCC, an adjusted camera with a thinner front plate is used to avoid clipping. The spectrometer parts are generally made of aluminum, unless otherwise specified.

5.2.1. Dual Unbent Crystal Spectrometer

The DUCC model is shown in fig. 5.3 with the parts color coded, which is presented in table 5.1, along with a summary of their functions and names. The most numerous parts are the ones responsible for shielding and structure. These protect the chip and crystals from debris, particles and extraneous rays. Also serving a shielding role is a pointer holder, whose main purpose is to hold the optical post for alignment purposes.

The blast shields, on which $2\text{ }\mu\text{m}$ Mylar foils are attached to the opening, protect the crystal from debris while allowing the x-rays through. Additionally, two carbon filters are glued onto the openings of the filter holder, which are light-tight and prevent visible light from reaching the chip. These carbon filters can be chosen to have an areal density of $\approx 200\text{ }\mu\text{g}/\text{cm}^2$ or $\approx 900\text{ }\mu\text{g}/\text{cm}^2$, depending on the intensities observed on the chips in the experiment. The filter holder also serves to spatially separate the two channels onto the chip, where the holes have a vertical separation of 1 mm so that a shadow will appear on the center line of the chip.

The ADP crystals are held in place by first placing them in a groove, then screwing on the crystal frames made of Trovidur. By attaching a plexiglass foil to the bottom of the groove and fabricating the frames out of plastic, the crystal is protected from direct contact with the aluminum housing. The 20° angle of the DUCC w.r.t. the PHELIX beam is implemented by an angled block of the foot. Finally, a venting channel is engraved into the plate attached to the camera, partially visible in fig. 5.3b. This channel is designed with random turns, similar to a snake, so that air can escape while light is kept out. This is essential to prevent the carbon filters from breaking during venting of the HHT chamber.

The alignment is realized by first affixing the pointer holder with screws to the top and bottom plates of the shielding, making sure to use the groove on the bottom plate to guarantee proper orientation. Then an optical post is set to the designed distance from the front surface of the pointer holder to the x-ray source. The post is attached to the pointer holder and the DUCC is brought into the chamber. Once the tip of the post is as close as possible to the laser-target interaction point, known as the target chamber center (TCC), the spectrometer is aligned, as the alignment of further degrees of freedom is guaranteed by the mechanical precision of the structural pieces, reaching the desired precision of $\pm 0.5\text{ mm}$.

Table 5.1.: Color code of the DUCC model with the functions and name of the parts.

Color	Function	Name
Light gray	Structural/Shielding	-
White (near source)	Protecting crystal	Blast shield
White (labeled)	Capturing spectra	Greateyes camera
Brown	Capturing spectra	Camera chip
Dark gray	Holding alignment post	Pointer holder
Red (front of camera)	Separating spectra/holding filter	Filter holder
Transparent yellow	Securing crystals	Crystal frame
Turquoise	Dispersion of rays	ADP crystal
Green	Supporting + tilting spectrometer	Foot with angled block
Beige	Display location of chamber floor	Breadboard floor
Red	-	Central ray
Black	-	Outer rays

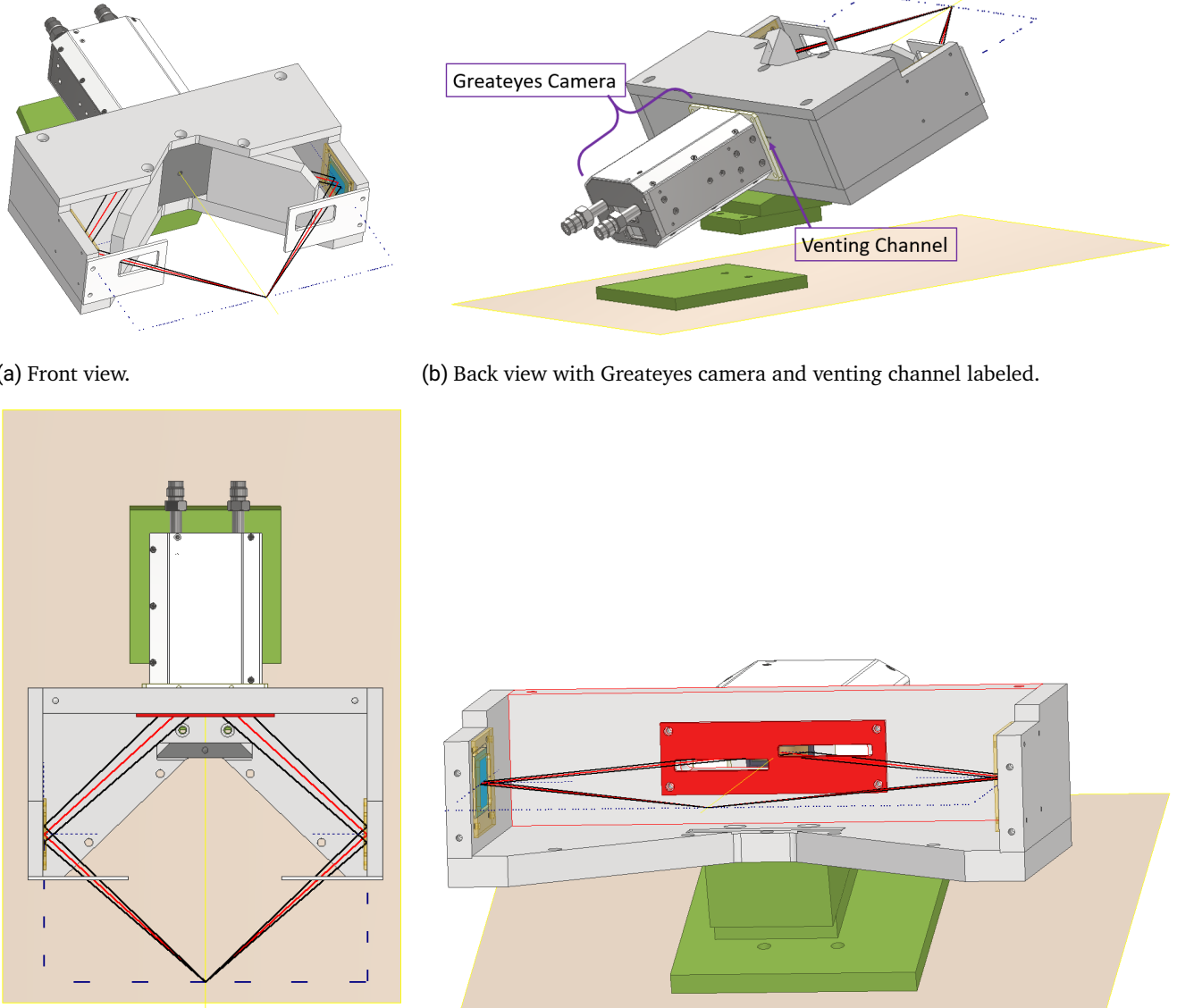


Figure 5.3.: CAD model of the DUCC. The parts are color coded, whose function and name are listed in table 5.1. The optical posts between the foot parts are not depicted.

5.2.2. Focusing Spectrograph with Spatial Resolution

In fig. 5.4 the FSSR-1D model is pictured with the parts color coded, presented in table 5.2 with a summary of their functions and names. The shielding in this setup is mainly taken care of by the front plate closest to TCC. A snout, formed by three plates, adds additional shielding in front of the chip, as well as functioning as an aperture at the polychromatic crossover as described in section 3.2.2. Inside the snout is the carbon filter holder, which fulfills the same role as with the DUCC, except this time using only the $\approx 900 \mu\text{g}/\text{cm}^2$ carbon filter. Additionally, a blast shield is attached to the front plate, set up the same way as in the DUCC. The crystal itself was originally planned to be fixed by the crystal holder, designed in such a way that the

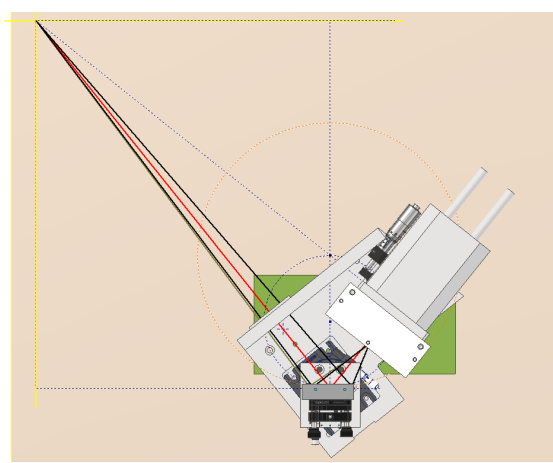
reflecting surface does not come into contact with anything. In the experiment, this holder couldn't be used, as the mica crystal was a different one than planned, namely one that came in its own holder.

Shown in fig. 5.4 are also optical stages utilized for the alignment procedure, which must be more exacting than that of the DUCC, owing to the curvature of the crystal and therefore the imaging and focusing properties. As the alignment is an involved process using additional components not pictured in fig. 5.4, it is described in detail in the appendix, section III.

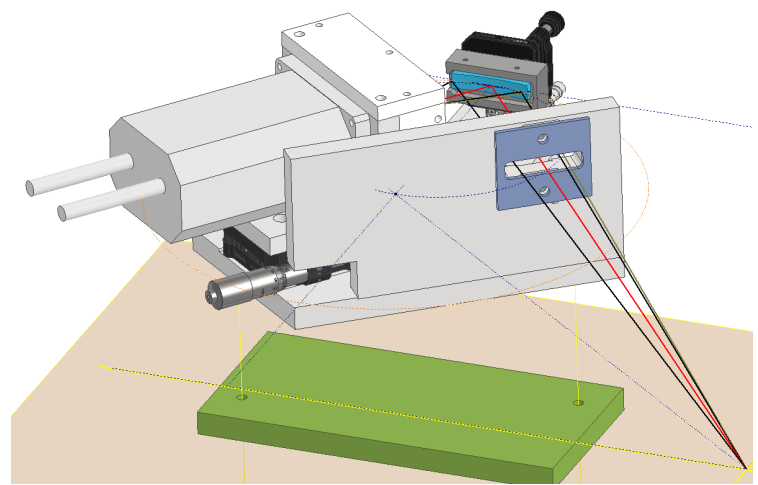
The precision of the internal alignment of ± 0.5 mm is realized with a series of grooves, where each part attached to the main plate is set into a groove. The alignment process use the various optical stages further guarantees the desired precision.

Table 5.2.: Color code of the FSSR-1D model with the functions and name of the parts. Note that there are four optical stages which are not color coded. These are used in the alignment process, so are labeled in fig. III.1.

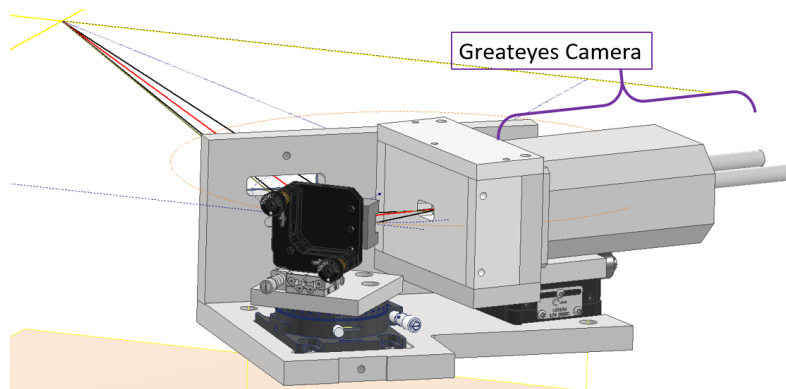
Color	Function	Name
Light gray	Structural/Shielding	-
Light gray (labeled)	Capturing spectra	Greateyes camera
Brown	Capturing spectra	Camera chip
White	Aperture at crossover/Shielding	Snout
Dark gray	Securing crystal	Crystal holder
Red (front of camera)	Holding carbon filter	Filter holder
Dark blue	Protecting crystal	Blast shield
Turquoise	Dispersion of rays	Mica crystal
Green	Support	Foot
Beige	Display location of chamber floor	Breadboard floor
Red	-	Central ray
Black	-	Outer rays
Olive green	-	Highest energy ray



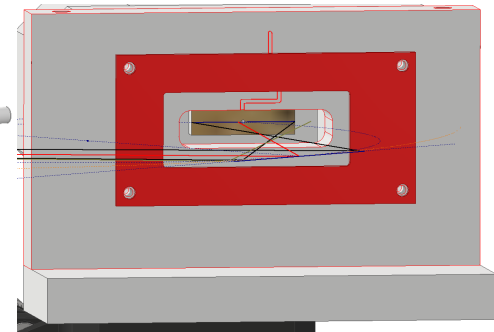
(a) Top view.



(b) Front view.



(c) Back view with Greateyes camera labeled.



(d) View onto chip with snout and camera apparatus hidden. Venting channel is shown behind the filter holder.

Figure 5.4.: CAD model of the FSSR-1D. The parts are color coded, whose function and name are listed in table 5.2. Note that the optical posts between foot and bottom plate are not shown. The various optical stages for aligning the spectrometer are shown, but not color coded.

6. Data Analysis

In this chapter, I will describe the analysis of the data collected in the laser-only experiment conducted in May 2023, with a focus on the spectrometers and their ability to produce spectra capable of high-resolution XAFS. In the following, I will start by explaining the processing of the raw images from the cameras into spectra, then I will outline the results to be derived from them.

I carry out the analysis with a program that I developed in *python3* called *AXAWOTLS*, which stands for "Analysis of X-ray Absorption for WDM Observation and Testing of Locally-made Spectrometers". It is capable of taking a TIFF image and outputting fully processed spectra, as well as performing further analysis with these spectra. The code is designed from the ground up to be applicable to any x-ray spectrometer intended for XAFS and allow "online" data analysis during a beamtime, producing results for any given event in less than a few minutes. With this processing speed and its ease-of-use, requiring only that the user input parameters, it is my hope that this code lets future researchers involved in WDM research with XAFS at PHELIX effectively interpret and act on raw data in a beamtime, simplifying the workflow.

The code consists of two main parts. The first is responsible for producing workable spectra from raw TIFF images, while the second encompasses further processing and application of these spectra for data analysis. The general workflow of the code to produce a spectrum is illustrated in fig. 6.1. First, horizontal line outs of each spectrum in the TIFF image are taken by selecting the corresponding area in the image and averaging over the pixels in the vertical direction. This yields the counts for each pixel, which are numbered starting from the leftmost edge of the image. Next, spectra are flipped depending on the orientation of the camera chip and spectrometer channels. The background spectrum is subtracted and the pixel number is converted to photon energy according to the dispersion of the spectrometer. To note is that this dispersion must be first calibrated by a previous known emission line, in this work the Al He- α line.

At this point the second part of the code, the data analysis, takes over, further processing the spectra as follows. First, the filters are corrected out using the transmission values from the CXRO database of Berkeley Lab. Then, the corrected counts on the camera chip N_{counts} are converted to photon number on detector N_{det} with the formula

$$N_{det} = \frac{N_{counts} \cdot E_{hole}}{G \cdot E_{ph} \cdot Qe}, \quad (6.1)$$

where the gain G , energy needed to generate a photoelectron E_{hole} , and quantum efficiency Qe are all properties of the x-ray camera found in its specification sheet. Next, the number of photons emitted by the source per steradian and energy interval $N_{st,eV}$ is estimated with the equation

$$N_{st,eV} = \frac{N_{total}}{4\pi\Delta E} = \frac{N_{det} \cdot D}{\Delta x_{pix} \cdot R_{int} \cdot \Delta E}, \quad (6.2)$$

adapted from Döppner *et al.* [44], where N_{total} represents the total number of photons emitted by the source, D the distance over which the x-rays diverge (for example, the optical path length from source to detector for flat crystal geometries), Δx_{pix} the pixel width in the non-dispersive direction (i.e. the physical

length which collects the rays), and ΔE the energy interval covered by a pixel. Notably, ΔE is assumed to be constant, as the dispersion of the spectrometers is approximately linear, and the integrated reflectivity R_{int} is taken from the literature, as it is not directly measurable in this experiment. Finally, the spectra can be smoothed through binning.

It is also important to note that the processing is slightly different for the FSSR, where it is summed instead of averaged over the pixel rows of the spectrum to get a horizontal line out. This is due to the focusing nature of the geometry, which can be most easily visualized with the pinhole analogy illustrated in fig. 3.3b. Any rays of a shared wavelength that land on a specific place on the detector in the dispersive plane must also pass through a unique mirrored location on the Rowland circle, such that one must sum the contributions in the non-dispersive direction to accurately represent the signal. As a consequence of the summing, the background is estimated by averaging to get a horizontal line out, then multiplying by the number of pixel rows summed over for the signal spectrum. As the photons are collected by the entire width of the mica crystal, the diverging distance D and the collecting length Δx_{pix} in formula 6.2 must be adjusted so that $\Delta x_{pix} \rightarrow w_{crystal}$, where $w_{crystal}$ represents the crystal width, and D becomes the source-crystal distance a_0 . Otherwise, the spectrum extraction is analogous to the flat crystal geometries.

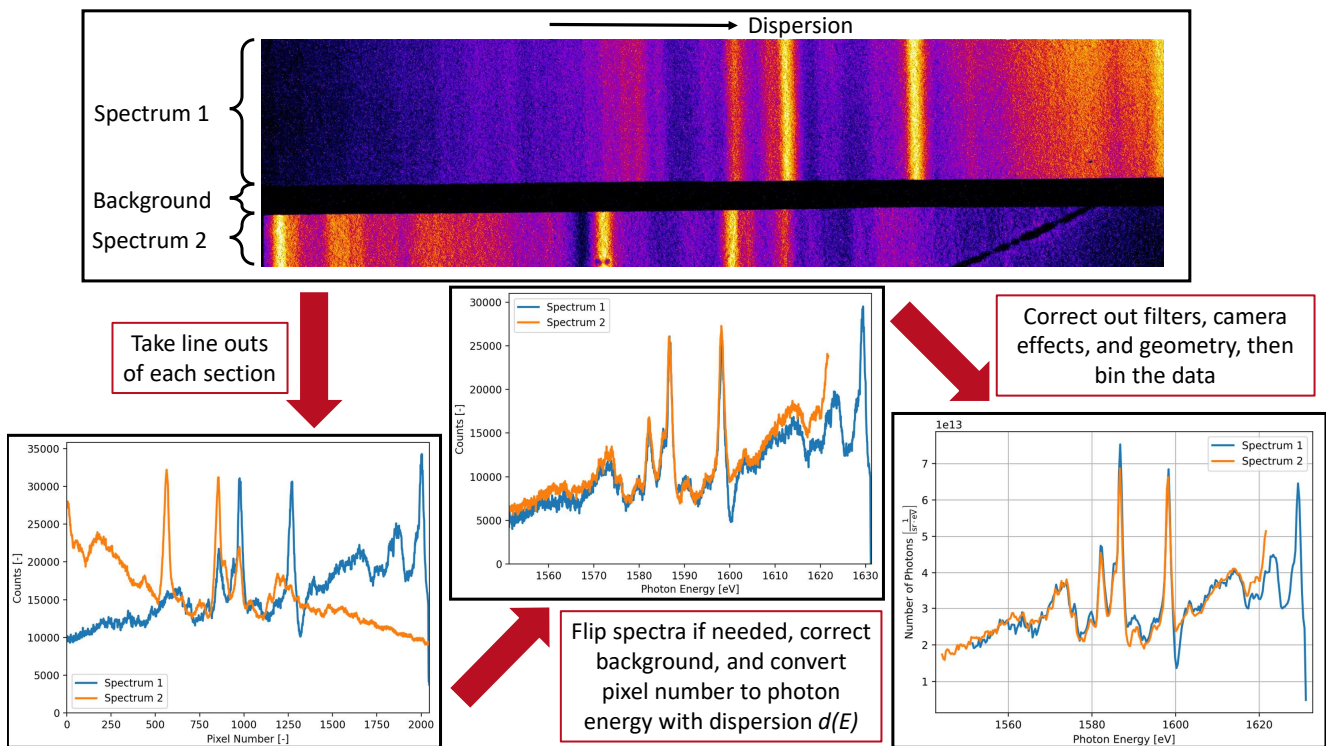


Figure 6.1.: Overview of the data analysis steps from raw TIFF image to fully processed spectrum. Example is of spectra from a Dy plasma ignited with a 57.3 J laser pulse, recorded with the DUCC. In the raw image, the higher the count, the warmer the color, so yellow represents the maxima and dark purple towards black the minima.

The fully processed spectra can then be used for further analysis, which aims to characterize the spectrometers and assess their performance in the scope of XAFS of aluminum. For clarity, I will organize the results into three categories, to be presented in the following chapter:

- 1. Qualitative Performance:** The results in this category serve to assess the spectrometers qualitatively

and to touch on the properties of the laser-driven backlights. The fundamental outputs of the spectrometer will be presented, which take the form of source spectra of various backlighter targets as well as absorption spectra of cold aluminum, where here cold refers to ambient vacuum temperatures.

2. **Spectrometer Characterization:** This covers the quantitative characterization of the spectrometers, consisting of the calculation of the spectral resolution through two spectral features: the He- α (corresponding to the $n=2$ to $n=1$ transition of He-like ions, starting from $2p^1P_1$) line of aluminum in source spectra and the Al K-edge in transmission spectra. Additionally, the ratio of integrated reflectivities of both spectrometers for a given event will be determined. To note is that the integrated reflectivity itself can not be directly determined, as the total emission of the x-ray sources are unknown.
3. **Setup Validation:** The purpose of this category is to check that the experimental setup yields plausible results considering the characteristics of the x-ray sources. To this end the conversion efficiency of the laser energy into the Al He- α emission line is determined, serving as a quantitative validation through comparison to literature.

In light of the results, the effectiveness of each spectrometer design in the context of this work will be discussed. I will then use these considerations to inform a recommended spectrometer design for future experiments.

7. Results and Discussion

In this chapter, I will present and discuss the results gained from spectra produced and analyzed by the in-house code *AXAWOTLS*. The results are grouped as described in the previous section, with each category addressing an aspect of the analysis. For each set of results, I will first explain the processing steps, then present the results, and end with a discussion detailing the ramifications for the spectrometer designs. For finer details of the calculations, please refer to the source code of *AXAWOTLS* at https://git.gsi.de/al_exafs/laser-only-wdm/-/tree/main/Codes. In addition, the error calculations will be described in the appendix chapter V.

I will begin with the qualitative performance, which will be prefaced by a brief introduction to the main types of emission of plasma, since it is important for the discussion of the source and absorption spectra. This will be followed by the spectrometer characterization, containing the spectral resolution and integrated reflectivity ratios of each spectrometer. Finally, I will present the setup validation, which consists of the conversion efficiency into the Al He- α line.

7.1. Qualitative Performance

As stated in the spectrometer comparison of section 4.3, neither the DUCC nor the FSSR-1D clearly distinguishes itself in terms of design specifications. As such, the qualitative assessment of the performance of each spectrometer during the experiment plays an important role. The most significant result in this area is of course the absorption spectra, whose quality depends on a number of experimental factors and mechanical properties, e.g. crystal quality, backlighter type, accuracy of the alignment of the setup, etc. To understand the details of the XAFS spectra quality, it is necessary to first study the spectra of the x-ray sources, i.e. the laser-driven plasma emission. Accordingly, I will begin by summarizing the main x-ray emission mechanisms in plasma, then present source spectra.

7.1.1. X-ray Source Spectra

There are three main mechanisms responsible for x-ray emission in plasma, each identifiable by their characteristics on the spectrum [1, 53]. The first is free-free emission, originating from scattering of free electrons with ions in the plasma. This generates bremsstrahlung and gives a smooth emission spectrum, where the intensity decreases for increasing photon energy. As this emission depends on average ionization, it is strongest for high Z materials. The second is recombination, in which free electrons recombine with ions and radiate a photon. This also results in a continuous spectrum, but deviates from bremsstrahlung emission in that it occurs from a minimum photon energy called the recombination edge. These edges also result in jumps in the spectrum corresponding to recombination stages. The third is line emission,

occurring for transitions of bound electrons between states. This is the strongest source of x-ray radiation, but is also discrete.

The types of x-ray emission lead to diverse possibilities for the source spectra of the different backscatterers. An ideal x-ray source for XAFS would exhibit a high-intensity, quasi-continuous spectrum, as this reduces the chance of spectral structure, like peaks or edges, impacting the absorption spectrum, as well as ensures good signal-to-noise ratios [1, 32]. In practice, continuum x-ray emission is usually realized by plasma of either very low-Z or high-Z (≥ 20) material. In the case of very low-Z targets, ions are fully stripped, thus suppressing line emission so that Bremsstrahlung dominates. For high-Z targets, the spectrum is dominated by line emissions from many-electron interactions, leading to a high line density and therefore a quasi-continuous spectrum. As such, very low-Z targets offer smooth spectra at the cost of having low intensity, while high-Z backscatterers yield high intensities with potential significant structure in the spectrum [53].

In light of this, five high-Z elements are tested in this experiment, namely gold and four rare earth elements: samarium, gadolinium, terbium, and dysprosium. Additionally, a low-Z material is investigated in the form of Teflon. Figure 7.1 depicts source spectra for each backscatterer material, which are all extracted and processed according to the procedure described in chapter 6. When available, events with different laser intensities are shown. All the source spectra, excepting those of Teflon, are captured with the DUCC, as it simultaneously displays the fewest spectral artefacts, often originating from crystal defects or damage, and good resolution, as will be demonstrated in section 7.2.1. Owing to the lower intensity of the emission as compared to the high-Z elements, the Teflon source spectra are taken with the SUCC, whose KAP crystal reflects significantly more x-rays than the DUCC's ADP crystals due to its higher integrated reflectivity. The greater collection rate of the SUCC is demonstrated in fig. 7.2a, where approximately three times more photons land on the detector (filter corrected) as compared to the DUCC.

In general, the spectrometers successfully produce results qualitatively in agreement with the expected source spectra. Each rare earth spectrum is dominated by high density line emission, recognizable in the peak-heavy structures, whereas the teflon spectrum exhibits a continuous spectrum whose intensity falls with increasing photon energy, as is consistent with bremsstrahlung emission. **QUESTION: IS THE Au SPECTRUM CONSISTENT WITH EXPECTATIONS? I THOUGHT ITS BREMSSTRAHLUNG, BUT THE INTENSITY DOESNT FALL WITH PHOTON ENERGY.** In addition, estimations of the conversion efficiency CE of laser energy E_{laser} into x-ray emission within the spectrometer energy range ($E_{max} - E_{min}$) deliver reasonable orders of magnitude in reference to FLYCHK simulations conducted by Leonard Weger. The estimation is carried out using the equation with the mean photon energy \bar{E}

$$CE = \frac{N_{st,eV} \cdot 4\pi(E_{max} - E_{min}) \cdot \bar{E}}{E_{laser}}, \quad (7.1)$$

yielding approximately a CE of 10% for dysprosium and 1% for teflon. While not a rigorous calculation, it serves as a first qualitative validation of the spectrum processing procedure and the efficacy of the spectrometers.

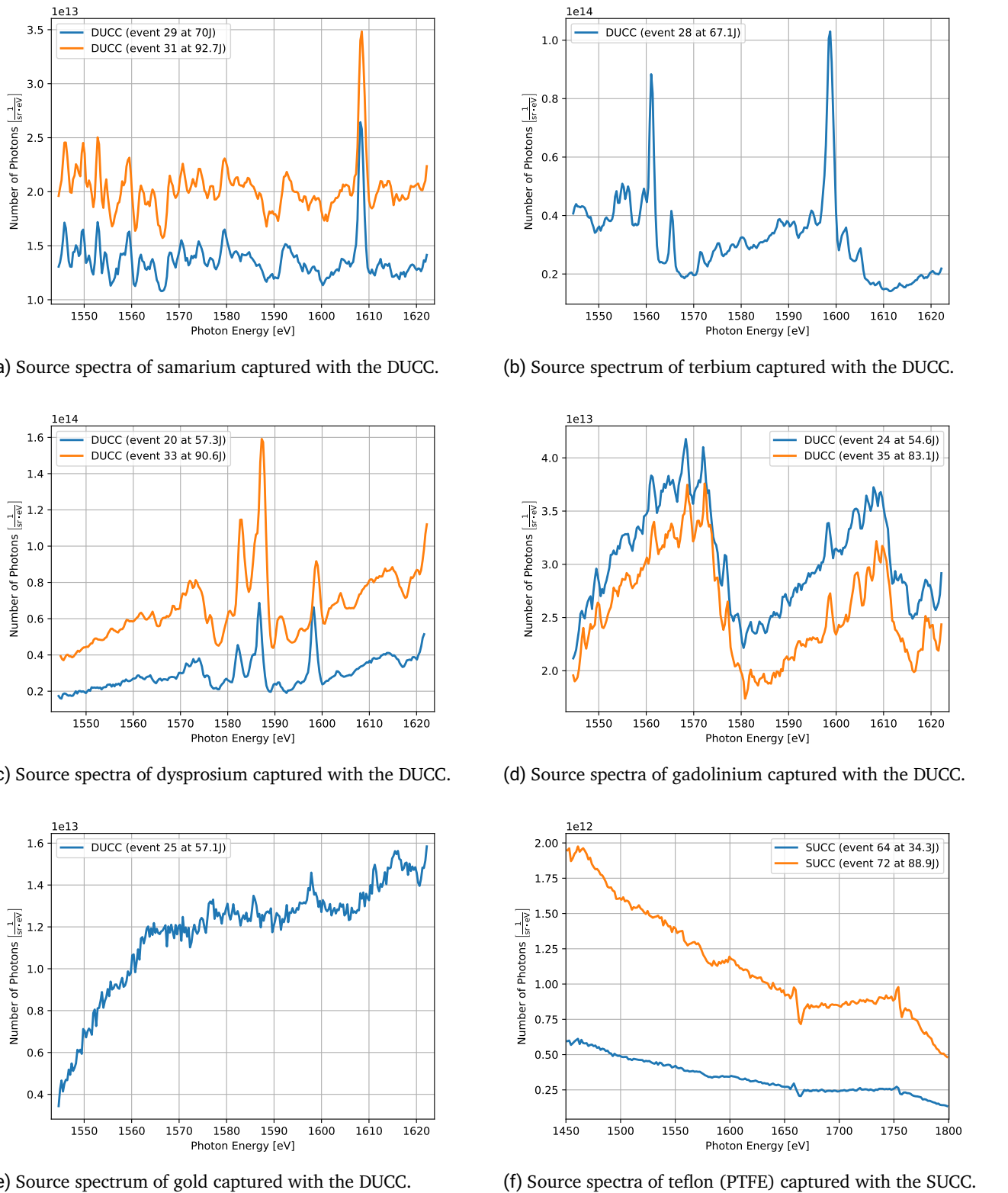
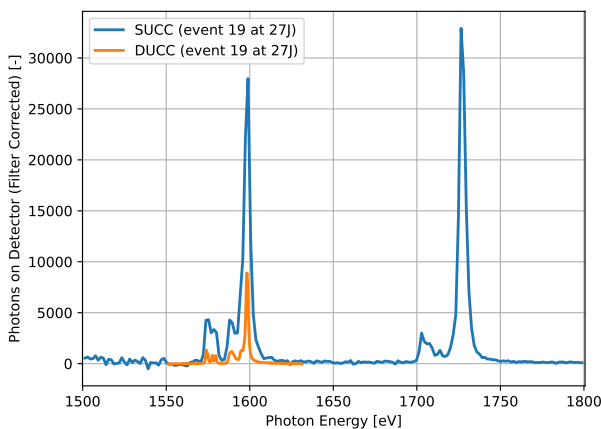
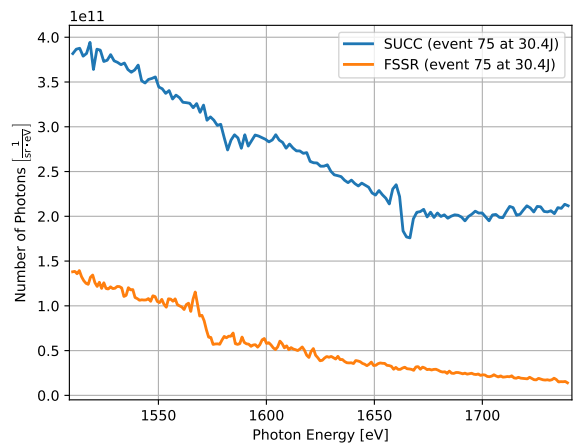


Figure 7.1.: Source spectra of laser-driven plasma from various backscatterer materials. Shots of different laser energies are shown when available. Notably, the teflon spectra are from the SUCC because the signal-to-noise ratio for the DUCC is in this case poor, as the intensity of the emission is at least an order of magnitude lower than for other backscatterers.

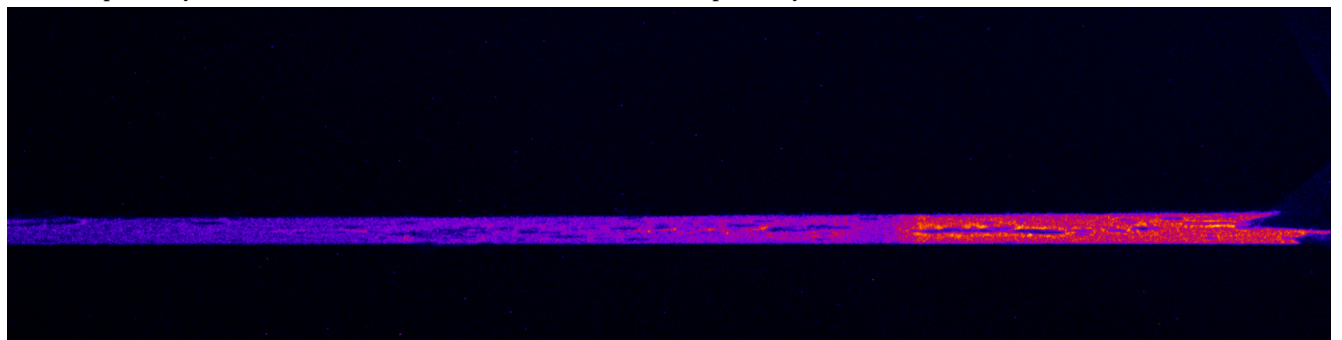
Notably, the FSSR is not represented in the example source spectra. As is apparent from fig. 7.2b, the FSSR spectra are laden with features that are most likely caused by defects and properties of the spherically bent mica crystal, significantly distorting the source spectrum. For example, a dip occurs for the FSSR at ≈ 1570 eV, preceded by a small peak at ≈ 1565 eV. These artefacts are likely caused by a K-edge from the aluminum component in the mica and by holes and features in the raw image (see fig. 7.2c) that can be traced back to defects in the crystal. Besides the difficulties of the crystal quality, the FSSR performed qualitatively as designed in that the predicted focusing properties were successfully reproduced and that spectra with the expected dispersion were extracted.



(a) Source spectrum of aluminum captured with the DUCC and SUCC respectively.



(b) Source spectrum of teflon captured with the FSSR and SUCC respectively.



(c) Raw TIFF image from the FSSR (unfocused) for a shot on teflon at 30.4 J (event 75).

Figure 7.2.: Supplementary results. (a) depicts the aluminum source spectra with the number of photons landing on the detector (ccd chip). This serves to illustrate the significantly greater collection efficiency of the SUCC, which can be traced back, in part, to the higher integrated reflectivity of the KAP crystal compared to the ADP of the DUCC. (b) shows the difference in spectra from a single shot on teflon for different spectrometers. From this one can identify spectral features that most likely are linked to crystal defects. The most notable is the dip at ≈ 1570 eV in the spectrum from the FSSR, an artefact of the Al K-edge originating from the presence of aluminum in the mica crystal makeup. (c) shows the numerous holes and deformations in the raw image of the FSSR, which are due to crystal defects and damage. To note is that for a standard FSSR-1D setup, the signal would appear as a single horizontal line. In this case, the image was unfocused by extending the crystal-detector distance b_0 by 5 mm.

7.1.2. X-ray Absorption Spectra

The processing of the x-ray absorption spectra begins with the extraction of the spectra for a given absorption shot analogously to the previous section, yielding a source and transmitted spectrum from the same x-ray source. The two spectra are then aligned with an algorithm that shifts the source spectrum until the best possible alignment is found in given energy range; a step made necessary by small deviations of the backlighter location from the TCC. Once aligned, the photon energy dependent transmission $T(E)$ is calculated by the ratio of the transmitted intensity I_{trans} to the source spectrum intensity I_{source} . The absorption coefficient μ can then be determined with the equation

$$\mu = \frac{-\ln(T)}{d_{Al,eff}}, \quad (7.2)$$

where the effective aluminum thickness $d_{Al,eff}$ takes into account the angle of the x-rays to the sample surface and with the thickness of the aluminum sample d_{Al} and central Bragg angle θ_0 is given by

$$d_{Al,eff} = \frac{d_{Al}}{\cos(\theta_0)}. \quad (7.3)$$

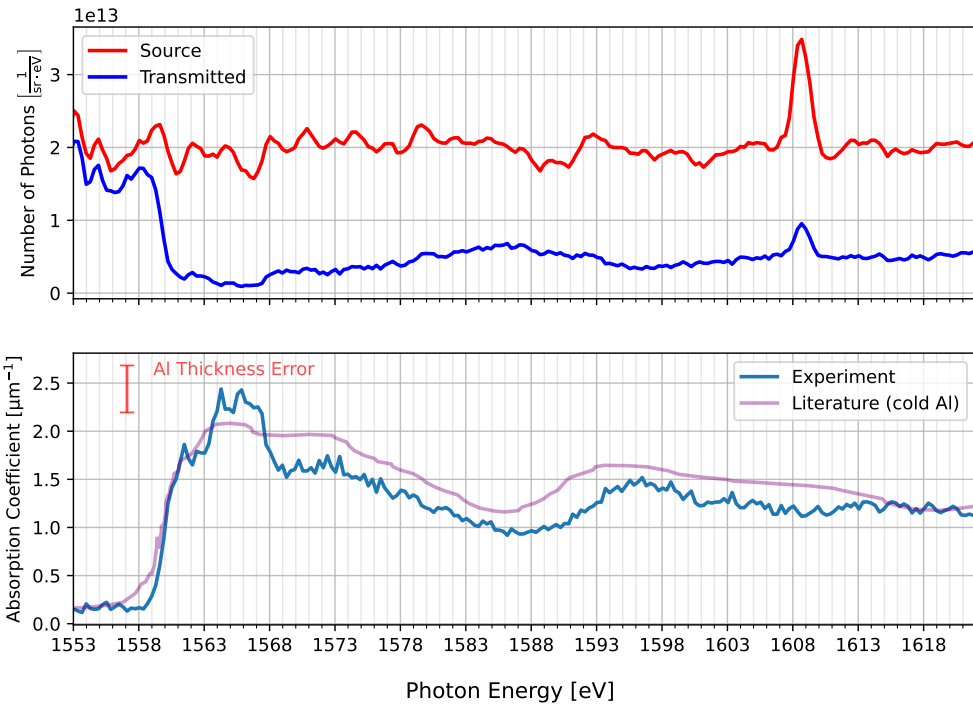
I estimated an error of 10% for d_{Al} , which gets passed onto the absorption coefficient using Gaussian error propagation. This uncertainty is depicted in the results as an error bar that aligns with the maximum value of μ .

While this procedure is effective for crystals of excellent quality, the processing can be improved by including a crystal calibration step. This step consists of using a so-called calibration shot, in which spectra without a sample are taken with ideally the same setup and laser parameters as the absorption shot, in order to account for spectral features from crystal defects. First, the features are isolated by dividing the calibration source spectrum corresponding to the source spectrum of the absorption shot $I_{cal,source}$ by the spectrum corresponding to the transmitted of the absorption shot $I_{cal,trans}$. For example, if the transmitted spectrum is captured with the OSUCC and the source with the SUCC, then for the calibration shot $I_{cal,trans}$ would come from the OSUCC and $I_{cal,source}$ from the SUCC. Using this ratio, the crystal features can be accounted for with the formula

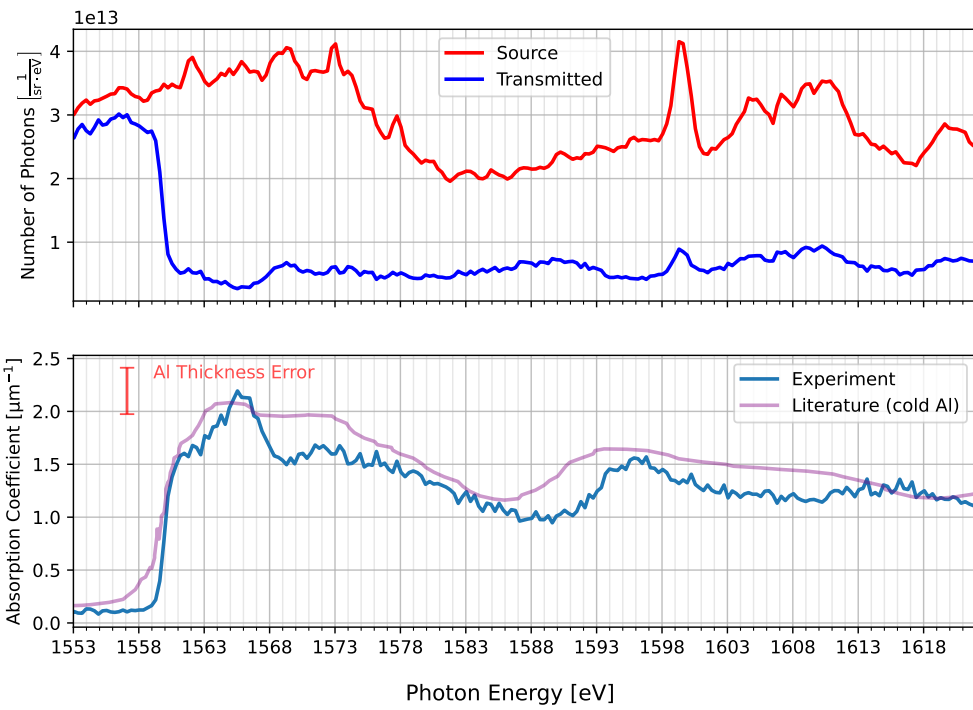
$$T = \frac{(I_{trans}/I_{source})}{(I_{cal,trans}/I_{cal,source})}. \quad (7.4)$$

To note is that calibrating in this way introduces further complexity to the processing and hinges on how accurately the shots are reproduced. Accordingly, I chose to apply this crystal calibration to the OSUCC/SUCC absorption shot, since the spectrometers are not identical and the crystals were of differing quality. The shots with the DUCC did not apply this calibration as no suitable calibration shots exist and the ADP crystals were of relatively good quality, in that they display few noticeable crystal spectral features.

For all the results presented below, the Al sample was placed directly on the spectrometer channel entrance to ensure that the Al foil remained at ambient temperature, i.e. so that no preheating due to proximity to the backlighter occurs. A literature curve of the Al absorption spectrum is used to validate the experimental results and is published by Levy *et al.* [27], whose experimental setup is similar to our own with the DUCC, with the key differences that the rare earth erbium is the backlighter material and the crystals are conically bent.



(a) X-ray absorption spectrum through a $(1.18 \pm 0.12) \mu\text{m}$ thick aluminum foil for a 97.4J shot on samarium.



(b) X-ray absorption spectrum through a $(1.18 \pm 0.12) \mu\text{m}$ thick aluminum foil for a 87.4J shot on gadolinium.

Figure 7.3.: X-ray absorption spectra taken using the DUCC. In (a) and (b); Above: fully processed spectrum pair whose ratio yields the x-ray transmission through the sample. **Below:** absorption spectrum with comparison to a result from Levy *et al.* [27] and the systematic uncertainty due to the sample thickness.

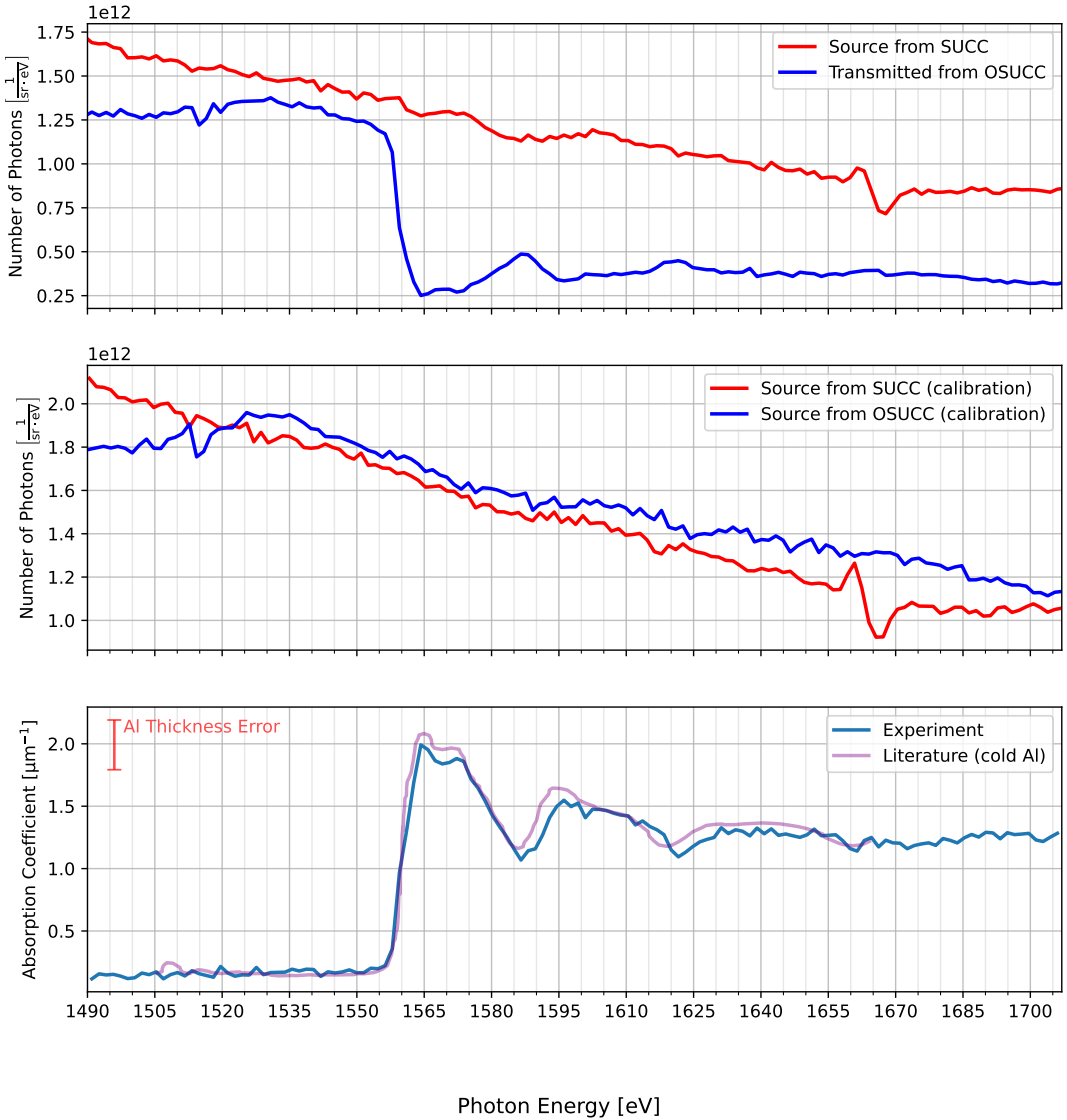


Figure 7.4.: X-ray absorption spectrum taken using the SUCC for the source and the OSUCC for the transmitted spectrum. The crystal spectral features are corrected out using a calibration shot without a sample. **Above:** fully processed spectrum pair from a 88.9 J shot on teflon. The ratio of transmitted to source spectrum yields the x-ray transmission through a $(0.84 \pm 0.08) \mu\text{m}$ thick aluminum foil sample. **Middle:** fully processed calibration spectrum pair from a 110.3 J shot on teflon. **Below:** absorption spectrum with comparison to a result from Levy *et al.* [27] and the systematic uncertainty due to the sample thickness.

In the case of the absorption shots with the DUCC (see fig. 7.3), for which the dual channels are employed to record the spectra, a reasonably good agreement with the literature curve is achieved, considering that no crystal calibration is carried out. Notably, the extraction of absorption spectra of this quality required careful fine tuning of the alignment algorithm; a consequence of the structure-heavy transmitted and source spectra. In fact, much of the structure in the absorption spectra can be attributed to features of the x-ray

source emission. In general, a peak in the source spectrum will yield a dip in the absorption, and vice-versa. For example, many structures occur in the range of 1561-1568 eV that are clearly artefacts from the source spectrum, a observation supported by the marked difference of the absorption curve in that range between fig. 7.3a and fig. 7.3b. The two shots also differ from the literature example in the magnitude of the absorption coefficient, with the experimental curve being on average lower. The deviation being within the error due to the Al sample thickness could explain the difference, as well as the potential influence of the erbium backlighter spectral structures on the literature curve. Despite the differences between shots, the similarity of the overall behavior of the experimental absorption spectra, especially in the oscillation after 1570 eV, implies qualitative consistency between shots, lending validity to the experimental setup and dual channel spectrometer design.

In contrast to the DUCC, the absorption spectrum pictured in fig. 7.4 is extracted using two separate single channel spectrometers, namely the SUCC and OSUCC, and a teflon backlighter, which displays an exceptionally smooth x-ray source spectrum. Interestingly, the resulting absorption curve shows excellent agreement with the literature, despite the fact that the KAP crystal of the OSUCC was of visibly low quality and that the spectral resolutions are by nature of the spectrometer geometries different. I attribute the effectiveness of the setup to three considerations. First, the crystal features in the recorded spectra are for the most part corrected out by the crystal calibration, as apparent in the disappearance of the peak and valley inherent in both the calibration and source spectrum of the SUCC. Second, the smoothness of the teflon spectra suppresses the difference of spectral resolutions, while reducing overall foreign structure in the absorption curve. Third, the OSUCC crystal is most significantly damaged on the low end of the spectrum, visible in the calibration spectrum of the OSUCC, with the higher energies showing few large features. That the most significant defects appear behind the K-edge energy means that the poor crystal quality plays only a minor role in XAFS. The resulting quality of the experimental absorption spectrum demonstrates the power of a smooth backlighter spectrum as well as the crystal calibration method.

As the reader may note, the FSSR is not represented here. Despite many attempts at tuning the alignment algorithm and selecting a suitable combination of absorption and calibration shots, the absorption spectra derived from the FSSR/KAP setup yielded no curves that clearly aligned with that of aluminum. The main reasons are twofold. On one hand, the poor quality of the mica crystal and presence of Al in the chemical makeup lead to significant spectral structure around the K-edge energy, heavily distorting the absorption curve, especially at the edge. On the other, the vastly different geometries and function of the FSSR and SUCC hindered the aligning of the component spectra and prevented the removal of spectral structures in the absorption curve, which is most noticeable at large peaks in the backlighter emission. The difference in spectral resolution has the largest impact in this regard. This result again highlights the utility of a smooth backlighter spectrum. It also reflects the importance of good crystal quality, even with a meaningful tool like the crystal calibration.

In summary, the results of this section expose the difficulties brought on by highly-structured x-ray source spectra and using different spectrometers in a setup, as well as the impact of poor crystal quality on the end results. In light of these findings, the geometry of the DUCC, with its dual channels and flat crystals, represent the most promising design, since it offers the highest potential for good crystal quality and guarantee of near identical spectral resolutions and geometries. In addition, it is clear that a smooth backlighter spectrum greatly simplifies the processing of the data and leads to a smooth absorption curve, although the use of a specific backlighter material still hinges on the its interaction with the spectrometer itself. This is seen in the combination of a teflon backlighter with the DUCC spectrometer, where the poor signal-to-noise ratio makes it untenable, though it is sound in theory.

7.2. Spectrometer Characterization

To supplement the qualitative analysis of the spectrometer performance, properties of three spectrometers, namely the DUCC, FSSR, and SUCC, will be quantitatively investigated, giving insight into the extent to which the designs were successfully implemented. First, the spectral resolution and its contributions will be determined for all the spectrometers using the He- α line of aluminum, along with the transmission for absorption shots of the DUCC. From these results, I will assess the efficacy of the *mmpxrt* simulations and the viability of each spectrometer for its intended type of XAFS. Second, I will calculate the ratio of the integrated reflectivities of the crystals for each spectrometer pairing, as well as directly estimate the R_{int} value of the mica crystal in the FSSR with the help of a simulation carried out by Artem Martynenko, allowing further characterization of the crystals and assessment of their impact on the spectrometers' performance.

7.2.1. Spectral Resolution

The analysis of the spectral resolution begins with the extraction of spectra, following the same method as before except for the binning of the data, which is left out to maximize the number of data points. In the case of the calculations using the He- α line, the peak at 1598.4 eV in aluminum source spectra is first isolated. Due to the influence of a neighboring small emission line (see fig. 7.2a), the bottom part of the lower energy side of the peak is cut off at approximately the full width at half maximum (FWHM). The empty region is then replaced by mirroring the higher energy side of the line, taking only the values below the FWHM. Consequently, a near symmetrical, approximately Gaussian peak remains. The data points are then fitted to a Gauss function of the form

$$f(x) = A \cdot \exp\left(\frac{-(x - \mu)^2}{2\sigma^2}\right) + c \quad (7.5)$$

with the fit parameters A , μ , σ , and c . The goal is to determine the FWHM through the equation

$$\text{FWHM} = 2\sqrt{2\ln(2)} \cdot \sigma, \quad (7.6)$$

corresponding to the convolution of a number of line broadening mechanisms. For this application the significant contributions are Doppler broadening and spectrometer resolution, which consists of source broadening, detector resolution, and broadening due to crystal properties, henceforth referred to as crystal broadening. For clarity I'd like to note that crystal broadening is affected by geometry as well as crystal quality. By deconvolving the FWHM result with

$$\sigma_{crystal} = \sqrt{\text{FWHM}^2 - \sum_i^n \sigma_i^2}, \quad (7.7)$$

where the sum over σ_i represents the resolution contributions listed above, the crystal broadening $\sigma_{crystal}$ is calculated. By comparing $\sigma_{crystal}$ to the results of the *mmpxrt* simulations, I will assess the spectrometer performance and quality of the crystals.

In the case of the DUCC, the resolution can also be found using the transmission T for absorption shots. This method leverages the dual channel aspect of the geometry and the absence of significant crystal features in the spectra and works under the assumption that the resolutions of both channels are equal. For the

analysis I first extract the transmission spectrum analogously to the method described in section 7.1.2. Next, I fit the data with the modified error function

$$f(x) = A \cdot \text{erf} \left(\frac{-(x - \mu)}{(\sigma\sqrt{2})} \right) + c \quad \text{with} \quad \text{erf}(z) = \frac{2}{\sqrt{\pi}} \int_0^z e^{-t^2} dt, \quad (7.8)$$

yielding the same fit parameters as with the Gauss function. Finally, σ_{crystal} can be determined just as with the He- α line, except without the Doppler broadening contribution.

In order to have full insight into the FWHM uncertainty calculation, I conduct the fitting with a self-built algorithm that manually tests a range of possible FWHM values. The algorithm functions as follows:

1. Initialize a set of evenly spaced FWHM values ranging from 0.5-7 eV.
2. Loop through the FWHM set, where for each value a model is created by fitting the data while holding the fit parameter σ constant as calculated from the FWHM.
3. The "goodness" of each model is parameterized using the reduced chi-squared test, which determines a χ^2 value with the formula

$$\chi^2 = \frac{1}{n - m} \sum_i^n \frac{(O_i - M_i)^2}{s_i^2}, \quad (7.9)$$

where O_i is the observed data point, M_i the corresponding fitted value, s_i the statistical error of the data point, n the number of data points, and m the number of fit parameters.

4. With this test, models are generally accepted if $\chi^2 \leq 1$. As the statistical error of the data in this experiment is too small to yield a low enough χ^2 , a model is considered acceptable if $\chi^2 \leq 1.5 \cdot \chi_{\min}^2$, where χ_{\min}^2 is defined as the minimum value of all the fit models. I chose the prefactor 1.5 heuristically by testing the fits and gradually reducing the prefactor until the fringe models were visually reasonable.
5. The final FWHM is chosen from the best model, i.e. with χ_{\min}^2 . The bounds of the error are given by the absolute difference between the best FWHM and the worst accepted FWHM, so with the largest χ^2 within the accepted range.

For each result I will graph the best fit alongside the upper and lower worst accepted fits, with the corresponding χ^2 values.

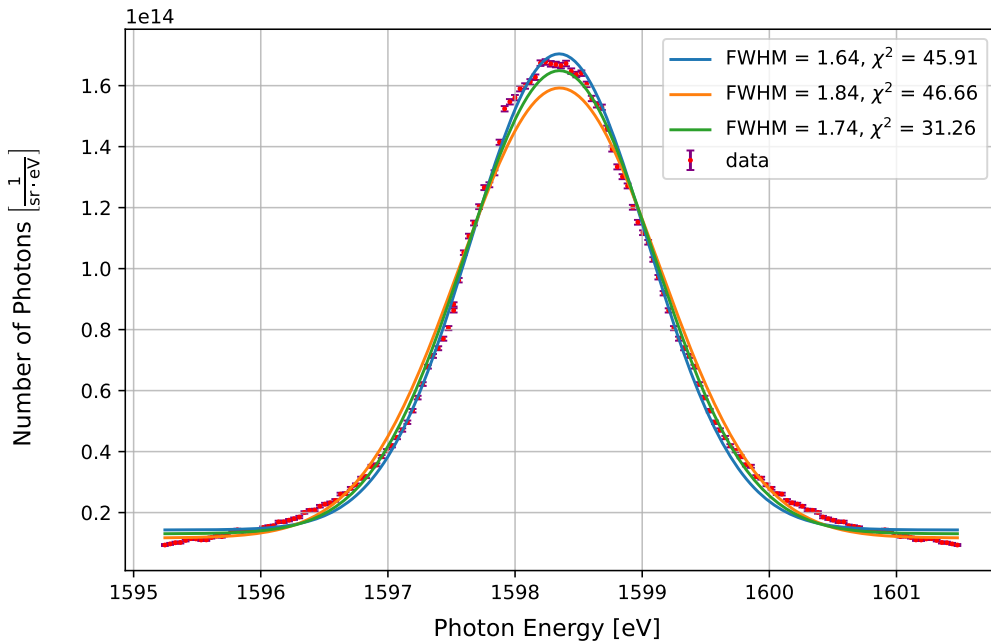
For the SUCC and DUCC the source broadening plays a crucial role. It is derived from the source size and is influenced by the spectrometer geometry. To determine the source size, we placed a so-called knife edge on the SUCC, consisting of a opaque metal sheet placed in front of the crystal in the x-ray path in such a way as to cover approximately half of the source image on the detector. By fitting an error function to the edge of the shadow cast by the knife edge, the number of pixels that the FWHM covers can be extracted and converted to millimeter with the pixel size. Lastly, the magnification of the knife edge image, set by the geometry and knife edge placement, is accounted for, yielding the source size. I then begin calculating the source broadening by projecting the source size x_s onto the detector of a given spectrometer with the formula

$$x_{s,d} = \frac{x_s}{\cos(\theta_0)}. \quad (7.10)$$

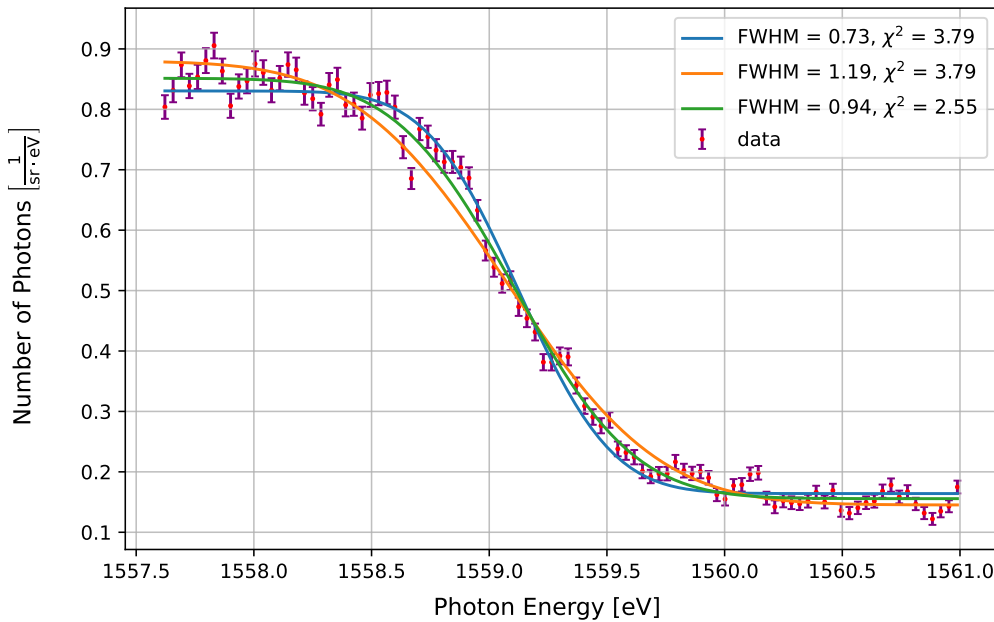
The source image size $x_{s,d}$ is converted to eV using the dispersion of the spectrometer, finally resulting in the source broadening.

In the following I present the results for the spectral resolution calculations. An example graph for each spectrometer and type of fit is accompanied by tables containing the results for each resolution contribution.

The final results for the crystal broadening as compared to the *mmpxrt* simulations are then given. The graphs of the remaining shots not shown below can be found in the appendix section IV.i.



(a) Gaussian fit of the He- α peak for a 27 J shot on aluminum (event 19).



(b) Error function fit of the transmission through a (1.18 ± 0.12) mm thick aluminum sample for a 87.4 J shot on gadolinium (event 32).

Figure 7.5.: Fits used to determine the spectral resolution of the DUCC with (a) Gaussian fit and (b) error function fit respectively. The best (green) and worst (blue and orange) fit models are depicted and labeled with their corresponding FWHM and χ^2 values.

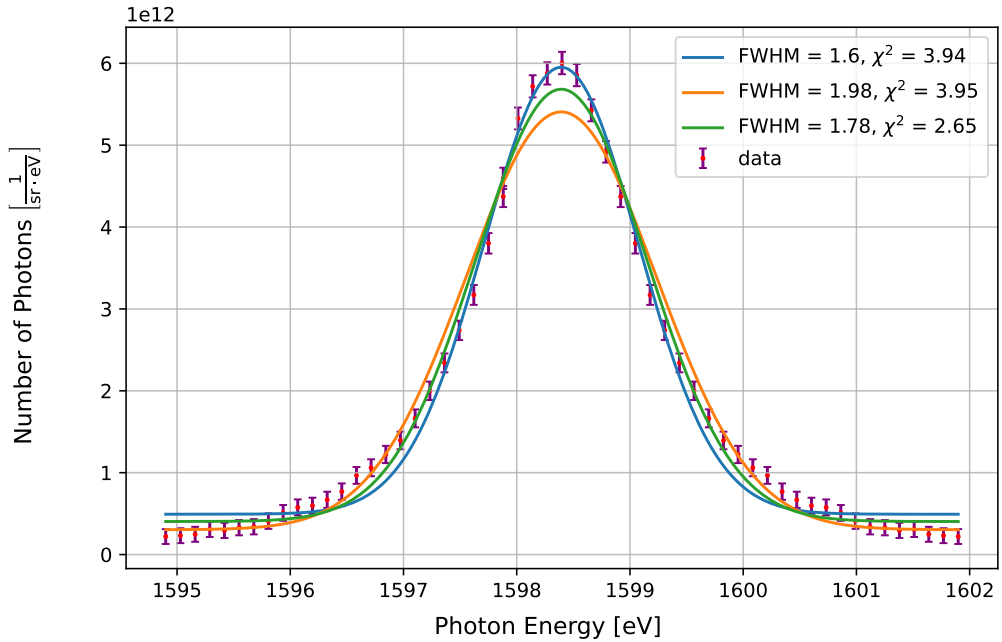


Figure 7.6.: Gaussian fit of the He- α peak for a 24 J shot on aluminum (event 16) used to determine the spectral resolution of the FSSR. The best (green) and worst (blue and orange) fit models are depicted and labeled with their corresponding FWHM and χ^2 values.

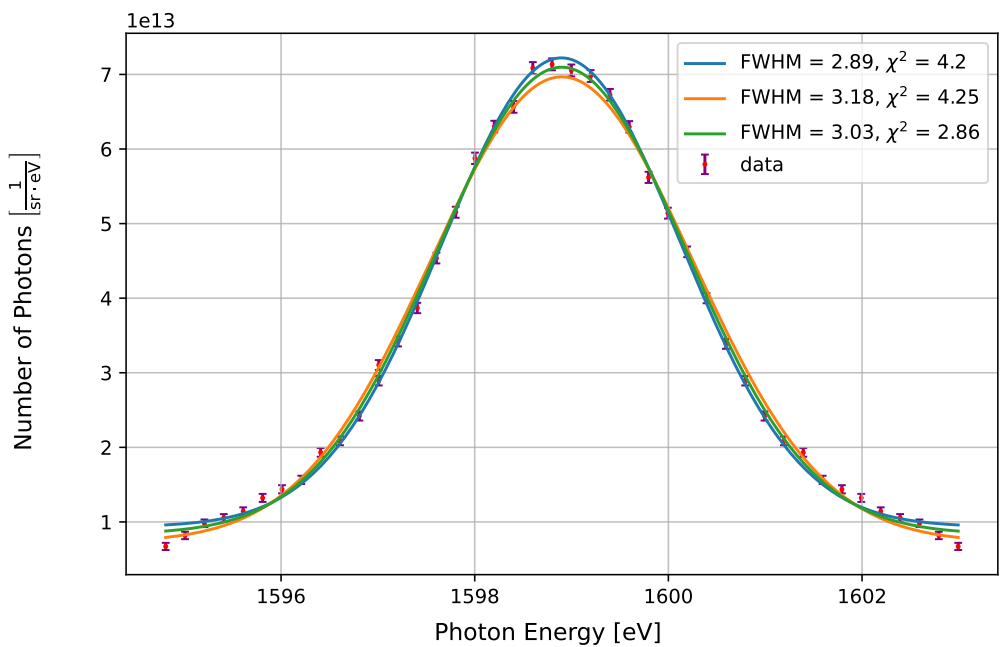


Figure 7.7.: Gaussian fit of the He- α peak for a 28 J shot on aluminum (event 18) used to determine the spectral resolution of the SUCC. The best (green) and worst (blue and orange) fit models are depicted and labeled with their corresponding FWHM and χ^2 values.

Table 7.1.: Resolution contributions of DUCC, where every value is given in eV unless another unit is expressly assigned. The shot parameters and type of calculation are presented, where g corresponds to a Gaussian fit of the Al He- α peak and t to an error function fit of the transmission. The fit algorithm discussed previously delivers the FWHM and its error. Source size and broadening are determined from the knife edge of the SUCC. Doppler broadening is from a FLYCHK simulation with the electron temperature $T_e = 1000$ eV, whose error is estimated from comparison to a simulation of $T_e = 500$ eV. The crystal broadening results from the deconvolution of the FWHM. Notably, the detector resolution of the DUCC is negligible (see table 4.1).

Shot	Type	FWHM	Source Size [mm]	Source Broadening	Doppler Broadening	Crystal Broadening
27 J on Al	g	$1.739^{+0.105}_{-0.099}$	0.118 ± 0.015	0.491 ± 0.062	0.474 ± 0.100	$1.599^{+0.119}_{-0.113}$
92.7 J on Sm	t	$1.287^{+0.468}_{-0.319}$	0.147 ± 0.002	0.610 ± 0.009	-	$1.134^{+0.532}_{-0.363}$
87.4 J on Gd	t	$0.940^{+0.253}_{-0.209}$	0.137 ± 0.002	0.571 ± 0.008	-	$0.748^{+0.319}_{-0.263}$

Table 7.2.: Resolution contributions of FSSR, where every value is given in eV unless another unit is expressly assigned.. Each column is derived analogously to table 7.1. In this case, the source broadening is negligible due to the focusing properties of the FSSR, but the detector resolution becomes significant (see table 4.1). The detector resolution uncertainty is neglected, as it is small compared to other error sources because of the precisely known pixel size.

Shot	Type	FWHM	Detector Resolution	Doppler Broadening	Crystal Broadening
1.7 J on Al	g	$1.799^{+0.193}_{-0.182}$	0.143	0.474 ± 0.100	$1.730^{+0.202}_{-0.190}$
24 J on Al	g	$1.777^{+0.198}_{-0.176}$	0.143	0.474 ± 0.100	$1.707^{+0.208}_{-0.185}$

Table 7.3.: Resolution contributions of SUCC, where every value is given in eV unless another unit is expressly assigned. Each column is derived analogously to table 7.1. The detector resolution is assumed to be negligible, following from the shared basic design of the SUCC and DUCC.

Shot	Type	FWHM	Source Size [mm]	Source Broadening	Doppler Broadening	Crystal Broadening
24 J on Al	g	$2.691^{+0.149}_{-0.138}$	0.075 ± 0.013	1.156 ± 0.201	0.474 ± 0.100	$2.384^{+0.195}_{-0.185}$
28 J on Al	g	$3.033^{+0.149}_{-0.138}$	0.109 ± 0.028	1.685 ± 0.438	0.474 ± 0.100	$2.477^{+0.349}_{-0.343}$
27 J on Al	g	$2.922^{+0.193}_{-0.176}$	0.109 ± 0.022	1.691 ± 0.3325	0.474 ± 0.100	$2.336^{+0.341}_{-0.327}$

Table 7.4.: The final results for the crystal broadening compared to simulation when applicable. The type corresponds to which feature was used to fit, g for Gaussian Al He- α peak and t for the transmission through an Al sample. The experimental broadening is calculated by the mean of the crystal broadening results of all available shots.

Spectrometer	Type	Simulated Broadening	Experimental Broadening
DUCC	g	0.238 eV	$(1.599^{+0.119}_{-0.113})$ eV
DUCC	t	0.238 eV	$(0.941^{+0.310}_{-0.224})$ eV
FSSR	g	2.954 eV	$(1.719^{+0.145}_{-0.133})$ eV
SUCC	g	-	$(2.399^{+0.175}_{-0.170})$ eV

Immediately apparent in table 7.4 is that the simulated crystal broadening values deviate significantly from the experimental. In both available cases, the main cause likely lies in the discrepancy of the R_{int} values used in the *mmxprt* simulation (28.9 μ rad for mica and 2.32 μ rad for ADP) to the real, unmeasured values. As will be elaborated on in the next section, the FSSR appears to exhibit a significantly lower integrated reflectivity than anticipated, while the results of the DUCC point to a markedly worse quality. This demonstrates the inherent difficulty in assuming accurate crystal properties purely from the literature, where values can easily deviate by an order of magnitude, e.g. with the ADP R_{int} values of 2.32 μ rad [47] and 40 μ rad [52]. Therefore, accurate resolutions from simulations clearly require sufficient pre-knowledge of the crystal, which in this work is unfortunately lacking.

Another interesting finding is the more than 50% deviation of the crystal broadenings found with the transmission and the He- α line for the DUCC, lying well outside the margins of error. In addition the two transmission results given in table 7.1, computed from shots on different rare-earth backscatterer materials, do not line up nor fall within the error ranges. Both these discrepancies could be attributed to inaccuracies introduced into the transmission spectrum by structure in the original rare-earth backscatterer spectra, which become significant in the small width of the Al K-edge (~ 1 eV), reinforcing the argument that smooth backscatterer spectra are highly advantageous for this application. Another possible origin of the crystal broadening discrepancy between the transmission and peak techniques is unaccounted for broadening mechanisms of the emission line, leading to an artificially inflated result for the He- α line. The most probable mechanism is stark broadening caused by interaction with charged particles in the plasma, which broadens lines according to a Lorentz distribution. Notably, Doppler broadening dominates for high electron temperature, low electron density plasma [54], as is expected for the Al plasma in this experiment. As such, any influence of the stark broadening should be small, making it an unlikely culprit of the crystal broadening discrepancy.

On the other hand, the stark broadening could help explain why the Gaussian fit of the He- α line does not perfectly fit the data, as most easily seen in fig. 7.6. The relatively far extending wings of the data are characteristic of the Lorentz profile [25] and indicate that the peak likely conforms to a Voigt profile, which is the convolution of the Gauss and Lorentz profile. Despite this, a Gaussian profile is applied for the fitting because it still closely describes the data and markedly simplifies the analysis, since the Voigt fitting would require an additional fitting parameter.

Due to its applicability to all spectrometers, the Gauss fit results will be used in a comparison of the FSSR, DUCC, and SUCC resolutions. With a crystal broadening of $(1.599^{+0.119}_{-0.113})$ eV, the DUCC with ADP

crystals does not fulfill the original spectrometer design consideration for conducting XANES of $\Delta E \leq 1$ eV, even without considering source broadening. This failing, along with the low x-ray collection efficiency that precludes using a teflon backlighter, excludes the future use of the DUCC in its current iteration. Conversely, the excellent spectral resolutions, as calculated by the deconvolution of the FWHM from the Doppler broadening, of $(1.724^{+0.145}_{-0.132})$ eV for the FSSR and $(2.842^{+0.097}_{-0.089})$ eV for the SUCC, easily fulfill the requirement of $\Delta E < 10$ eV for EXAFS. Consequently, both the spectrometers could be considered viable candidates for future designs, purely from a spectral resolution standpoint.

7.2.2. Integrated Reflectivity Ratio

To build on the findings of the previous section, the ratio of R_{int} will now be determined, giving a deeper insight into the quality of the KAP, ADP, and mica crystals. To calculate the ratio of the integrated reflectivities of the crystal of a pair of spectrometers for a shot, I begin by extracting the source spectra of an Al shot for two spectrometers, following the same process as described in chapter 6 but leaving out the binning and multiplying equation 6.2 with R_{int} , ΔE and 4π . Accordingly, the quantity of interest becomes

$$N_{total} \cdot R_{int} = \frac{4\pi \cdot N_{det} \cdot D}{\Delta x_{pix}}. \quad (7.11)$$

Then, I approximately integrate by summing over the $N_{total} \cdot R_{int}$ values for a given energy range, which I chose to cover the two emission lines at 1588.3 eV and 1598.4 eV, corresponding to the $n = 2 \rightarrow n = 1$ transition of heliumlike ions of aluminum [55]. These lines are selected because they are the strongest that fall within the shared energy range of every spectrometer. Next, by simply taking the ratio of $N_{total} \cdot R_{int}$ of both spectrometers, I can determine the integrated reflectivity ratio of the crystals. As previously noted, R_{int} cannot be directly measured by this setup due to the unknown total number of emitted photons from the source N_{total} .

In addition to the method above, the R_{int} for the mica crystal of the FSSR will be calculated directly by using the efficiency γ of the FSSR spectrometer with mica crystal, derived in a simulation conducted by Artem Martynenko using the parameters of the FSSR geometry of this work and mica crystals typical of Sergey Pikuz' lab, where the crystal of this experiment originates. The efficiency is defined as the ratio the simulated photons reaching the detector $N_{det,sim}$ and the total number of emitted photons, i.e. $N_{det,sim}/N_{total}$. I determine the integrated reflectivity of the FSSR by first linearly interpolating the efficiency data of fig. 7.8 to get $\gamma(E)$. Then, equation 7.11 is applied to derive

$$R_{int} = \frac{\sum_i [4\pi \cdot N_{det}(E_i) \cdot D(E_i)] / w_{crystal}}{\sum_j (N_{det}(E_j) / \gamma(E_j))}, \quad (7.12)$$

where the summations are over the same energy range described in the first method.

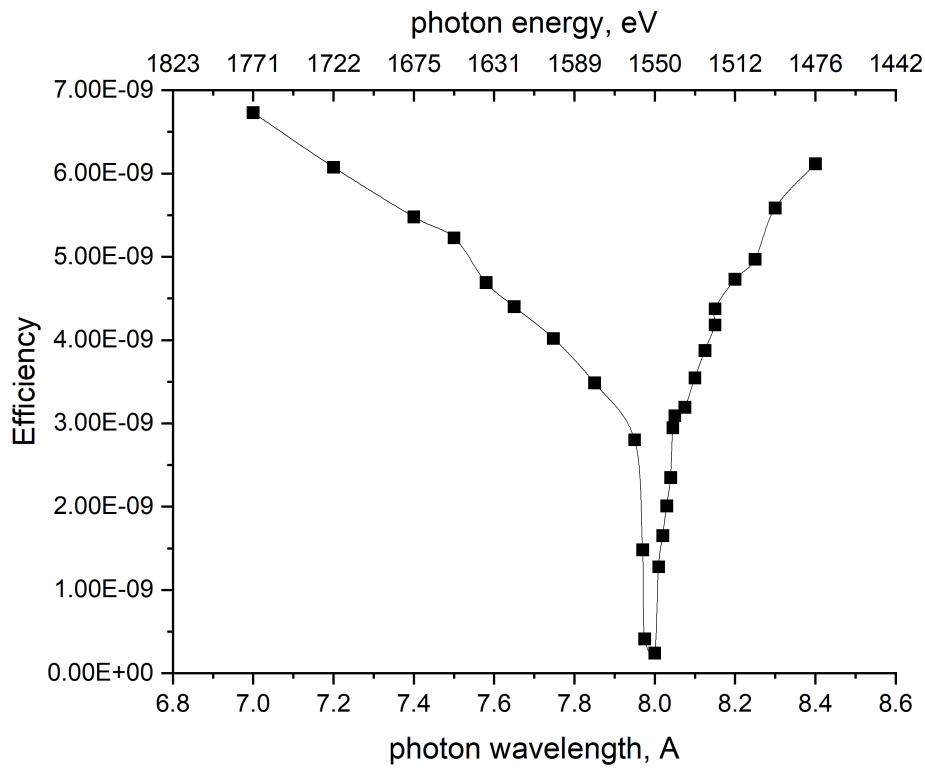


Figure 7.8.: Efficiency of the FSSR-1D with a mica crystal typical of Sergey Pikuz' lab, extracted by a ray tracing simulation carried out by Artem Martynenko. Immediately recognizable is a dip around 1540-1560 eV, which is related to the K-edge of the aluminum component of the mica crystal.

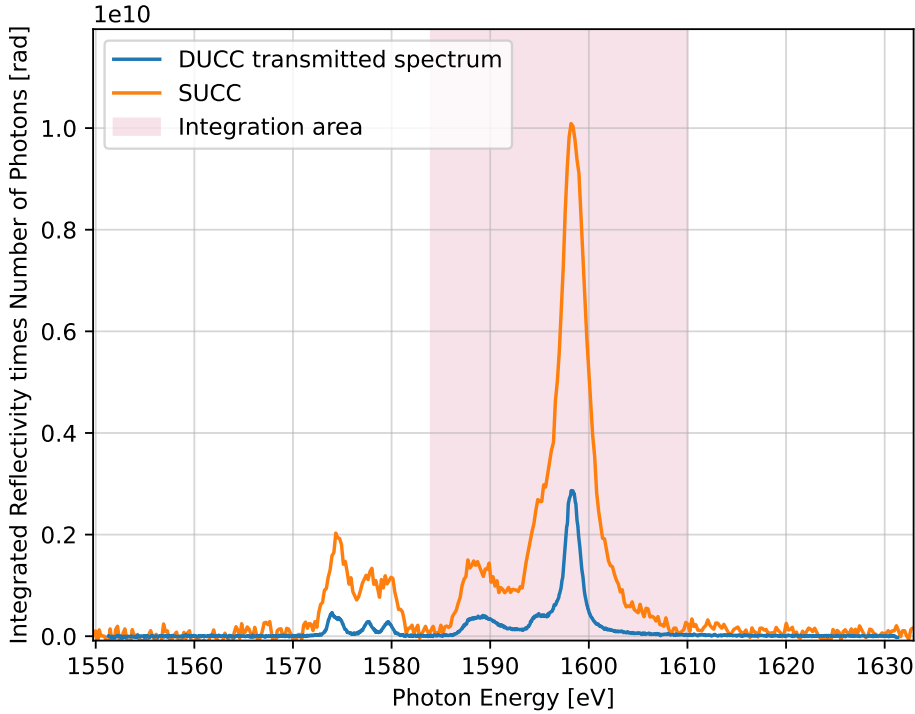


Figure 7.9.: $R_{int} \cdot N_{total}$ for a 27 J shot on aluminum (event 19). The spectra from the transmission channel of the DUCC and the SUCC are presented, as well as the integration area used to calculate the integrated reflectivity ratio.

The results will be compared to the estimated literature values for R_{int} of 40 μrad for the ADP crystals of the DUCC [52], 80 μrad for the KAP crystal of the SUCC [50], and 53.6 μrad for the mica crystal of the FSSR [38]. For clarity and completeness, $N_{total} \cdot R_{int}$ is depicted along with the integration area for the SUCC and the transmitted spectrum of the DUCC (see fig. 7.9). The other cases are available in the appendix section IV.ii.

Table 7.5.: Ratio of R_{int} for various spectrometer combinations. DUCC_{*t*} refers to the transmission channel of the DUCC and DUCC_{*s*} to the source channel. The literature ratios are calculated using the literature values given above.

Shot	Spectrometer	Literature Ratio	Experimental Ratio
27 J on Al	DUCC _{<i>t</i>} /SUCC	0.5	0.892 ± 0.047
27 J on Al	DUCC _{<i>s</i>} /SUCC	0.5	0.781 ± 0.041
24 J on Al	FSSR/SUCC	0.67	0.062 ± 0.015

The results for the ratios of the DUCC to the SUCC integrated reflectivities in table 7.5 indicate that the ADP crystals of the DUCC are of lower quality, having a R_{int} larger than the literature value, the KAP crystals of the SUCC exhibit a lower integrated reflectivity, or some combination of the two. This is consistent with the crystal broadening value of the DUCC of table 7.4, which is higher than expected. Nevertheless, it is

difficult to draw any definitive conclusions from these results, as none of the R_{int} values have been directly measured.

One path to leverage the integrated reflectivity ratios is through the R_{int} of the FSSR from the simulated efficiency. Applying the method described previously and using $\gamma(E)$ results in an integrated reflectivity of $(2.752 \pm 0.633) \mu\text{rad}$, as compared to the literature value of $53.6 \mu\text{rad}$. Inserting the new R_{int} value into the experimental ratio FSSR/SUCC and propagating the uncertainties yields an integrated reflectivity of $(44.39 \pm 14.82) \mu\text{rad}$ for the SUCC. Repeating this process again for the DUCC results in $(37.13 \pm 11.98) \mu\text{rad}$. Though this calculation hinges on the correctness of the FSSR R_{int} value, it does qualitatively align with the crystal broadening results, where the FSSR displays significantly better resolution than expected and the DUCC and SUCC values are appreciably close, considering the differences in geometry. Still, these conclusions should be taken with a grain of salt, as the relation between crystal broadening and integrated reflectivity is not straightforward due to the interplay of geometry influence, photon energy dependence of R_{int} , and possible crystal defect effects.

In any case, it is clear that the FSSR integrated reflectivity and therefore non-local (i.e. ignoring local defects) crystal quality exceeds expectations. This is counter-balanced by the presence of numerous meaningful crystal defects and an inherent Al absorption edge. Accordingly, the FSSR in its current state with the mica crystal is unsuited to EXAFS of the Al K-edge. If another suitable crystal of good quality without the drawbacks of mica could be guaranteed, the FSSR would be a powerful tool capable of high-resolution, high signal-to-noise ratio absorption spectra for use in EXAFS.

7.3. Setup Validation

As of yet, the spectrometers, and by extension the experimental setup have been assessed without quantitative comparison to similar experiments. To remedy this and place the captured spectra in a broader context, the conversion efficiency of the PHELIX laser energy into the He- α emission line of aluminum will be extracted. I will then check the reasonableness of the results by comparing them to the expected order of magnitude estimated from the literature. A more exacting comparison is not possible in this case due to the fundamental differences between experimental setups and studied backlighter materials.

7.3.1. Conversion Efficiency into He- α Line of Aluminum

I determine the conversion efficiency of the laser energy into the Al He- α line by first processing the source spectra of aluminum shots as described in chapter 6 without the binning step, then multiplying the resulting $N_{st,eV}$ with 4π and ΔE to get the total number of emitted photons E_{total} in each energy interval covered by a given pixel. I then approximate integrating by summing over all the energy intervals included in the He- α line, avoiding the neighboring other heliumlike ion emission line. An example of an integration area is depicted in fig. 7.10. Multiplying the energy of the line, i.e. 1598.4 eV , onto this sum yields the total energy emitted into the He- α line. The ratio of this quantity to the laser energy then gives the desired conversion efficiency.

As with the R_{int} ratio, the conversion efficiency CE using the FSSR can alternatively be determined through the simulated efficiency of the FSSR. As before, I begin by interpolating the simulated efficiency γ of the

FSSR, with which I can use the formula

$$CE = \frac{\sum_i (N_{det}(E_i)/\gamma(E_i)) \cdot 1598.4 \text{ eV}}{E_{laser}}, \quad (7.13)$$

wherein the sum runs over the same integration area as the first method.

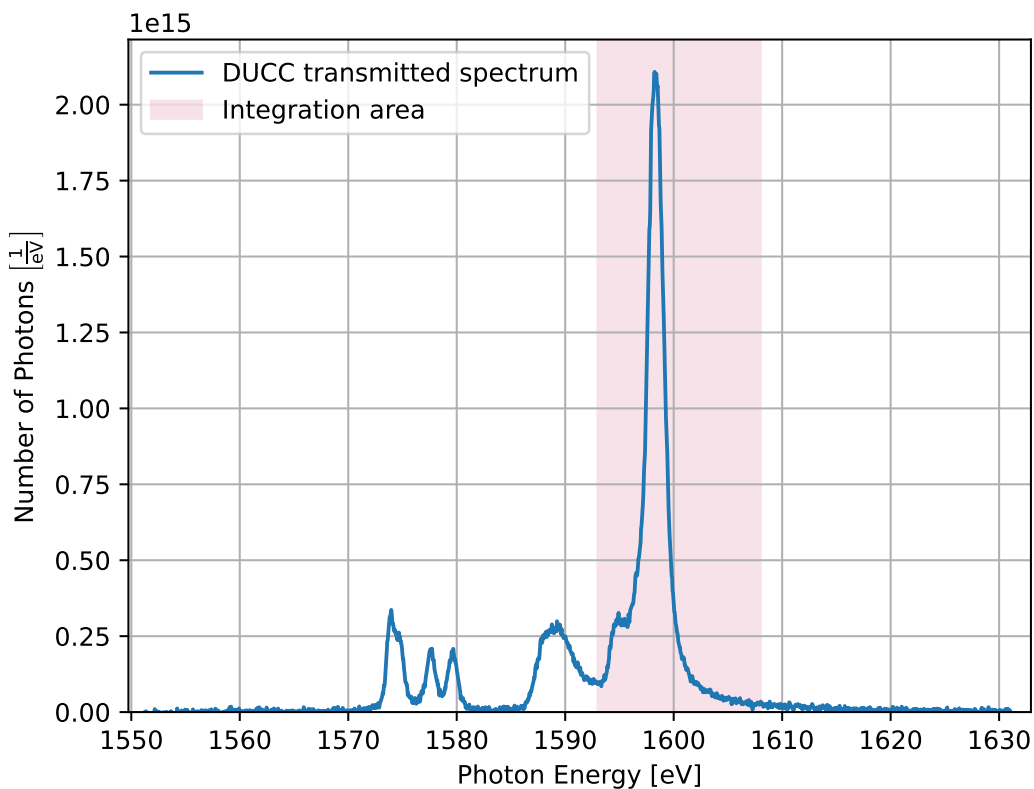


Figure 7.10.: Spectrum from a 27 J shot on aluminum (event 19) captured with the transmission channel of the DUCC and utilized to determine the conversion efficiency. The area over which the signals belonging to the Al He- α line are summed is depicted in pink.

Table 7.6.: Conversion efficiency of the laser energy into the He- α line of aluminum, given in percent. DUCC_{*t*} refers to the transmission channel of the DUCC, DUCC_{*s*} to the source channel. FSSR_{*sim*} is calculated using the simulated efficiency of the FSSR from Artem Martynenko.

Shot	Spectrometer	Conversion Efficiency
27 J on Al	DUCC _{<i>t</i>}	(4.50±2.25)%
27 J on Al	DUCC _{<i>s</i>}	(3.76±1.88)%
24 J on Al	FSSR	(0.20±0.10)%
24 J on Al	FSSR _{<i>sim</i>}	(3.89±0.28)%
24 J on Al	SUCC	(2.55±1.28)%
27 J on Al	SUCC	(2.71±1.36)%

For context, I estimate the expected order of magnitude for the results using values of the conversion efficiency of the Z-Beamlet laser at Sandia National Laboratories into He-like emission lines of laser-plasma of various elements ranging from Z= 21 to 32 [56]. Extrapolating from the conversion efficiencies in fig. 5 of Ruggles *et. al.*'s paper, a *CE* into the Al He- α line on the order of 1-10⁻¹% is reasonable. Consequently, every spectrometer yields acceptable values. Moreover, all the *CE* lie approximately within each others error ranges, with the exception of the FSSR result derived using the literature *R_{int}* value, again reinforcing the notion that the *R_{int}* from simulation is closer to the actual value. This agreement serves to demonstrate the consistency of the setup across all spectrometers and support the validity of the spectrum processing procedure, with the caveat that the results only consider orders of magnitude.

8. Summary and Outlook

In the course of this work, I designed, built, and tested two spectrometers, namely the Dual Unbent Crystal Spectrometer (DUCC) and the Focusing Spectrograph with Spatial Resolution in 1 Dimension (FSSR-1D), with the purpose of conducting XAFS on aluminum samples in warm dense matter experiments at GSI and eventually FAIR, which presents the unique opportunity to combine heavy-ion beams for WDM heating and laser-driven backscatterers as an x-ray source. The DUCC aims to resolve XANES around the Al K-edge and leverages a dual crystal design to simultaneously capture a transmitted and source spectrum on one detector. With its flat crystal design, it emphasizes consistency and simplicity. The FSSR-1D is designed to measure EXAFS and sports a spherically bent crystal, which enables spectral focusing and 1D spatial imaging onto the detector, significantly reducing background and increasing the signal-to-noise ratio (SNR). This spectrometer prioritizes performance, having the potential for excellent spectral resolution with a larger energy range than the DUCC, at the cost of higher complexity and possibly lower consistency.

The designs were informed by considerations stemming from the unique requirements of the experimental setup and the purpose of the spectrometers, which include: covering the energy ranges relevant to XANES (\sim 1540-1585 eV) and EXAFS (\sim 1560-1810 eV) respectively, limitations imposed by the WDM sample size (\leq 1 mm) due to the uniformity requirements of the heavy-ion heating, goals for the spectral resolution for observing XANES ($\Delta E \leq$ 1 eV) and EXAFS ($\Delta E <$ 10 eV), achieving sufficient intensity on the detector for a workable SNR, and keeping the physical size (< 550 mm) within the confines of the setup. In theory and simulation, both spectrometers fulfill all the considerations, with the DUCC covering an energy range of 1541-1618 eV, leading to a sample size of 0.75 mm, and having a spectrometer length of 235.17 mm. The FSSR-1D records in an energy range of 1465-1755 eV, gives a sample size of 1.07 mm, and has a spectrometer length of 404.30 mm. Using *mmpxrt* simulations, the energy resolutions were determined, which included an estimation of the crystal properties' contribution to the DUCC resolution, resulting in $\Delta E = 0.703$ eV for the DUCC and $\Delta E = 3.097$ eV for the FSSR-1D. The largest contribution to ΔE originated from the source broadening for the DUCC and the crystal properties for the FSSR-1D. With the schemes theoretically proven, the spectrometers were mechanically modeled using *Autodesk Inventor 2020* and fabricated. Each spectrometer takes into account the harsh experimental conditions by shielding the sensitive crystals and camera chips, where the chips are further insulated from visible light, and includes necessary parts to fully align the spectrometers in the experimental setup, which must be especially exacting for the FSSR-1D.

In a laser-only experiment using the PHELIX beam conducted in May, 2023, which is part of a series of preparatory experiments for eventual WDM experiments at FAIR, I tested and vetted the DUCC and FSSR, as well as another spectrometer designed by Philipp Hesselbach called the Single Unbent Crystal Spectrometer (SUCC), whose geometry effectively corresponds to a single channel of the DUCC, adjusted to accommodate a KAP crystal instead of ADP, and is intended for capturing wide energy range (1400-1800 eV) source spectra as a control. The spectral data gathered as TIFF images is processed and analyzed by a *python3* code I developed called *AXAWOTLS*, designed from the ground up to be applicable during future beamtimes using any spectrometer. With this code, I extracted source spectra of every backscatterer material,

produced x-ray absorption spectra, and calculated the spectral resolution, ratio of integrated reflectivity, and conversion efficiency of laser energy into the Al He- α line for each spectrometer.

Every spectrometer exhibits the expected energy range with generally sufficient SNR, assuring that the basic geometries and designs are successful. Additionally, the x-ray source spectra behave as anticipated and yield reasonable photon numbers. In contrast, each spectrometer performs to varying degrees when extracting x-ray absorption spectra. The SUCC delivers absorption curves with excellent agreement with the literature, where the crystal calibration method and the smooth backscatter spectra from teflon prove to be effective. The DUCC also performs well, albeit with notable features in the absorption curve due to the lack of a suitable crystal calibration shot and the requirement of rare-earth backscatterers, which exhibit structure-rich source spectra. Despite this, the results speak for the double channel design, since it enables fairly accurate absorption spectrum extraction even without crystal calibration. The same cannot be said of the FSSR, which did not produce any reasonable absorption spectra. The spectrometer is hindered most significantly by the poor quality of its mica crystal as well as the presence of aluminum in mica's chemical makeup, leading to an Al K-edge even in source spectra. These aspects heavily distort the fine structures around the absorption edge, making the constellation untenable for XAFS applications.

On the other hand, the quantitative analyses yield surprising results. With the help of a simulation of the FSSR conducted by Artem Martynenko, the integrated reflectivity of the mica crystal could be estimated directly from the aluminum spectra, giving an R_{int} of $(2.752 \pm 0.633) \mu\text{rad}$, over an order of magnitude lower than the value of $28.9 \mu\text{rad}$ used in the *mmpxrt* simulation. This result is supported by an experimentally derived spectral resolution of $(1.724^{+0.145}_{-0.132}) \text{ eV}$, which is a significant improvement on the simulation value. Propagating the R_{int} of the FSSR to other spectrometers using the integrated reflectivity ratios results in $(44.39 \pm 14.82) \mu\text{rad}$ for the SUCC and $(37.13 \pm 11.98) \mu\text{rad}$ for the DUCC, the latter of which is ~ 16 times higher than the R_{int} of the DUCC's *mmpxrt* simulation. As with the FSSR, the experimental resolutions qualitatively reflect these findings, with $(2.842^{+0.097}_{-0.089}) \text{ eV}$ for the total spectral resolution of the SUCC and $(1.599^{+0.119}_{-0.113}) \text{ eV}$ for the broadening due to crystal properties of the DUCC, which alone exceeds the resolution requirement for XANES of $\Delta E \leq 1 \text{ eV}$ and outpaces the simulated crystal broadening of 0.238 eV . Consequently, the DUCC design does not currently fulfill its design requirement. In contrast, the FSSR exhibits excellent resolution despite its defect-heavy crystal, displaying the power of the FSSR geometry and potential of the mica crystal for other spectroscopy applications. Notably, the SUCC has more than sufficient resolution and energy range for EXAFS with a crystal with few defects. Finally, the conversion efficiency results show good agreement between all spectrometers and fall within a reasonable order of magnitude as compared to literature, i.e. on the order of a few percent. This demonstrates that the experimental setup yields consistent measurements of the source across different spectrometers that qualitatively agree with the literature.

In light of these results, it is clear that:

1. Crystal quality plays a crucial role in the extraction of absorption spectra with resolved fine-structure.
2. Smooth backscatter spectra greatly enhance the quality of the absorption spectra, since structure in the source spectra are passed on enough to be significant.
3. Identical spectrometer channels for the transmitted and source spectra markedly improve absorption curve quality, even for less than ideal shots.
4. The ADP and mica crystals are unsuitable for this experimental setup, the former due to higher than anticipated integrated reflectivity, and the latter because of the aluminum in its chemical makeup, along with numerous defects.

With these findings in mind, I recommend that the next spectrometer, which will be designed for the combined heavy-ion beam/intense laser experiment of 2024, use the DUCC geometry adapted for the KAP crystals of the SUCC, in combination with teflon backscatterers. This design leverages the smooth spectrum of teflon with the high x-ray collection of KAP, as well as the advantages offered by the dual channels. Furthermore, the spectral resolution and energy range allows for EXAFS, as shown by the SUCC. The flat crystal design also ensures reliability and ease-of-use, which are essential when considering the high complexity of a combined experiment. Lastly, the individual features of the spectrometer have all already been proven to work, reducing the potential for unforeseen difficulties during a beamtime.

In conclusion, the careful design, realization, and detailed analysis of the spectrometers, independent of and in relation to the backscatterers, are an important contribution to the optimization of XAFS of heavy-ion heated aluminum using laser-driven plasmas as x-ray sources. The recommended spectrometer design for the 2024 combined experiment and the analysis code *AXAWOTLS* will simplify workflow during beamtimes and enable the extraction of high-resolution, high signal-to-noise ratio absorption spectra for EXAFS of aluminum, helping to pave the way to new WDM physics in the future.

Bibliography

- [1] D. Riley, Warm Dense Matter: Laboratory Generation and Diagnosis, IOP Publishing (2021), doi: 10.1088/978-0-7503-2348-2.
- [2] K. Falk, Experimental methods for warm dense matter research, High Power Laser Science and Engineering, **6**:e59 (2018), doi:10.1017/hpl.2018.53.
- [3] F. Graziani *et al.*, Frontiers and challenges in warm dense matter, volume 96, Springer Science & Business (2014).
- [4] M. Koenig *et al.*, Progress in the study of warm dense matter, Plasma Physics and Controlled Fusion, **47**(12B):B441 (2005), doi:10.1088/0741-3335/47/12B/S31.
- [5] G. Collins *et al.*, Measurements of the equation of state of deuterium at the fluid insulator-metal transition, Science, **281**(5380):1178–1181 (1998), doi:10.1126/science.281.5380.1178.
- [6] N. Tahir *et al.*, Planetary physics research at the Facility for Antiprotons and Ion Research using intense ion beams, The European Physical Journal Plus, **137**(2):273 (2022), doi:10.1140/epjp/s13360-022-02476-2.
- [7] V. Bagnoud *et al.*, Commissioning and early experiments of the PHELIX facility, Applied Physics B, **100**:137–150 (2010), doi:10.1007/s00340-009-3855-7.
- [8] M. Millot *et al.*, Nanosecond X-ray diffraction of shock-compressed superionic water ice, Nature, **569**(7755):251–255 (2019), doi:10.1038/s41586-019-1114-6.
- [9] M. Altarelli, The European X-ray free-electron laser facility in Hamburg, Nuclear Instruments and Methods in Physics Research Section B: Beam Interactions with Materials and Atoms, **269**(24):2845–2849 (2011), doi:10.1016/j.nimb.2011.04.034.
- [10] D. Riley, Generation and characterisation of warm dense matter with intense lasers, Plasma Physics and Controlled Fusion, **60**(1):014033 (2017), doi:10.1088/1361-6587/aa8dd5.
- [11] L. Dubrovinsky *et al.*, In situ X-ray study of thermal expansion and phase transition of iron at multimegarbar pressure, Physical Review Letters, **84**(8):1720 (2000), doi:10.1103/PhysRevLett.84.1720.
- [12] T. Döppner *et al.*, Observing the onset of pressure-driven K-shell delocalization, Nature, 1–6 (2023), doi:10.1038/s41586-023-05996-8.
- [13] S. Vinko *et al.*, Creation and diagnosis of a solid-density plasma with an X-ray free-electron laser, Nature, **482**(7383):59–62 (2012), doi:10.1038/nature10746.

- [14] N. Tahir *et al.*, Studies of high-energy density states using isochoric heating of matter by intense heavy ion beams: the HEDgeHOB Collaboration, *Physica Scripta*, **2008**(T132):014023 (2008), doi:10.1088/0031-8949/2008/T132/014023.
- [15] K. Schoenberg *et al.*, High-energy-density-science capabilities at the Facility for Antiproton and Ion Research, *Physics of plasmas*, **27**(4):043103 (2020), doi:10.1063/1.5134846.
- [16] R. Torchio *et al.*, Probing local and electronic structure in Warm Dense Matter: single pulse synchrotron x-ray absorption spectroscopy on shocked Fe, *Scientific reports*, **6**(1):1–8 (2016), doi:10.1038/srep26402.
- [17] R. W. Lee *et al.*, Finite temperature dense matter studies on next-generation light sources, *JOSA B*, **20**(4):770–778 (2003), doi:10.1364/JOSAB.20.000770.
- [18] H. Lee *et al.*, X-ray Thomson-scattering measurements of density and temperature in shock-compressed beryllium, *Physical review letters*, **102**(11):115001 (2009), doi:10.1103/PhysRevLett.102.115001.
- [19] T. Hall *et al.*, Experimental observation of ion correlation in a dense laser-produced plasma, *Physical review letters*, **60**(20):2034 (1988), doi:10.1103/PhysRevLett.60.2034.
- [20] M. Newville, Fundamentals of XAFS, *Reviews in Mineralogy and Geochemistry*, **78**(1):33–74 (2014), doi:10.2138/rmg.2014.78.2.
- [21] A. Lévy *et al.*, X-ray absorption for the study of warm dense matter, *Plasma Physics and Controlled Fusion*, **51**(12):124021 (2009), doi:10.1088/0741-3335/51/12/124021.
- [22] Ringbeschleuniger SIS18 – der Rekordhalter, URL <https://www.gsi.de/forschungbeschleuniger/beschleunigeranlage/ringbeschleuniger>.
- [23] D. Varentsov, HHT Experimental Area, URL https://www.gsi.de/work/forschung/appamml/plasmaphysikphelix/anlagen_bei_sis18_hht.
- [24] D. Hoffmann *et al.*, Frontiers of dense plasma physics with intense ion and laser beams and accelerator technology, *Physica Scripta*, **2006**(T123):1 (2006), doi:10.1088/0031-8949/2006/t123/001.
- [25] H.-J. Kunze, Introduction to plasma spectroscopy, volume 56, Springer Science & Business Media (2009), doi:<https://doi.org/10.1007/978-3-642-02233-3>.
- [26] O. Renner and F. Rosmej, Challenges of x-ray spectroscopy in investigations of matter under extreme conditions, *Matter and Radiation at Extremes*, **4**(2):024201 (2019), doi:10.1063/1.5086344.
- [27] A. Levy *et al.*, Double conical crystal x-ray spectrometer for high resolution ultrafast x-ray absorption near-edge spectroscopy of Al K edge, *Review of Scientific Instruments*, **81**(6):063107 (2010), doi:10.1063/1.3441983.
- [28] M. Siegbahn, The Spectroscopy of X-rays, volume 10, Oxford University Press, H. Milford (1925).
- [29] A. Mottana, 1913–2013—The centennial of X-ray absorption spectroscopy (XAS): Evidences about a question still open, *Journal of Electron Spectroscopy and Related Phenomena*, **196**:14–19 (2014).
- [30] R. Stumm von Bordwehr, A history of X-ray absorption fine structure, in *Annales de Physique*, volume 14, 377–465 (1989).

- [31] A. Mottana and A. Marcelli, The historical development of X-ray Absorption Fine Spectroscopy and of its applications to Materials Science, in R. Pisano (editor), *A Bridge between Conceptual Frameworks: Sciences, Society and Technology Studies*, 275–301, Springer (2015), doi:10.48550/arXiv.1312.5295.
- [32] R. Eason *et al.*, Improved laser-EXAFS studies of aluminium foil, *Journal of Physics C: Solid State Physics*, **17**(28):5067 (1984), doi:10.1088/0022-3719/17/28/022.
- [33] O. Peyrusse *et al.*, K-edge Absorption spectra in Warm Dense Matter, in *AIP Conference Proceedings*, volume 1161, 200–206, American Institute of Physics (2009), doi:10.1063/1.3241191.
- [34] A. Fontaine *et al.*, Soft X-ray absorption and EXAFS on the K edge of aluminium, *Journal of Physics F: Metal Physics*, **9**(10):2143 (1979), doi:10.1088/0305-4608/9/10/023.
- [35] W. Bragg and W. Bragg, The X-ray spectrometer, *Nature*, **94**(2347):199–200 (1914).
- [36] Q. Yang *et al.*, Focusing X-ray spectrograph with spatial resolution and uniform dispersion, *Nuclear Instruments and Methods in Physics Research Section A: Accelerators, Spectrometers, Detectors and Associated Equipment*, **634**(1):52–58 (2011), doi:10.1016/j.nima.2011.01.032.
- [37] O. Renner *et al.*, Vertical variant of a double channel-cut crystal spectrometer for investigation of laser-generated plasmas, *Review of scientific instruments*, **70**(7):3025–3031 (1999), doi:10.1063/1.1149863.
- [38] G. Hölzer *et al.*, Flat and spherically bent muscovite (mica) crystals for X-ray spectroscopy, *Physica Scripta*, **57**(2):301 (1998), doi:10.1088/0031-8949/57/2/029.
- [39] F. Blasco *et al.*, Portable, tunable, high-luminosity spherical crystal spectrometer with an x-ray charge coupled device, for high-resolution x-ray spectromicroscopy of clusters heated by femtosecond laser pulses, *Review of scientific instruments*, **72**(4):1956–1962 (2001), doi:10.1063/1.1355273.
- [40] H. H. Johann, Die erzeugung lichtstarker röntgenspektren mit hilfe von konkavkristallen, *Zeitschrift für Physik*, **69**:185–206 (1931), doi:10.1007/BF01798121.
- [41] P. Monot *et al.*, High-sensitivity, portable, tunable imaging X-ray spectrometer based on a spherical crystal and MCP, *Nuclear Instruments and Methods in Physics Research Section A: Accelerators, Spectrometers, Detectors and Associated Equipment*, **484**(1-3):299–311 (2002), doi:10.1016/S0168-9002(01)01991-X.
- [42] A. Y. Faenov *et al.*, High-performance x-ray spectroscopic devices for plasma microsources investigations, *Physica Scripta*, **50**(4):333 (1994), doi:10.1088/0031-8949/50/4/003.
- [43] T. Pikuz *et al.*, Bragg X-ray optics for imaging spectroscopy of plasma microsources, *Journal of X-ray Science and Technology*, **5**(3):323–340 (1995), doi:10.1006/jxra.1995.0009.
- [44] T. Döppner *et al.*, High order reflectivity of highly oriented pyrolytic graphite crystals for x-ray energies up to 22 keV, *Review of Scientific Instruments*, **79**(10):10E311 (2008), doi:10.1063/1.2966378.
- [45] B. Young *et al.*, High-resolution x-ray spectrometer based on spherically bent crystals for investigations of femtosecond laser plasmas, *Review of Scientific Instruments*, **69**(12):4049–4053 (1998), doi:10.1063/1.1149249.
- [46] B. L. Henke, E. M. Gullikson and J. C. Davis, X-ray interactions: photoabsorption, scattering, transmission, and reflection at E= 50-30,000 eV, Z= 1-92, *Atomic data and nuclear data tables*, **54**(2):181–342 (1993), doi:10.1006/adnd.1993.1013.

- [47] C. Ferrari *et al.*, Characterization of ammonium dihydrogen phosphate crystals for soft X-ray optics of the Beam Expander Testing X-ray facility (BEaTriX), *Journal of Applied Crystallography*, **52**(3):599–604 (2019), doi:10.1107/S1600576719004631.
- [48] P. Rajesh and P. Ramasamy, Growth and characterization of large size ADP single crystals and the effect of glycine on their growth and properties, *Optical Materials*, **42**:87–93 (2015), doi:10.1016/j.optmat.2014.12.024.
- [49] M. Alkhimova *et al.*, Determination of spectral reflectivity of spherically bent mica crystals applied for diagnostics of relativistic laser plasmas, in *Journal of Physics: Conference Series*, volume 774, 012115, IOP Publishing (2016), doi:10.1088/1742-6596/774/1/012115.
- [50] G. P. Loisel *et al.*, Measurement and models of bent KAP (001) crystal integrated reflectivity and resolution, *Review of Scientific Instruments*, **87**(11) (2016), doi:10.1063/1.4960149.
- [51] M. Šmíd, X. Pan and K. Falk, X-ray spectrometer simulation code with a detailed support of mosaic crystals, *Computer Physics Communications*, **262**:107811 (2021), doi:10.1016/j.cpc.2020.107811.
- [52] J. Gilfrich, D. Brown and P. Burkhalter, Integral reflection coefficient of X-ray spectrometer crystals, *Applied Spectroscopy*, **29**(4):322–326 (1975), doi:10.1366/00037027577445591.
- [53] D. Giulietti and L. A. Gizzi, X-ray emission from laser-produced plasmas, Ed. Compositori (1998), doi:10.1007/BF02874624.
- [54] W. Wiese, R. Huddlestome and S. Leonard, *Plasma Diagnostic Techniques*, RH Hudddlestone, SL Leonard, editors, **21**:201–264 (1965).
- [55] A. C. Thompson, D. Vaughan *et al.*, X-ray data booklet, volume 8, Lawrence Berkeley National Laboratory, University of California Berkeley, CA (2001).
- [56] L. Ruggles *et al.*, Measurements of 4–10 keV x-ray production with the Z-Beamlet laser, *Review of scientific instruments*, **74**(3):2206–2210 (2003), doi:10.1063/1.1537854.

I. Crystal Considerations

The choice of crystal for the spectrometers took several aspects into account:

- **Lattice Spacing:** The lattice spacing must lie in a range that ensures the Bragg condition is fulfilled for reasonable incident angles depending on the spectrometer geometry and the consideration 2 outlined above.
- **Diffraction Order:** Reflection in the first order is preferred, as the lower orders typically display higher reflection efficiency and cover a lower energy range, corresponding to higher intensities from the plasma source compared to intensities at higher energies [26, 41].
- **Bendability:** A bent crystal allows for high intensities on the detector and reduces shot-to-shot fluctuations [27]. It could also potentially offer spatial resolution.
- **Intrinsic Properties:** As discussed in section 2.4, a compromise between a small rocking curve width and sufficiently high integrated reflectivity is required to reach high resolutions while maintaining good luminosity on the detector.
- **Availability:** The crystals themselves must be acquirable.

It is noted that various crystals were considered for each spectrometer, but were gradually eliminated during the initial design development. For example, KAP was considered for the flat crystal geometry, but was rejected since it would lead to a too high spectrometer length. Quartz also came into consideration for the FSSR-1D, but in the end did not allow for a FSSR geometry that fulfilled the experimental requirements.

II. Spectrometer Simulations

To investigate the spectrometer properties and validate the design I ran ray tracing simulations, using a self-made simple ray tracing code and the python3 ray tracing code mmpxrt, built by Michal Šmíd at the Helmholtz-Zentrum Dresden-Rossendorf [51]. mmpxrt is specialized for x-ray spectrometers and supports bent crystal geometries.

First, I will discuss the simple ray tracing code and its application in section 4.1. This is followed by the presentation and discussion of the results of the mmpxrt simulations of the DUCC and FSSR spectrometers in sections 4.2 and 4.3 respectively. Finally, I will summarize the results of the simulations and present the expected contributions to the resolution for each spectrometer in section 4.4.

i. Simple Ray Tracing of the Focusing Spectrograph with Spatial Resolution

It should be noted that this code is not, strictly speaking, a full ray tracing program, as the direction and energy of the rays are not randomly chosen. Despite this I will use the term ray tracing in this section for simplicity.

During the design phase of this work, it was unclear how exactly the detector surface should be orientated for the FSSR-1D. In order to directly test this, I made a simple 2D ray tracing code. The calculation of the rays is done by finding the line equation for each ray before and after reflection on the crystal. It then uses the imaging condition in the vertical plane (see eq. 3.2) to find the optimal intersection point with the detector for each photon energy. The ray tracing follows the steps:

1. The initial ray begins at the source, which is assumed to be a point source, and ends at the contact point with the crystal surface. By taking advantage of the known location of the source, set by the geometry of the spectrometer, and the circle equation of the crystal curvature, the contact point can be calculated for a given Bragg angle, and therefore energy.
2. Using the calculated contact point and the fact that the ray is reflected on the crystal, the line equation of the reflected ray is determined.
3. The reflected ray is propagated until it reaches the distance b given by the imaging condition in the vertical plane. a is calculated by the length of the initial ray. This final point is denoted as the imaging point of the ray.
4. Finally, the detector line is drawn out along the line of best fit of the set of imaging points for a range of energies, where all rays that do not land on the crystal are filtered out.

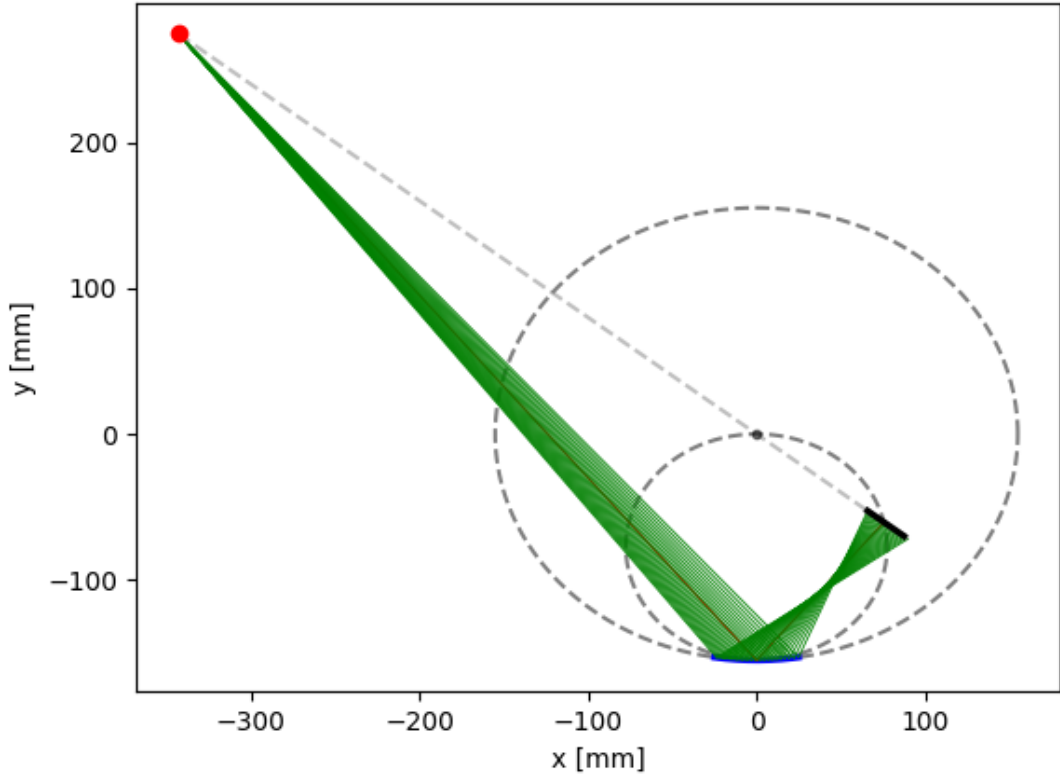


Figure II.1.: Simple ray tracing of the FSSR-1D with a mica crystal with second order diffraction, where $R = 155$ mm, $E_0 = 1600$ eV and $a_0 = 549.7$ mm. The detector length in dispersive direction is 27.6 mm and the crystal length is 50 mm. The red dot represents the source and the red ray is the central ray. The remaining rays are shown in green. The crystal is in blue and the detector in black. The dotted circles depict the crystal curvature and the RC respectively. Finally, the black dot shows the center of the crystal curvature circle.

The code delivers the diagram seen in fig. II.1, where the parameters of the final FSSR-1D are used. Notably, the detector line lies exactly on a symmetry axis of the circle drawn out from the crystal curvature, even though no explicit symmetry relations were used in the calculations. This supports the optimal orientation outlined in section 3.3. In addition, the angle of the central ray to the detector line is 90° , as expected for the FSSR-1D geometry.

To note is that this geometry has many degrees of freedom when fine tuning the spectrometer. As such, it's simpler to set a parameter first, then adjust the others accordingly. In this work, I set the central ray to be incident on the center of the crystal, meaning the central energy E_0 corresponding to this ray doesn't lie in the center of the energy range due to the off-axis source location (relative to the spherical crystal optical axis). Therefore, the easiest way to fine tune the energy range, limited by detector position and size as well as crystal position and size, is to slightly shift the detector location along the symmetry axis mentioned above. In this case, I chose the top end of the detector (positive y direction) to correspond with the topmost ray (lowest energy ray) reflected from the crystal, as seen in fig. II.1. This choice covered the largest possible energy range with this setup. With the offset and orientation set, the placement of the detector is determined.

This code is applicable for all FSSR geometries and can be used to quickly determine the optimal detector placement for any FSSR.

ii. Simulation of the Focusing Spectrograph with Spatial Resolution

I simulated the FSSR-1D with the same parameters as in the final design (see table 4.2) using mmpxrt. In this section I will discuss the quantities relevant to the validation of the final design. For more details about each graph and result of the simulation, refer to [51].

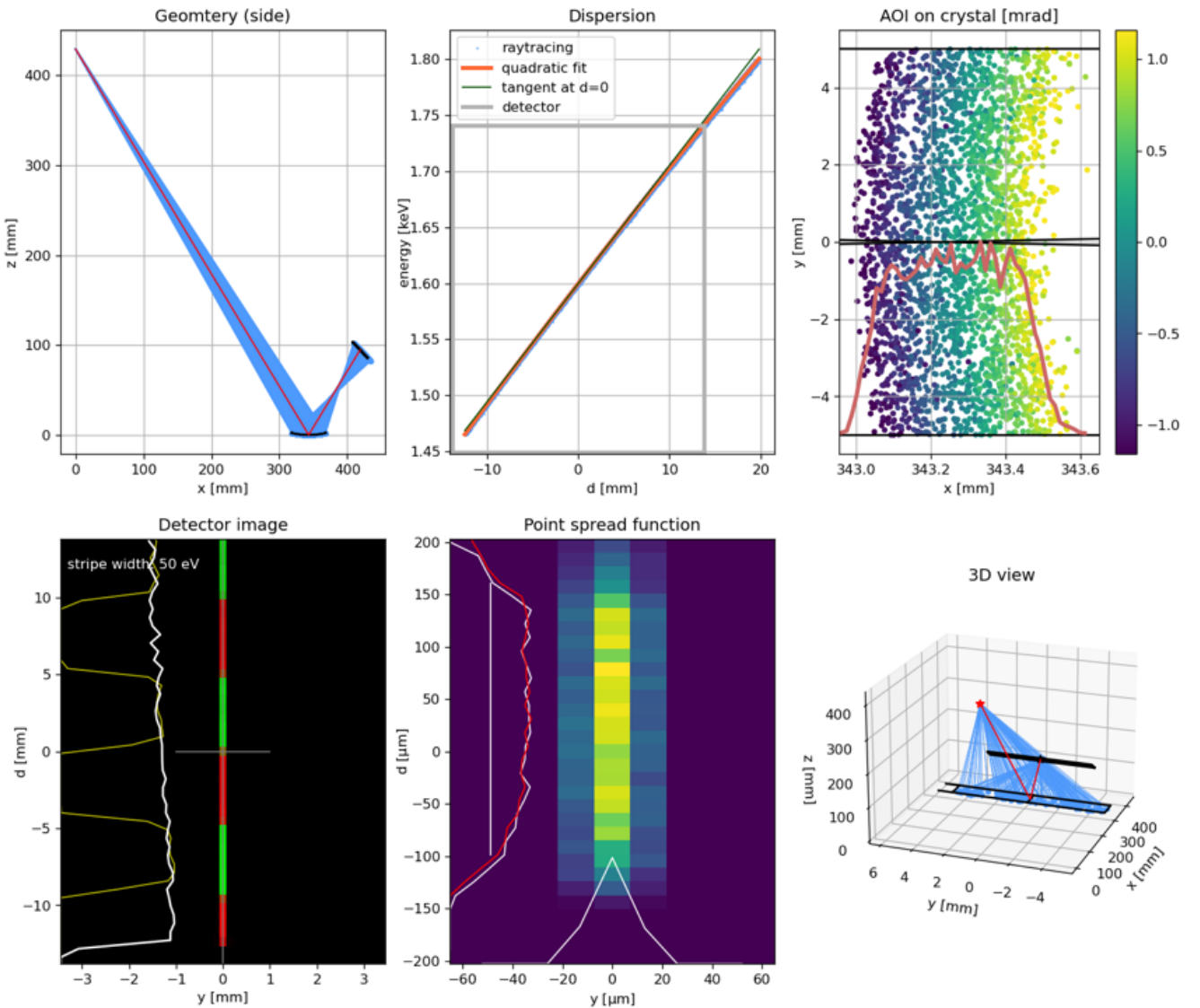
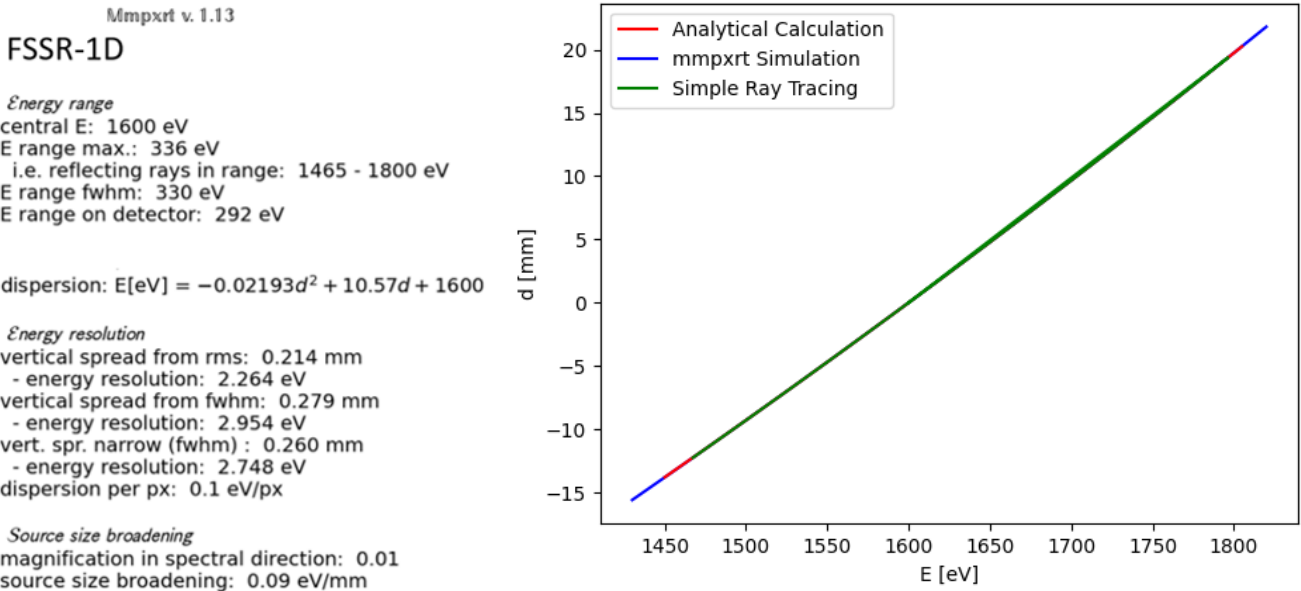


Figure II.2.: Graphical results of mmpxrt simulation of the FSSR-1D, wherein the point spread function used to find the energy resolution is in the bottom middle.



(a) Numerical results of mmpxrt simulation of FSSR-1D with some quantities removed for clarity.

(b) Dispersion of the FSSR-1D calculated with three different methods.

Figure II.3.: (a): Results of simulation of the FSSR-1D with the parameters as in fig. II.1. Simulated using mmpxrt [51]. (b): Comparison of dispersion. Energy range was extended for the simple ray tracing and analytical results to render them visible on the graph.

To run the ray tracing simulation, a number of parameters needed to be input. These include the geometry dependent parameters like radius of crystal curvature and source-crystal distance, among others, along with settings pertaining to the simulation and source/crystal properties. I set the simulation settings according to limitations of the computer and code, where the most important is the parameter `p['simulation']['numerical_intersect_halving']=1`, which increases the runtime but is necessary for simulating curved crystals. As for the source and crystal properties, I set the source to be a cube with length of 0.1 mm and the crystal as a monocrystal with a rocking curve width of 2322 μrad and an integrated reflectivity of 28.9 μrad , as typical values for mica [38].

To assess the accuracy of the simulation, I will first look at the dispersion. I determined the dispersion using three different techniques and graphed them together in fig. II.3b. The simple ray tracing calculation was done by finding d through the absolute distance between the imaging points of a given ray and the central ray. This is an excellent approximation, as the detector line follows the line of imaging points almost exactly, with negligibly small deviations on the order of 10^{-13} mm. For the analytical calculation I used the relation in eq. 3.16. The simulation dispersion is found in fig. II.3a, where one need only take the inverse. It's immediately clear that the results show extremely good agreement. In fact, the lines overlap almost perfectly. This speaks for the validity of all three methods. Furthermore, the dispersion is, as desired, approximately linear over the energy range covered by the detector, as apparent in the fit of the analytical formula

$$d(E) = 1.932 \cdot 10^{-5} \text{ mm/eV}^2 \cdot E^2 + 0.03292 \text{ mm/eV} \cdot E - 102.1 \text{ mm} + \mathcal{O}(E^3). \quad (\text{II.1})$$

The simulation recovers an energy range of 1465 - 1757 eV, which is comparable to the range expected from the FSSR-1D design of approximately 1465 - 1755 eV. Additionally, the dispersion per pixel, using a pixel size of 13.5 μm , is reasonable when compared to the estimated value of 0.14 eV/pixel from the analytical formula. The magnification in dispersive direction and source size broadening are also as expected, taking negligibly small values, with the source broadening resulting in $\Delta E = 0.014$ eV, assuming a source size of 150 μm .

Before discussing the energy resolution, an explanation of each type of resolution given in the mmpxrt results is useful (see fig. II.3a). Each of the three resolutions given is derived from the point spread function (PSF) seen in fig. II.2 using different methods. The first value from "vertical spread from rms" is calculated by taking the root-mean-square of the spread of points in the d direction, then multiplying a factor onto it to approximate a gaussian profile. Consequently, this value is not of much immediate use in this work, as it assumes a distribution. The second value from "vertical spread from fwhm" corresponds to the FWHM of the plot of the profile in dispersive (d) direction, integrating over the y direction. As such, this resolution takes into account the full y range shown in the PSF graph. The third value from "vert. spr. narrow (fwhm)" uses the same process as the second value, with the exception of using only the y range shown by two red lines in the PSF graph. In summary, the first value will not be used in this work, while the choice between the second and third value depends on the y range on the detector one wishes to cover. It is important to mention that this energy resolution result takes only the crystal quality into account.

In the case of the FSSR-1D, the most instructive energy resolution is the second one, as the detector is large enough in the vertical direction (6.9 mm) to capture all the rays in the PSF graph. The result $\Delta E = 2.954$ eV is comparable to an estimated value of $\Delta E_{est} = 2.960$ eV, calculated from the rocking curve width $\Delta\theta = 2322 \mu\text{rad}$ with the formula

$$\Delta E_{est} = E(\theta_0) - E(\theta_0 + \Delta\theta), \quad (\text{II.2})$$

where $E(\theta)$ is determined using Bragg's law (see eq. 3.1). The agreement between the estimated and simulated value speaks for the trustworthiness of the result. To note is that this energy resolution depends directly on the crystal quality, and as such can be noticeably different in the experiment.

iii. Simulation of the Dual Unbent Crystal Spectrometer

As with the FSSR-1D, I simulated the DUCC using the parameters as in the design (see section 4.2.1), where only one channel was considered, as the geometry is analogous along both channels.

The source and simulation parameters in mmpxrt were set just as in section ii, with the exception of leaving out the "numerical_intersect_halving" parameter, since the crystal is flat. The geometry parameters were chosen as in the actual design (see table 4.2). The crystal properties were chosen to correspond to a monocrystal with an integrated reflectivity of 2.32 μrad , taken from [47], and rocking curve width of 800 μrad , which was artificially increased from the literature value of 165 μrad [48], since the simulation did not function for too small a $\Delta\theta$, most likely owing to too few reflected rays.

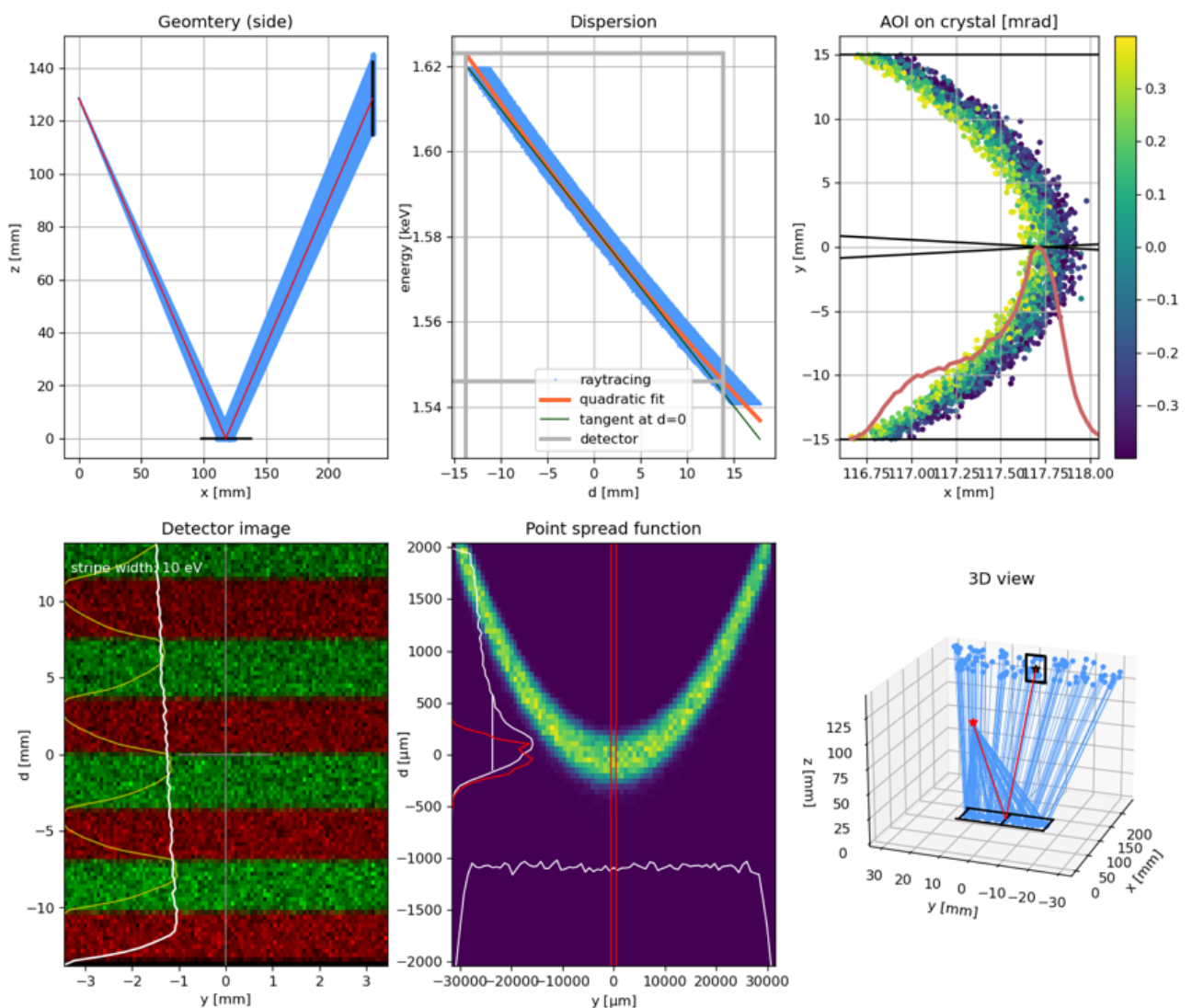


Figure II.4.: Graphical results of mmpxrt simulation of the DUCC, wherein the point spread function used to find the energy resolution is in the bottom middle.

Mmpxrt v. 1.13

DUCC Spectrometer

Energy range

central E: 1580 eV
 E range max.: 79 eV
 i.e. reflecting rays in range: 1541 - 1620 eV
 E range fwhm: 75 eV
 E range on detector: 77 eV

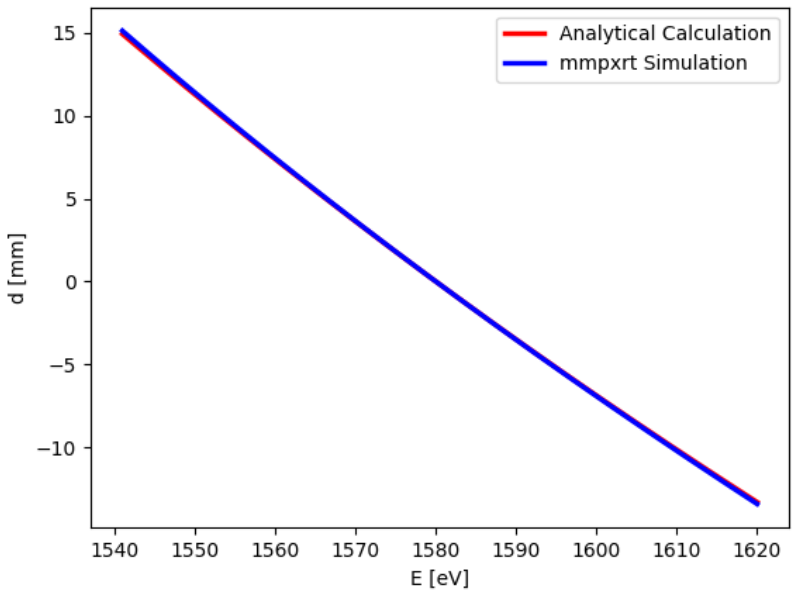
$$\text{dispersion: } E[\text{eV}] = 0.01402d^2 + 2.79d + 1582$$

Energy resolution

vertical spread from rms: 1.516 mm
 - energy resolution: 4.224 eV
 vertical spread from fwhm: 0.791 mm
 - energy resolution: 2.204 eV
 vert. spr. narrow (fwhm) : 0.341 mm
 - energy resolution: 0.952 eV
 dispersion per px: 0.0 eV/px

Source size broadening

magnification in spectral direction: 1.48
 source size broadening: 4.14 eV/mm



(a) Numerical results of mmpxrt simulation of DUCC with some quantities removed for clarity.
 (b) Dispersion of the DUCC calculated with two different methods.

Figure II.5.: (a): Results of simulation of the DUCC with the parameters as in table 4.2. Simulated using mmpxrt [51].
 (b): Comparison of dispersion calculated analytically and through the mmpxrt simulation.

As before, the dispersion $d(E)$ is determined using different methods, namely by the simulation and analytically using eq. 3.8. The results are pictured in fig. II.5b, where again a very good agreement is apparent. In this case the dispersion is also approximately linear, albeit less than for the FSSR-1D, with a fit of the analytical equation resulting in

$$d(E) = 6.306 \cdot 10^{-4} \text{ mm/eV}^2 \cdot E^2 - 2.35 \text{ mm/eV} \cdot E - 2139 \text{ mm} + \mathcal{O}(E^3). \quad (\text{II.3})$$

The energy range as well shows good agreement, with ranges of 1541 - 1618 eV for the simulation and approximately 1541 - 1620 eV for the design. The dispersion per pixel is also as expected, with 0.037 eV/pixel for the analytical dispersion taking into account the pixel size of 13.5 μm , which is low enough to display as 0.0 eV/pixel in the simulation.

In the case of the source broadening, the simulation results slightly deviate from the analytically estimated value. This estimate assumes a source size in the dispersive plane of 150 μm and uses 1-to-1 imaging of a 2D source onto the detector, which follows from the geometry and the fact that source extension in the vertical direction should not affect spectral resolution. Together with the dispersion, this delivers a broadening of 0.592 eV, while the simulation gives a value of 4.14 eV/mm \cdot 0.15 mm = 0.621 eV. The deviation can be possibly traced back to the way that mmpxrt handles the source broadening calculation, which is done using a monochromatic ray tracing, where an offset of the source is introduced for some rays [51]. Accordingly, the source broadening becomes dependent on the crystal quality. The artificially increased rocking curve width therefore leads to higher values of the source broadening in the code. Despite this, the simulation value will be carried over, as the estimate is fairly coarse.

For the energy resolution, as opposed to the FSSR-1D, the third value in fig. II.5a is used, as the detector only covers a fraction of the y range in the PSF graph, so that $\Delta E = 0.952$ eV, while the formula to estimate the spectral resolution from the rocking curve width (see eq. II.2) yields $\Delta E_{est} = 0.238$ eV. Due to the artificial increase of $\Delta\theta$ in the simulation, ΔE_{est} will be used instead of ΔE in this work.

iv. Summary of Simulation Results

For both the DUCC and FSSR-1D spectrometers, the mmpxrt simulations yielded results consistent with the analytical calculations, showing very good agreement for the dispersion, dispersion per pixel and energy range, and good agreement for source broadening. The energy resolution agreed well for the FSSR-1D, while the $\Delta E_{crystal}$ from the DUCC simulation is not meaningful due to the artificially increased $\Delta\theta$.

Since one of the main goals of the simulations was assessing the spectral resolution of each spectrometer, I have gathered and presented the contributions to the resolutions in table 4.1, along with the total spectral resolution ΔE_{tot} calculated by summing all the results.

It is immediately clear that the crystal properties are the main limiting factor on the resolution for the FSSR-1D, while the DUCC resolution is mostly limited by the source broadening, with a significant, though smaller, contribution from the rocking curve width. Here we see the advantage offered by the ADP crystal in comparison to the mica, in that it delivers better spectral resolution, albeit at the cost of lower integrated reflectivity and worse bendability. These results also indicate that the detector resolution does not limit the overall spectral resolution for either spectrometer. In general, both spectrometers have sufficient spectral resolutions to perform their roles outlined in section 4.2.

Table II.1.: Resolution contributions for the DUCC and FSSR-1D spectrometers. In both cases, the source broadening is taken from mmpxrt and assumes a source size of $150\text{ }\mu\text{m}$, and the detector resolution is calculated from the mmpxrt dispersion and uses a pixel size of $13.5\text{ }\mu\text{m}$. The contribution due to the crystal properties for the DUCC is estimated as described in section iii, while for the FSSR-1D it is taken from mmpxrt's second ΔE value. The total spectral resolution is calculated by using error propagation on the source broadening and crystal properties' resolution, then linearly adding on the detector resolution.

ΔE Contributions	DUCC	FSSR-1D
Source Broadening	0.621 eV	0.014 eV
Detector	0.038 eV	0.143 eV
Crystal Properties	0.238 eV	2.954 eV
Total	0.703 eV	3.097 eV

III. Alignment Procedure for FSSR-1D

The alignment process can be broken down into 5 steps. To note is that parts of the alignment are built into the mechanical design itself, such that manual adjustments are not required. I will touch on these aspects after explaining the procedure.

Essential to the alignment are the four optical stages labeled in fig. III.1. The rotation stage is a PR01/M, the large linear stage a LX10/M, and the tip-tilt stage a KM100B/M from *Thorlabs*. The fine linear stage, a TSDS-1 from *SigmaKoki*, serves to adjust the crystal-pin distance and the tip-tilt stage allows for pointing in step 2.

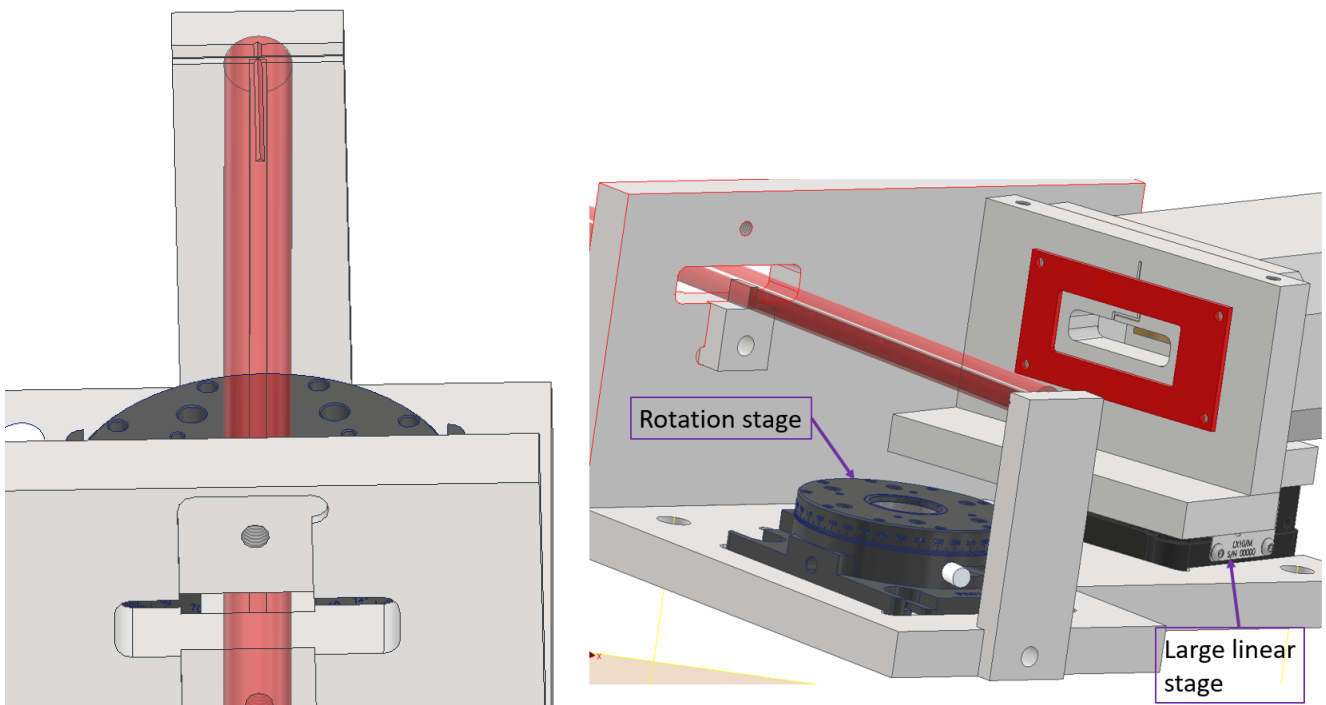
The first three steps are conducted outside the target chamber on an optical table equipped with an expanded collimated laser beam, in our case a HeNe laser, while the last two steps are carried out in the chamber.

1. First, the FSSR-1D without the crystal apparatus is brought into alignment with the HeNe beam for the next steps, simultaneously ensuring that the spectrometer base plate lies parallel to the floor. The HeNe beam is directed onto the opening of the front plate, onto which a pin is affixed, as seen in fig III.1a. The shadow cast by the pin is then aligned with the center of the cross on a plate attached to the back of the base of the FSSR-1D (see fig. III.1b). In this way the beam is parallel to the base plate of the FSSR-1D and to the line drawn out from the pin to the rotation axis of the rotation stage.
2. Now the crystal apparatus, consisting of the rotation stage, fine linear stage, tip-tilt stage and the crystal holder, is put in, as seen in fig. III.1c. Using the fine linear stage and tip-tilt stage, the beam is focused with the crystal onto the surface of the pin (see fig. III.1d), whose distance to the crystal is exactly the focal length of the crystal. This serves to set the location of the Rowland circle and ensure that the crystal center intersects the rotation axis of the rotation stage. It also corrects for any unintended tilts or shifts of the crystal w.r.t the rest of the spectrometer.
3. Next, the central Bragg angle is set by rotating the crystal with the rotation stage. This step leaves the crystal in its final position (see fig. 5.4). In preparation for the next step, the pin is removed and the pointer holder shown in fig. III.2 is attached to the front of the front plate. Analogously to the DUCC, an optical post is set to the required distance and screwed onto the pointer holder.
4. The pointer is then used to orientate the FSSR-1D in the chamber. This is equivalent to fixing the a_0 distance as defined in section 3.2.2.
5. Finally, a laser is shone onto the tip of a needle placed at the TCC. This allows for taking images of the source with photons in the optical range being reflected on the crystal and detected by the CCD camera of the FSSR-1D. By adjusting the distance from chip to crystal using the large linear stage under the camera pictured in fig. III.1b, the position of best focus is found, resulting in the thinnest possible horizontal line on the camera. This is paramount to setting the b_0 distance for the FSSR-1D geometry.

With this the alignment is complete and the FSSR-1D geometry is realized. The most important mechanical details that assist in the alignment are as follows:

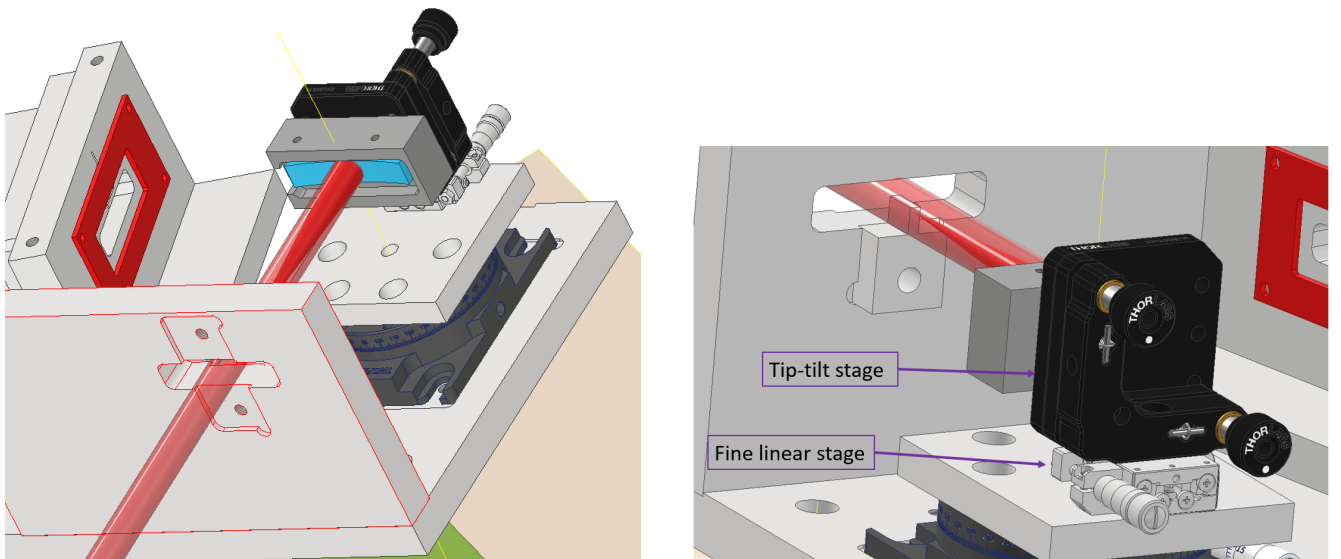
- The rotation stage, front plate, cross plate (used in the first step) and camera linear stage all lie in grooves in the base plate, which fixes their locations and angles w.r.t one another.
- Through additional positioning grooves for the pin and pointer holder, the relative distances between every part is further preserved by mechanical precision. In this way the distance from pin to rotation axis of the rotation stage is set to the focal length of the spherical crystal, allowing the second alignment step to line up the crystal center with the rotation axis.
- Finally, the crystal holder and corresponding connections to the stages ensure that the crystal lies at the correct height and parallel to the base plate, carrying over the alignment achieved in the first step.

With this setup the error of the alignment is mostly limited to mechanical precision, excepting the fourth step, which relies on bare-eye precision. Despite this the overall precision remains excellent, as this uncertainty occurs relatively far from the spectrometer itself, reducing its impact.



(a) Top view of step 1. The HeNe beam is directed through the front plate opening onto the cross plate.

(b) Back view of step 1, where the shadow of the pin is visible in the HeNe beam. The rotation stage and large linear stage are labeled.



(c) Front view of focusing in step 2. The focused HeNe beam is depicted within the main beam in a darker red. The rotation axis of the rotation stage is also shown.

(d) Back view of focusing in step 2. The tip-tilt and fine linear stage are labeled.

Figure III.1.: Model depicting the alignment process for the FSSR-1D using a collimated HeNe laser, which is shown in red. The various optical stages are labeled.

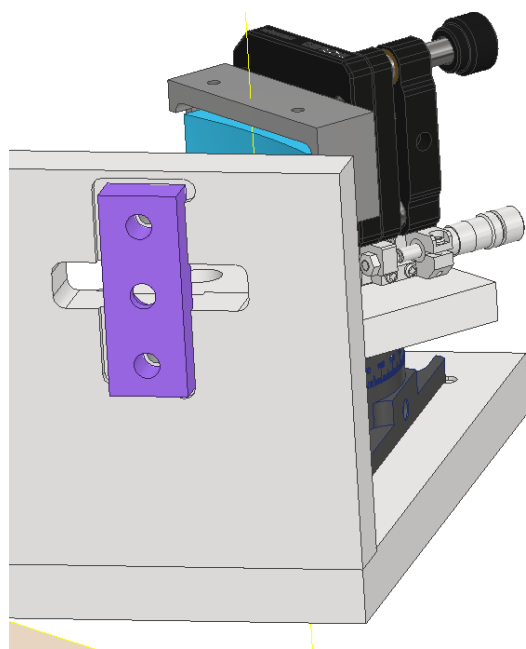
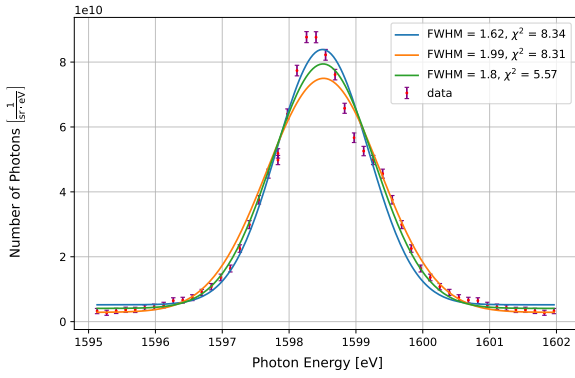


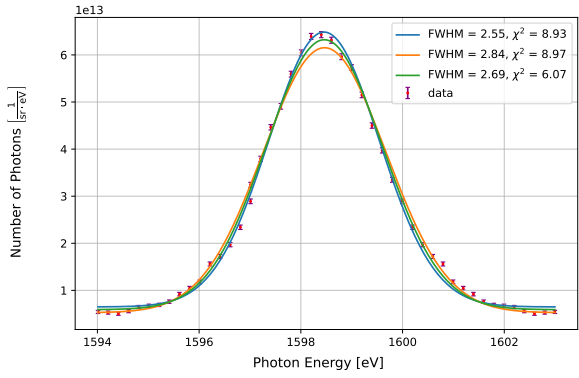
Figure III.2.: Front view of step 3 depicting the pointer holder set in its groove in purple.

IV. Supplementary Results

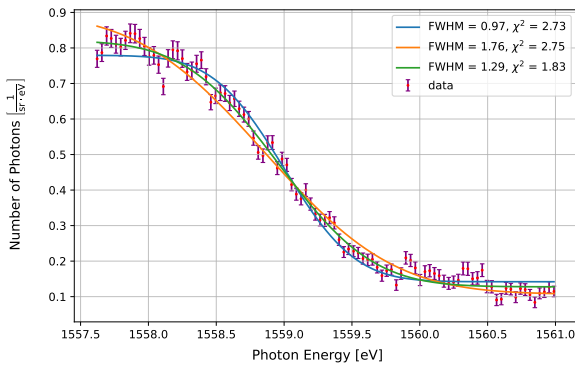
i. Spectral Resolution



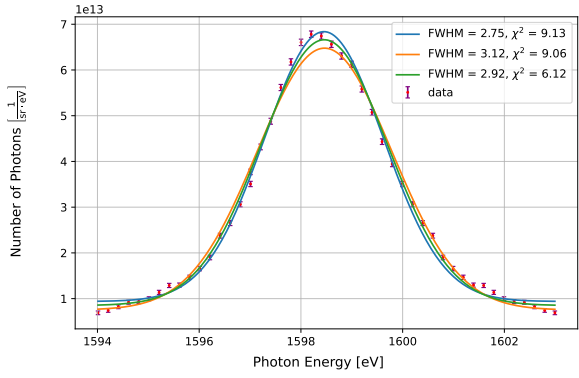
(a) FSSR: Gaussian fit of the He- α peak for a 1.7 J shot on aluminum (event 2).



(b) SUCC: Gaussian fit of the He- α peak for a 24 J shot on aluminum (event 16).



(c) DUCC: Error function fit of the transmission for a 92.7 J shot on samarium (event 31).



(d) SUCC: Gaussian fit of the He- α peak for a 27 J shot on aluminum (event 19).

Figure IV.1.: Fits used to determine the spectral resolution of various spectrometers. The best (green) and worst (blue and orange) fit models are depicted and labeled with their corresponding FWHM and χ^2 values.

ii. Integrated Reflectivity Ratio

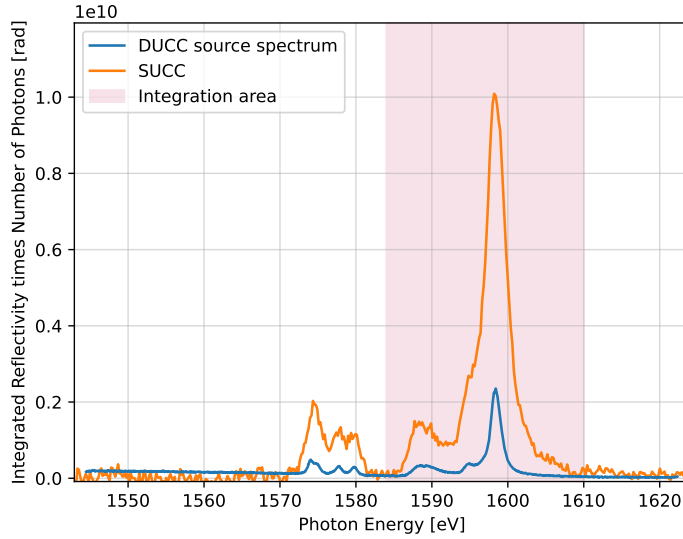


Figure IV.2.: $R_{int} \cdot N_{total}$ for a 27 J shot on aluminum (event 19). The spectra from the source channel of the DUCC and the SUCC are presented, as well as the integration area used to calculate the integrated reflectivity ratio.

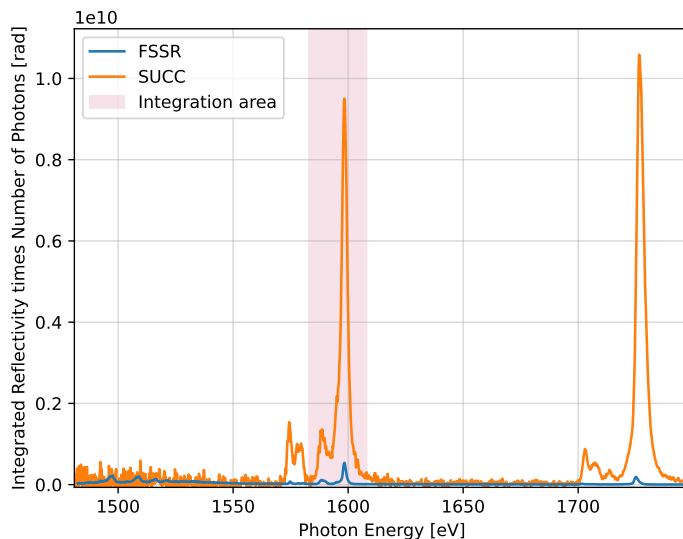
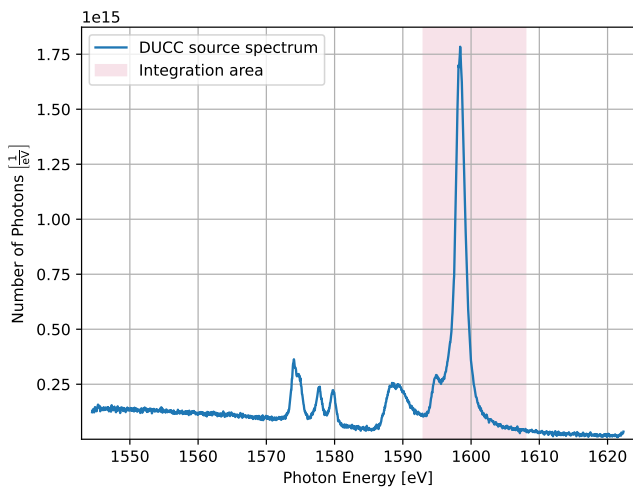
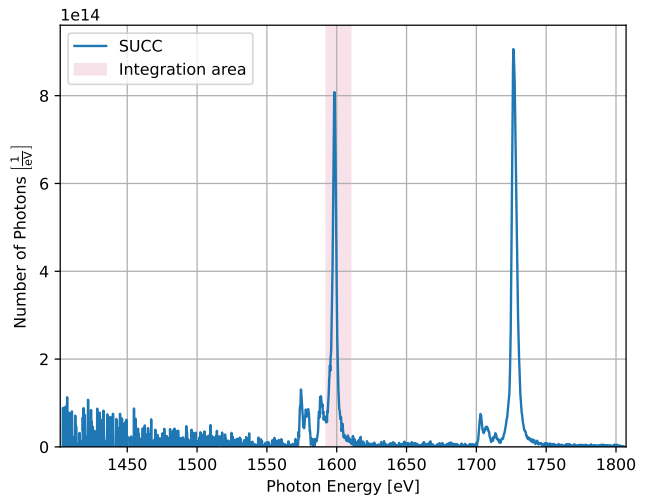


Figure IV.3.: $R_{int} \cdot N_{total}$ for a 24 J shot on aluminum (event 16). The spectra from the FSSR and the SUCC are presented, as well as the integration area used to calculate the integrated reflectivity ratio.

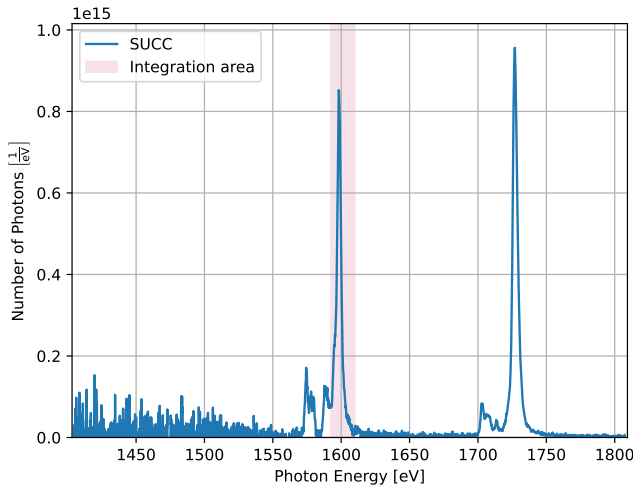
iii. Conversion Efficiency into He- α Line of Aluminum



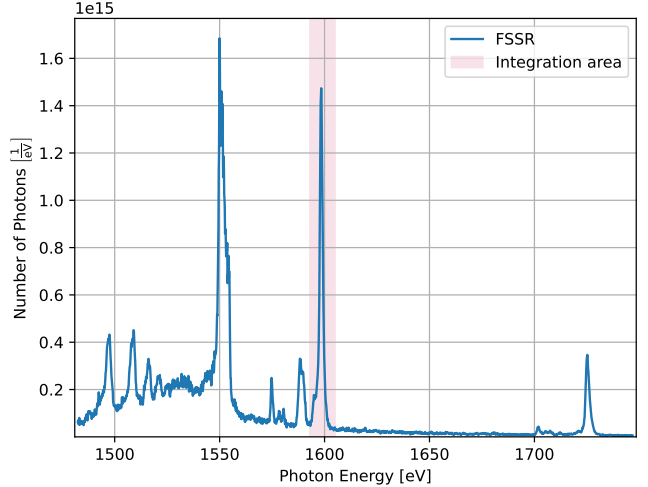
(a) DUCC source channel: Spectrum from a 27 J shot on aluminum (event 19).



(b) SUCC: Spectrum from a 24 J shot on aluminum (event 16).



(c) SUCC: Spectrum from a 27 J shot on aluminum (event 19).



(d) FSSR: Spectrum from a 24 J shot on aluminum (event 16).

Figure IV.4.: Spectra from various spectrometers utilized to determine the conversion efficiency. The area over which the signals belonging to the Al He- α line are summed is depicted in pink.

V. Uncertainty Analysis

In this chapter, the error calculations for the quantitative results presented in chapter 7 are elaborated on. As section 7.1 contains solely qualitative results, only the results of the remaining sections, namely 7.2 and 7.3, will be addressed.

Every error calculation begins with the statistical error, which consists of camera background noise and Poisson noise. I compute the background noise by first getting the standard deviation of the signals of every pixel in the area of the TIFF image from which the background is extracted, e.g. the middle region in fig. 6.1. In the case of the SUCC and DUCC, this standard deviation is then divided by the number of pixel rows N_{rows} that is used for the horizontal lineout of the source spectrum to account for the averaging. For the FSSR, the final background noise corresponds to standard deviation times $\sqrt{N_{rows}}$, since the lineout is formed with summing.

The Poisson noise calculation begins with the raw spectrum extracted by the first part of AXAWOTLS, i.e. the counts for each photon energy. As the Poisson noise accounts for the full counts on the ccd chip, for the DUCC and SUCC I multiply N_{rows} onto the raw spectrum counts to approximately undo the averaging of the lineout. The FSSR spectrum is left the same. I then apply equation 6.1 to get the number of photons incident on the ccd chip. The square root of this number yields the Poisson noise in photons. Inserting this result in the inverse of equation 6.1 gives the counts noise, which for the DUCC and SUCC is divided by N_{rows} to reinstate the lineout averaging. The sum of the Poisson noise and camera background noise gives the statistical error in counts. As the rest of the spectrum processing steps consist of linear calculations, the statistical error can be propagated just like a standard spectrum, effectively converting it to number of photons per steradian per eV.

For every result, a flat error of 20% of the mean signal of the peak is imposed on the FSSR, which is added onto the statistical error to account for the poor crystal quality.

i. Spectral Resolution

The uncertainty of the FWHM of the fits takes the error of the data points into consideration by nature of the algorithm outlined in section 7.2.1. In this case the only error present on the data is the statistical error. For the cases using the transmission data, the error of both source and transmitted spectra are extended using Gaussian error propagation. The remaining uncertainties of the resolution contributions are determined as follows:

- Source broadening: The error of the source size found from the fitting of the knife edge image is carried over to the source broadening through the same path at the source size, since the relations are linear.

- Doppler broadening: FLYCHK simulations of Al plasma with an electron temperature of $T_e = 1000$ eV deliver the base broadening of 0.474 eV. The difference of this value and the Doppler broadening of the He- α line for $T_e = 500$ eV corresponds to the error.
- Crystal broadening: Gaussian error propagation is applied to equation 7.7, giving

$$s_{crystal} = \frac{1}{\sigma_{crystal}} \sqrt{FWHM^2 \cdot s_{FWHM}^2 + \sum_i \sigma_i^2 \cdot s_i^2}, \quad (V.1)$$

where s represents the uncertainty of each resolution contribution.

ii. Ratio of Integrated Reflectivities

The error on the data points is a combination of the statistical error and a systematic error in the form of a filter transmission error. The latter is based off a 5% uncertainty placed on the filter thickness. This relative error is propagated to the filter transmission, which is converted into an absolute error on the counts. The sum of this error and the statistical error builds the uncertainty on the signal. In addition, a systematic error of 5 mm is imposed on the diverging distance and added onto the cumulative error. Through Gaussian error propagation, the error is passed onto the final R_{int} ratio. The same method is applied for the R_{int} of the FSSR computed using the simulated efficiency.

iii. Conversion Efficiency into He- α Line of Aluminum

The uncertainty of CE is determined analogously to that of the R_{int} ratio, except that an additional 50% relative error is assumed for the literature R_{int} values, as estimated from the comparison of the experimental R_{int} ratios with the literature. This uncertainty is incorporated in the same way as with that of the diverging distance D . As such, the error of the CE from the simulated efficiency of the FSSR exhibits a smaller relative error than with the original method, since the uncertainties of D and R_{int} do not play a role.